Charles University in Prague, Faculty of Science

Department of Physiology

Institute of Molecular Genetics, Czech Academy of Sciences

Department of Integrative Biology

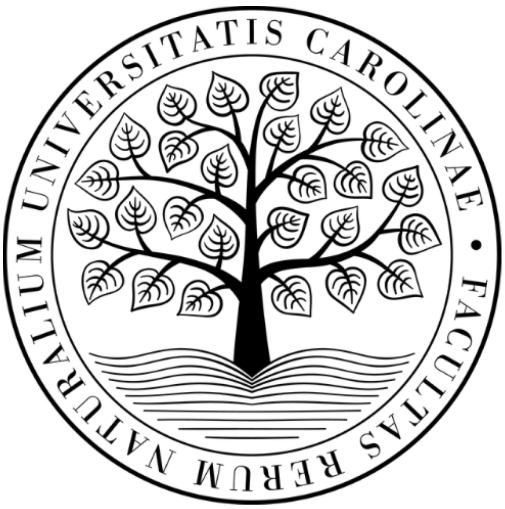

Mgr. Kateřina Korelová

PhD Thesis

The Impact of Plectin Deficiency on Pathogenesis of Liver Diseases

Supervisor:

RNDr. Martin Gregor, PhD.

Table of content

Declaration

I, Katerina Korelová, hereby declare that this PhD thesis is my original work and that it has not been previously submitted (or any of its part) for any academic degree earlier or at another institution. All sources of information used in this thesis have been acknowledged appropriately through citations and references.

Prague, 13.11.2024

Mgr. Kateřina Korelová

Poděkování

Na tomto místě bych chtěla poděkovat RNDr. Martinu Gregorovi, PhD. za vedení práce a možnost pracovat na své doktorské práci v Laboratoři integrativní biologie na Ústavu molekulární genetiky a učit se tak pronikat do tajů vědecké práce. Dále tímto děkuji celému týmu této laboratoře za podporu, jmenovitě Mgr. Markétě Jirouškové, PhD. za mentoring po celou dobu mého studia. Práce byla taktéž podpořena projektem Národního ústavu pro výzkum rakoviny (Program EXCELES, ID: LX22NPO5102 – Financováno Evropskou unií – Next Generation EU).

Chtěla bych poděkovat i svým přátelům, kteří mě vždy podporovali. S nimi je život prostě veselejší.

Velké, děkuji, patří mému manželovi za jeho lásku a kuráž, s jakou jsme přivedli na tento svět naše dvě děti, Zůzu a Máťu, i tuto práci. Dále bych chtěla poděkovat mé sestře Zůze, bez které by toto vše snad ani nebylo možné. V neposlední řadě děkuji rodičům i prarodičům, kteří ve mne vždy věřili a dělali ze mne lepšího člověka, ikdyž se vetšina z nich odevzdání této práce nedočkala, věřím, že by na mne byli hrdí.

List of publications related to the thesis:

Plectin controls biliary tree architecture and stability in cholestasis

Marketa Jirouskova[*], **Katerina Nepomucka (Korelova)**[*], Gizem Oyman-Eyrilmez, Alzbeta Kalendova, Helena Havelkova, Lenka Sarnova, Karel Chalupsky, Bjoern Schuster, Oldrich Benada, Petra Miksatkova, Martin Kuchar, Ondrej Fabian, Radislav Sedlacek, Gerhard Wiche, Martin Gregor

*These authors contributed equally: Marketa Jirouskova, Katerina Nepomucka (Korelova)

J Hepatol. 2018 May;68(5):1006-1017. doi: 10.1016/j.jhep.2017.12.011

My contribution to this study was:

- Acquisition of data:
    - Processing of all mice liver samples for immunofluorescence and histology (H&E, SR, Masson's trichrome, PAS staining) and image acquisition. Primary hepatocytes isolation and treatment with OA, immunofluorescence, protein extraction, and immunoblotting of these samples. Preparation of samples of mice livers for electron microscopy.
- Analysis and interpretation of data:
    - Evaluation of biliary tree morphology and ductular reaction (K19, A6, and Ki67). Analysis of electronmicrographs (TEM and SEM).
- Manuscript preparation:
    - Graphical design of figures, figures.

Isolation and 3D collagen sandwich culture of primary mouse hepatocytes to study the role of cytoskeleton in bile canalicular formation in vitro

Katerina Korelova, Marketa Jirouskova, Lenka Sarnova, Martin Gregor

J Vis Exp. 2019 Dec 20:(154). doi: 10.3791/60507.

My contribution to this study was:

- Acquisition of data.
- Manuscript preparation.

Plectin

Magdalena Prechova, **Katerina Korelova**, and Martin Gregor

Curr Biol. 2023 Feb 27;33(4):R128-R130. doi: 10.1016/j.cub.2022.12.061.

My contribution to this study was:

- Manuscript preparation:
    - Graphical design of figures, figures.

In control of epithelial mechanics: Plectin as an integrator of epithelial cytoskeletal networks

Outla Z*, Prechova M*, **Korelova K**, Gemperle J, Gregor M.

*These authors contributed equally: Outla Z, Prechova M

Submitted to *Open Biology*, currently under revision.

My contribution to this study was:

- Manustricript preparation:
    - Graphical design of figures, figures.

List of publications not related to the thesis:

Dynamics of compartment-specific proteomic landscapes of hepatotoxic and cholestatic models of liver fibrosis

Marketa Jirouskova, Karel Harant, Pavel Cejnar, Srikant Ojha, **Katerina Korelova**, Lenka Sarnova, Eva Sticova, Christoph Mayr, Herbert Schiller, Martin Gregor

Submitted to *eLife*, currently under revision.

My contribution to this study was:

- Acquisition of data:
    - Processing of human liver sections for immunofluorescence and sample acquisition.
- Manuscript preparation:
    - Graphical design of figures, figures.

Plectin-mediated cytoskeletal crosstalk as a target for inhibition of hepatocellular carcinoma growth and metastasis

Zuzana Outla, Gizem Oyman-Eyrilmez, **Katerina Korelova**, Magdalena Prechova, Lukas Frick, Lenka Sarnova, Piyush Bisht, Petra Novotna, Jan Kosla, Patricia Bortel, Yasmin Borutzki, Andrea Bileck, Christopher Gerner, Mohammad Rahbari, Nuh Rahbari, Emrullah Birgin, Bibiana Kvasnicova, Martin Vit, Natalia Ziolkowska, Katerina Sulkova, Andreas Bauer, Eva Sticova, Marketa Jirouskova, Ben Fabry, Martin Otahal, Daniel Jirak, Mathias Heikenwälder, Gerhard Wiche, Samuel M Meier-Menches, Martin Gregor

eLife 2024 https://doi.org/10.7554/eLife.102205.1

My contribution to this study was:

- Acquisition of data:
    - Preparation and processing of HCC mouse models, including the DEN model, HDTVi, and lung colonization assay.
- Analysis and interpretation of data:
    - Analysis of Ki67 and cleaved-Caspase3 staining in xenografts, analysis of lung colonization assay, and participation on quantification of focal adhesions in HCC cell lines.

Abstract (in English)

This thesis investigates the crucial role of plectin, a versatile cytolinker protein, in maintaining the structural integrity and function of liver epithelial cells, specifically hepatocytes and bile duct cells (BEC). Plectin's interactions with keratin filaments and cell adhesion structures such as desmosomes are essential for the stability and resilience of the liver under both physiological and pathological conditions. In our study, we used a liver-specific plectin knockout mouse model ($Ple^{\Delta alb}$) to explore the effects of plectin deficiency on liver cytoarchitecture and the liver's response to cholestatic injury. Immunofluorescence and electron microscopy revealed that plectin-deficient hepatocytes exhibited disrupted keratin networks, with a loss of the typical peri-membranous distribution and increased bundling of keratin filaments within the cytoplasm. This altered cytoarchitecture was associated with significant bile canaliculi dysmorphology, including wider, more meandering bile canaliculi with frequent blind end loops, which are indicative of impaired bile flow and increased biliary pressure. Similarly, BECs in $Ple^{\Delta alb}$ mice showed apicobasal redistribution of keratin filaments and dysregulated cell-cell adhesions, including shorter tight junctions and elevated expression of E-Cadherin. Despite these cytoarchitectural changes, untreated $Ple^{\Delta alb}$ mice did not display significant liver pathology or defects in bile secretion under basal conditions. However, under cholestatic stress induced by bile duct ligation (BDL), 3,5-diethoxycarbonyl-1,4-dihydrocollidine (DDC) feeding, and cholic acid (CA) feeding, $Ple^{\Delta alb}$ mice exhibited significantly aggravated liver injury compared to control mice. This was characterized by more severe biliary epithelial damage, increased fibrosis, and an exacerbated ductular reaction, particularly in the BDL and CA models. Interestingly, the study also demonstrated that the cholestatic stress response in $Ple^{\Delta alb}$ mice involved an adaptive remodeling of the biliary tree, with increased intraluminal surface area through corrugation, potentially as a compensatory mechanism to alleviate cholestatic injury. However, the inability of plectin-deficient cells to efficiently upregulate bile acid transporters and maintain cytoskeletal integrity under stress highlighted the critical role of plectin in preserving liver function. Overall, the findings of this thesis underscore the importance of plectin in maintaining liver epithelial cell integrity, particularly in the face of cholestatic challenges.

Abstrakt (v češtině)

Tato práce se zabývá klíčovou úlohou plektinu, univerzálního cytolinkerového proteinu, při udržování strukturní integrity a funkce jaterních epiteliálních buněk (hepatocytů a cholangiocytů). Interakce plektinu s keratinovými vlákny a buněčnými adhezemi, jako jsou desmosomy, jsou nezbytné pro stabilitu a odolnost jater za fyziologických i patologických podmínek. V naší studii jsme použili myší model, se specifickou delecí plektinu v játrech (*Ple*$^{\Delta alb}$), abychom prozkoumali účinky plektinu na cytoarchitekturu jater a jejich odpověď na cholestatickou zátěž. Světelná a elektronová mikroskopie odhalila, že hepatocyty s deficitem plektinu vykazují narušené sítě keratinových vláken se ztrátou typického peri-membránového rozložení a zvýšeným shlukováním keratinových filament v cytoplazmě. Tato změněná cytoarchitektura byla spojena s výraznou dysmorfologií žlučových kanalikulů, jenž byli širší, více klikatější, s častými slepými koncovými kličkami, které svědčí o zhoršeném průtoku žluči a zvýšeném tlaku ve žlučovodech. Stejně tak cholangiocyty u *Ple*$^{\Delta alb}$ myší vykazovali apikobazální redistribuci keratinových vláken a dysregulované buněčné adheze, včetně kratších těsných spojů a zvýšené exprese E-Cadherinu. Navzdory těmto cytoarchitektonickým změnám nevykazovaly *Ple*$^{\Delta alb}$ myši významnou jaterní patologii bez zátěže. Při cholestatické zátěži, vyvolané podvázáním žlučových cest (BDL), podáváním 3,5-diethoxykarbonyl-1,4-dihydrokollidinu (DDC) a kyseliny cholové (CA), však *Ple*$^{\Delta alb}$ myši vykazovaly, ve srovnání s kontrolními myšmi, výrazně zhoršené poškození jater. To bylo charakterizováno závažnějším poškozením žlučového epitelu, zvýšenou fibrózou a zhoršenou duktulární reakcí, zejména u BDL a CA modelů. Tato studie také prokázala, že reakce na cholestatický stres u *Ple*$^{\Delta alb}$ myší zahrnovala adaptivní remodelaci žlučového systému se zvětšením intraluminálního povrchu prostřednictvím zvlnění, což může být kompenzační mechanismus ke zmírnění cholestatického poškození. Neschopnost buněk s nedostatkem plektinu účinně regulovat transportéry žlučových kyselin a udržovat integritu cytoskeletu při zátěži, však zdůraznila kritickou roli plektinu při zachování funkce jater. Celkově výsledky této práce zdůrazňují význam plektinu pro zachování integrity jaterních epiteliálních buněk, zejména tváří v tvář cholestatickým výzvám.

List of abbreviations

AB, apical bulkheads

ABC transporters, ATP-binding cassette transporters

ABCB4 / MDR3, ATP Binding Cassette Subfamily B Member 4

ABCC2, ATP-binding cassette sub-family C member 2

AJ, adherens junctions

ALP, alkalinephosphatase

ALT, alaninetransaminase

AMAs, antimitochondrial antibodies

AMPK, AMP-activated protein kinase

ANIT, α-naphthylisothiocyanate

APC, adenomatous polyposis coli protein

aPKC, atypical protein kinase C

AQP1, aquaporin 1

AQP4, aquaporin 4

AST, aspartatetransaminase

ATP, adenosine triphosphate

ATP8B1, ATPase Phospholipid Transporting 8B1

BC, bile canaliculus

BD, bile duct

BDL, bile duct ligation

BECS, biliary epithelial cells or cholangiocytes

BSEP/ ABCB11, bile salt export pump / ATP Binding Cassette Subfamily B Member 11

BW, body weight

CA, cholic acid

CBD, common bile duct

Cdc42, cell division control protein 42

CDE, choline-deficient, ethionine-supplemented

CFTR, cystic fibrosis transmembrane conductance regulator

Coll, collagen

CV, entral vein

DAPI, 4',6-diamidin-2-fenylindol

DCA, deoxychlic acid

DDC, 3,5-diethoxycarbonyl-1,4-dihydrocollidine

DPP4, dipeptidyl peptidase IV

Ds, desmosomes

Dsg, desmoglein

Dsp, desmoplakin

E-Cad, E-Cadherin

ECM, extracellular matrix

EDTA, ethylenediaminetetraacetic acid

ERM family proteins (ezrin, radixin, and moesin)

fch/fch, ferrochelatase gene

GAPDH, glyceraldehyde 3-phosphate dehydrogenase

H&E, hematoxylin and eosin

HA, hepatic artery

Hax1, HCLS1-associated protein X-1

HCC, hepatocellular carcinoma

HSCs, hepatic stellate cells

IBD, inflammatory bowel diseases

IF, intermediate filament

IgA, immune globulin A

K18, keratin 18

K19, keratin 19

K7, keratin 7

K8, keratin 8

KC, Kupffer cells

LKB1, liver kinase B1

LSECs, liver sinusoidal endothelial cells

LW, liver weight

MDCKs, Madin-Darby canine kidney cells

MDR2KO, MDR2-knockout mice

MRP2/MDR2, multidrug resistance protein 2

NAFLD, non-alcoholic fatty liver disease

OA, okadaic acid

pan-K, pan-keratin

Par complex, partitioning defective protein complex

Par3, partitioning defective protein 3

PAS, periodic acid of Shiff

PBC, primary biliary cholangitis

PBS, phosphate buffered saline

PBST, phosphate buffered saline + 0.1% tween

PDH-E2, E2 subunits of 2-oxo-acid dehydrogenase complexes, such as pyruvate dehydrogenase

PFA, paraformaldehyde

PFIC, progressive familial intrahepatic cholestasis-like pattern

Ple$^{fl/fl}$, Plec$^{flox/flox}$

Ple$^{\Delta alb}$, liver-specific plectin knockout

PLEKO plectin-knockout

PSC, primary sclerosing cholangitis

PV, portal vein

Slc10a1, Solute Carrier Family 10 Member 1 (NTPC in humans).

SR, Sirius red

tBA, totale bile acids

TJ, tight junction

TJP2, tight junction protein 2

WIF-B cells, hepatoma-derived hybrid cell line

ZO-1, zonula occludens-1

αSMA, Alpha smooth muscle actin

1. Introduction

Liver diseases represent a major global health concern, contributing significantly to morbidity and mortality worldwide. Conditions such as hepatitis, non-alcoholic fatty liver disease, alcoholic liver disease, cholestasis, cirrhosis, and hepatocellular carcinoma affect millions of individuals, often leading to life-threatening complications (Bataller and Brenner 2005). These diseases arise from a wide range of causes, including viral infections, excessive alcohol consumption, metabolic disorders, and exposure to toxins or certain medications. The burden of liver diseases continues to rise, especially with the increasing prevalence of obesity and metabolic syndrome. Despite advances in medical research, effective treatments for advanced stages of liver diseases, particularly cirrhosis and hepatocellular carcinoma, remain limited, and liver transplantation is often the only viable solution, underscoring the urgent need for a deeper understanding of the underlying mechanisms.

The progression of liver diseases involves complex interactions between hepatocytes, bile duct cells, and the surrounding extracellular matrix, leading to liver dysfunction and tissue remodeling (Bataller and Brenner 2005). A one of the hallmark of liver disease progression is cholestasis, the impairment of bile flow, which can result from bile duct obstruction, hepatocellular dysfunction, or damage to the bile canaliculi. Cholestasis triggers a cascade of pathological responses, including inflammation, oxidative stress, and fibrosis, which exacerbate liver injury and promote disease progression toward cirrhosis and liver failure (Yokoda and Rodriguez 2020). Understanding the cellular and molecular mechanisms that drive cholestatic liver disease is crucial for identifying novel therapeutic targets and developing effective interventions to halt or reverse the progression of liver damage. A deep understanding of how the liver preserves its structure and function under normal conditions is crucial for uncovering the mechanisms that become disrupted in liver diseases.

1.1 Liver

The liver is the second largest organ (after skin) in the human body. The liver is located in the right upper quadrant of the abdominal cavity, strategically positioned to receive portal blood from the stomach, intestines, pancreas, and spleen, enabling it to efficiently process and filter blood while maintaining the blood-bile barrier (Boron, Medical Physiology, 2012).

The liver is a complex organ that plays a pivotal role in performing diverse functions that are critical for maintaining physiological homeostasis. It stores nutrients absorbed after a meal

and releases them in a regulated manner, dynamically controlling the metabolite content in circulation (Michalopoulos and DeFrances 1997). Moreover, the liver performs detoxification processes, defending the organism against pathogens and xenobiotics. It also has exocrine functions in bile acid production and endocrine functions in hormone release. Additionally, it is a major site for protein synthesis in the body, producing a significant proportion of circulating blood proteins such as albumin, complement system proteins, and blood clotting factors (Boron, Medical Physiology, 2012). These different functions and liver micro-organisation are highly linked and tightly regulated (Gebhardt 1992; Jungermann 1986).

1.2 **Liver structure and organization**

The human liver consists of two main lobes (Figure 1A), in contrast, the mouse liver contains seven lobes (Martins 2008). The individual lobe is made up of eight segments that are formed by thousand repeating basic anatomical units described as lobules (Figure 1B). The classic lobule unit is a hexagonal structure in cross-section that resembles polygonal shaped column. The column measures approximately 1 mm in diameter in human (Figure 1C) and 0.5 mm in mice (Teutsch 2005).

At the center of each liver lobule residues a branch of the central hepatic vein, while at each of the six corners are portal triads composed of the hepatic artery, portal vein, and bile duct, where blood enters the liver lobule. Blood flows radially inwards toward the central vein through sinusoidal blood vessels. Hepatocytes are arranged in plates, consisting of 15 - 25 hepatocytes in humans and 12 - 15 hepatocytes in mice, which extend along the radial axis of the lobule (Figure 1D). Between two adjacent hepatocytes, their apical domains form an intercellular space known as the bile canaliculus. The bile canaliculi (Figure 1E) facilitate the outward transport of bile secreted by hepatocytes, moving in the opposite direction to blood flow. Bile is then conveyed into bile ductules located at the portal triads, from where it is transported to the intestines.

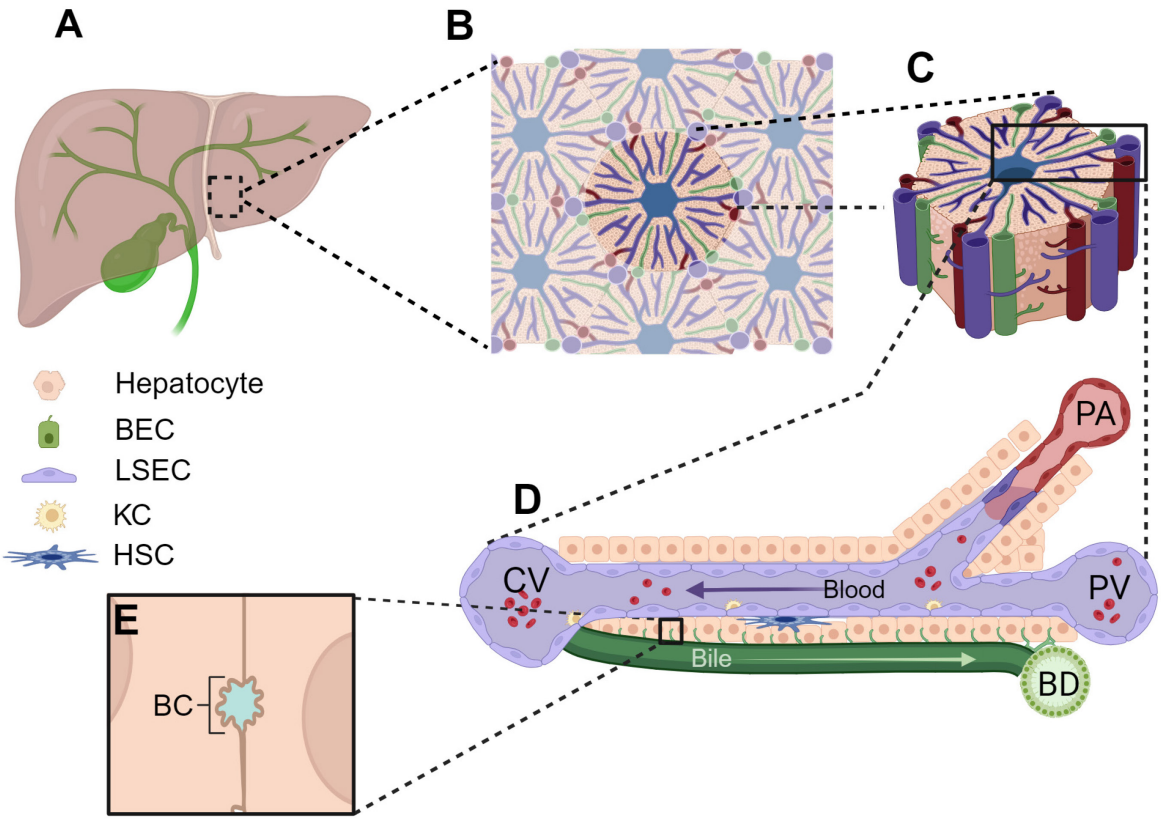

Figure 1. *Liver structure at different scales.* The human liver consists of two main lobes **(A)**. Both are made up of eight segments **(B)** that consists of thousands lobules **(C)**. Hexagonal unit with a branch of the hepatic vein (central vein, CV) at its center and, at each of the six corners, portal triads that contains the hepatic artery (HA), portal vein (PV), and bile duct (BD) and where blood enters the liver lobule **(D)**. The blood flows radially inwards towards CV via sinusoidal blood vessels. Hepatocytes are arranged in plates of 15-25 that extend along the radial axis of the lobule. Beside liver parenchymal cells (hepatocytes), the liver consists of liver endothelial cells (LSECs), hepatic stellate cells (HSCs), cholangiocytes (biliary epithelial cells, BECs), and Kupffer cells (KC). Between two adjacent hepatocytes the bile canaliculus (BC) is formend **(E)**. The BC facilitate the outward transport of bile secreted by hepatocytes, moving against the direction of blood flow. The bile is then conveyed into BD located at the portal nodes, from where they are transported to the intestines. Created in BioRender.com

Due to polarized blood flow in the lobule, periportal hepatocytes regulate the microenvironment of downstream pericentral hepatocytes by consuming oxygen and nutriens and secreting hormones, creating concentration gradients along the periportal-pericentral axis (Figure 2) (Cunningham and Porat-Shliom 2021). Approximately 75 % of the blood entering the lobule is venous blood from the intestine, while only 25 % originates from highly oxygenated arterial blood (Torre, Perret, and Colnot 2010). This makes oxygen availability a potential limiting factor for hepatocytes. As blood moves towards the central vein, hepatocytes consume oxygen through respiration, resulting in decreased oxygen concentrations. Oxygen is essential for hepatocytes to produce ATP, which fuels their various energy-demanding functions, including the continuous synthesis of secreted proteins and gluconeogenesis for

glucose secretion during fasting. Interestingly, periportal hepatocytes appear to regulate their respiration to prevent hypoxia in pericentral hepatocytes (Israel and Orrego 1984). The oxygen pressure in sinusoids decreases from 65 mmHg at the portal regions to 30 mmHg in pericentral regions. With an additional decrese of 10 - 20 mmHg from the sinusoids to the hepatocytes, the hepatocytes in pericentral regions approaching but still remain above levels of hypoxia (~2 mmHg) (Kietzmann et al. 2006). During pathologies when increase hepatocyte consumption of oxygen, such as excessive alcohol consumption, can result in pericentral hypoxia. Therefore, hepatocyte consumption of oxygen is likely to minimizing the risk of hypoxia of hepatocytes in pericentral regions (De Groot et al. 1988; Arteel et al. 1996).

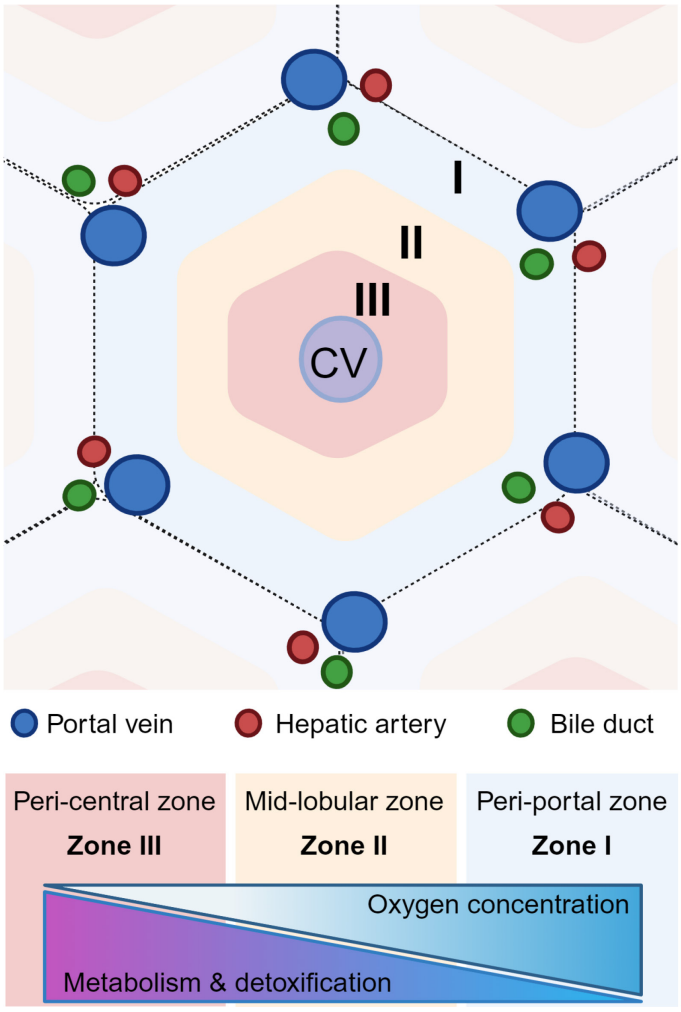

Figure 2. *Liver zonation.* The geometric scheme of a hepatic lobule, hexagonal unit, the vertices represent the portal triad that contains branches of the hepatic artery, portal vein, and bile duct. This organisation results in formation of a number of gradients including oxygen, nutrients, metabolic waste products. This gradient formation and the consequential organization of subsequent metabolic processes have been called liver zonation. Gradients depicted below shows to both oxygen and metabolic pathways (glycolysis, lipogenesis, ketogenesis, TG synthesis) and detoxification along the sinusoid. Created in BioRednder.com.

Hepatocyte respiration represents just one of several liver functions that exhibit non-uniform distribution along the radial axis of the lobule, a phenomenon referred to as liver zonation (Jungermann and Kietzmann 1996; Gebhardt and Matz-Soja 2014; Schliess et al. 2014). Each hepatic acinus can be subdivided into three sub-zones of hepatocytes (Figure 2), each with distinct levels of oxygen supply and metabolic function. Zone I, also known as the periportal zone, receives blood rich in oxygen, hormones, and nutrients.

Zones II and III, identified as the mid and pericentral zone, and are supplied with blood poor in oxygen but rich in CO_2 and metabolic waste products.

Beside liver parenchymal cells (hepatocytes), the liver consists of liver endothelial cells (LSECs), hepatic stellate cells (HSCs), cholangiocytes (biliary epithelial cells, BECs), and Kupffer cells (Figure 1D). The walls of liver sinusoids are lined by LSECs that create a fenestrated structure with their bodies and cytoplasmic extensions. Plasma solutes, excluding blood cells, thus can freely enter the space of Disse (Figure 3) through these fenestrae. Some evidence suggests that fenestrae may regulate access to the perisinusoidal space of Disse by contracting Kupffer cells, a population of resident macrophages, residing within the sinusoidal vascular space. HSCs are located in the space of Disse and are morphologically characterized by the presence of large fat droplets in their cytoplasm. These cells play a pivotal role in vitamin A storage, and can be activated and transform into proliferative, fibrogenic, and contractile activated HSCs. The amount of stored vitamin A decreases progressively during liver injury. Upon chronic liver injury, activated HSCs transform into myofibroblasts to contribute to fibrogenesis by remodeling the extracellular matrix (ECM) and depositing fibrous ECM rich in type I collagen, potentially leading to cirrhosis (Bataller and Brenner 2005; Krizhanovsky et al. 2008).

1.2.1 Hepatocyte structure

Hepatocytes are the primary epithelial cells in the liver, comprising approximately 80% of its volume and 60% of its cellular composition. Structurally, hepatocytes are polygonal in shape, with a centrally located nucleus and a cytoplasm that houses a variety of organelles. These cells are densely packed with mitochondria, reflecting their high energy demand. The Golgi apparatus is typically located near the nucleus and bile canaliculi, playing a role in the processing and transport of proteins. Hepatocytes also feature both rough and smooth endoplasmic reticulum, which are distributed throughout the cytoplasm. The rough endoplasmic reticulum is involved in protein synthesis, while the smooth endoplasmic reticulum is associated with lipid metabolism. Additionally, hepatocytes contain a large number of endosomes, lysosomes, and peroxisomes, which are important for intracellular transport and recycling. The overall arrangement of these organelles supports the highly organized and compartmentalized structure of hepatocytes, ensuring efficient metabolic processes (Blouin, Bolender, and Weibel 1977).

Structurally, hepatocytes are polyhedral cell measuring approximately 20 - 30 µm in size, with a volume of around 5000 µm^3 (Boyer et al. 2012). Unlike the majority of epithelial cells, which are polarized within the plane of the tissue, the hepatocytes display a distinctive polarity (Bryant and Mostov 2008; Musch 2014; Slim et al. 2014; Treyer and Musch 2013). Hepatocytes are characterized by distinct apical, lateral, and basal domains (Figure 3). The basal domain of hepatocytes faces the sinusoidal endothelium, forming the sinusoidal domain. The apical domain faces adjacent hepatocytes and encloses the bile canaliculi, forming the canalicular domain (Figure 3A and 3B). Lateral membranes of hepatocytes extend from the bile canaliculi to the space of Disse and establish cell-cell adhesions (tight junctions, adherent junctions, desmosomes, and gap junctions). The tight junctions are sealing the bile canalicular lumen from the interstitial space, preventing bile leakage into plasma, and blocking bile backflow from the interstitial space into the blood (Boyer 1983). Moreover, the bile canalicular

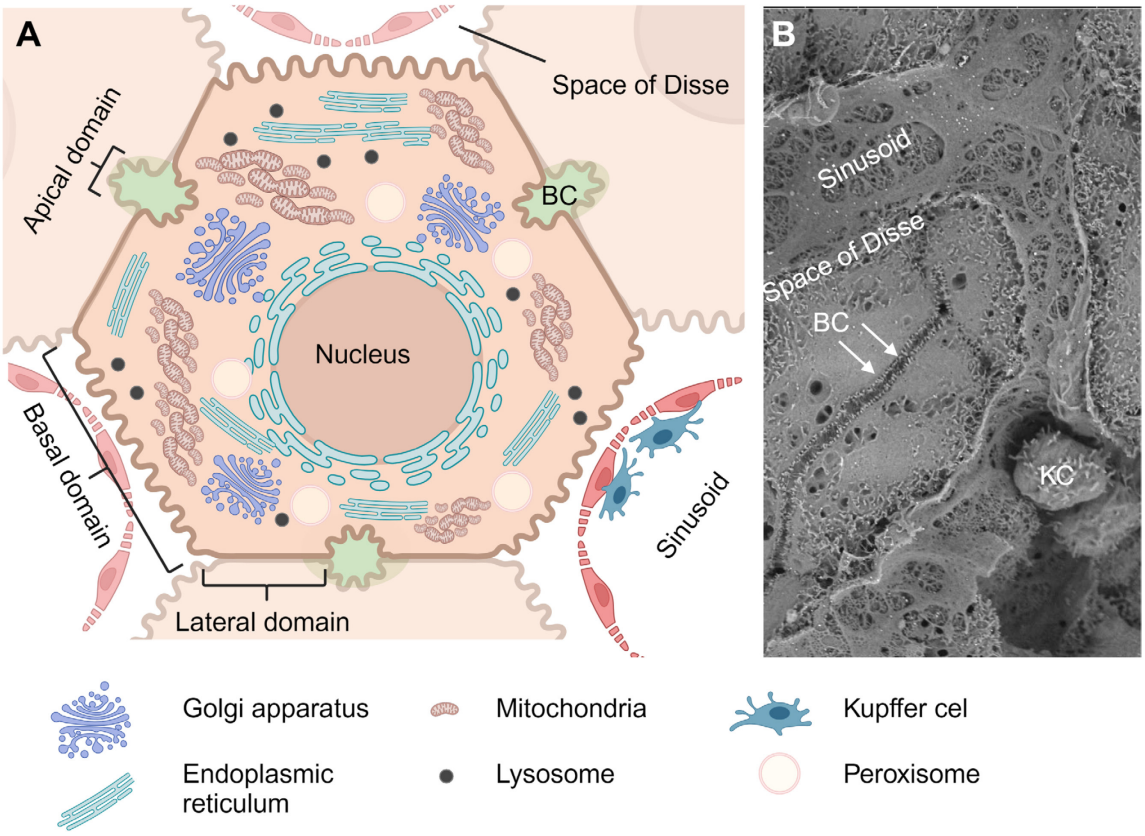

Figure 3. *Hepatocyte structure.* **(A)** Scheme of hepatocyte. Within the cytoplasm of hepatocytes, there are numerous mitochondria, prominent Golgi apparatus situated between the nucleus and bile canaliculi, as well as both rough and smooth endoplasmic reticulum. Additionally, liver cells contain numerous endosomes, lysosomes, and peroxisomes. Hepatic plasma membrane is separated into sinusoidal (basal), canalicular (apical), and lateral domains. **(B)** Scanning electron micrograph (SEM) of hepatocytes and fenestrated sinusoids in a section of acquired mouse liver. Space of Disse; sinusoid, BC (arrows) and Kupffer cells (KC) are indicated. SEM micrographs acquired in collaboration with Dr. Benada, Institute of Microbiology of the CAS. Created in BioRender.com.

network forms an intricate and highly organized three-dimensional (3D) structure within the liver parenchyma, connecting individual hepatocytes and allowing efficient bile transport across the lobules (Figure 3B). This complex network ensures that bile, secreted by hepatocytes, is efficiently conveyed toward the bile ducts while maintaining separation from the surrounding blood circulation. To uphold the unique distribution of transporters, channels, and receptors in these domains, hepatocytes have evolved intricate polarized trafficking mechanisms depended on cytoskeleton networks and cell-cell junctions (Boyer 2013; Wang and Boyer 2004).

1.2.2 Hepatocytes polarity and integrity

Hepatocyte polarity is a fundamental aspect of liver architecture and function, crucial for bile production, secretion, and overall liver homeostasis. The mechanisms that sustain hepatocyte polarity and integrity can be divided into structural and functional components. Structurally, this involves preserving the stability of the cytoskeleton, maintaining cell-cell junctions, and ensuring the integrity of apical domains, including their microvilli, while supporting the development and maintenance of the intricate bile canalicular network (Musch 2014).

Functionally, hepatic polarity is primarily driven by the activity of canalicular ATP-binding cassette (ABC) transporters, which are essential for bile secretion. These processes are energy-dependent and are regulated by AMP-activated protein kinase (AMPK), which plays a critical role in maintaining the energy balance required for proper transporter function and overall hepatocyte polarity (Fu et al. 2010). AMPK senses cellular energy levels and activates pathways to maintain energy balance. Activation of AMPK by phosphorylation triggers responses to cellular stress, promoting glucose, lipid, and protein homeostasis, as well as mitochondrial biogenesis. In hepatocytes, AMPK activation promotes bile canaliculi network formation, crucial for liver function. Phosphorylation of AMPK is mediated by liver kinase B1 (LKB1) (Hawley et al. 1996). Recent studies also indicate that LKB1-mediated AMPK activation plays a role in enhancing bile canaliculi network formation by promoting cytoskeletal rearrangements, which are essential for the structural integrity of bile canalicular network (Fu et al. 2010). Under conditions of ATP depletion, as seen in liver injury, the activation of LKB1 and AMPK together helps hepatocytes maintain or restore polarity, ensuring the function of the bile canalicular system despite stress (Woods et al. 2011). Studies on LKB1-knockout mice demonstrate polarity defects, cholestasis, and liver injury, implicating

LKB1 and AMPK in hepatocyte polarization (Just et al. 2015). However, the precise mechanisms by which AMPK and LKB1 regulate polarity remain to be fully elucidated.

The polarization of hepatocytes and bile canalicular network formation depend on the coordinated expression of conserved components, including the junctional complexes and polarized protein trafficking machinery, all supported by the cytoskeleton. (Gissen and Arias 2015; Cozmescu and Gissen 2021).

1.2.2.1 Cell junctions

The blood-bile barrier, formed by the cell-cell junctions that connect hepatocytes (Figure 4), is essential for maintaining the separation of bile and blood, ensuring the proper function of the liver (Theard et al. 2007). The tight junction complex comprises claudins, occludins, and zonulla occludens proteins, preventing the leakage of molecules between cells. Disruption of tight junctions in transgenic mice (Kojima et al. 1999), in primary hepatocytes *in vitro*, and tissue sections from hepatobiliary diseases leads to depolarization of hepatocytes and results into hepatocellular injury (Kojima et al. 2007). In non-polarized hepatocytes and epithelial cells, tight junction proteins and apical hepatic transporters (such as bile salt export pump (BSEP) relocate to intracellular sites (Torok et al. 2020), including the microtubular organizing center, where they colocalize with Rab11a and myosin Vb (Wakabayashi et al. 2005). Identification of pathologic mutations affecting tight junction protein 2 (TJP2) and claudin1 in patients with severe liver disease underscores the critical role of tight junctions in maintaining hepatocyte structure and function (Baum and Georgiou 2011; Kojima et al. 1999; Hadj-Rabia et al. 2004; Sambrotta et al. 2014; Wakabayashi et al. 2005). Moreover, Tocan et al. (Tocan et al. 2021) showed that the tight junction protein Par3, in cooperation with cell division control protein 42 (Cdc42), orchestrates hepatocyte polarization by targeting atypical protein kinase C (aPKC). Using 3D culture models, depletion of Par3, Cdc42, or aPKC impaired apicobasolateral polarity and apical lumen formation and bile canaliculi elongation (Wang et al. 2014). While lateral membrane-associated proteins such as, lethal giant larvae 1 (Lgl1) and Lgl2 were shown to be dispensable for polarity establishment, they maintain lateral integrity. Together, Par3, Cdc42, and aPKC coordinate hepatocyte polarity and apical lumen formation (Tocan et al. 2021). β-catenin, as a key component of adherens junctions, links cadherins to the actin cytoskeleton, playing a crucial role in maintaining cell-cell adhesion and the structural integrity of bile canaliculi. Yeh et al. (2010) showed, that liver-specific β-catenin

deletion, results in bile canalicular abnormalities such as dilatation and tortuosity, leading to impaired bile secretion and cholestasis *in vivo* (Yeh et al. 2010).

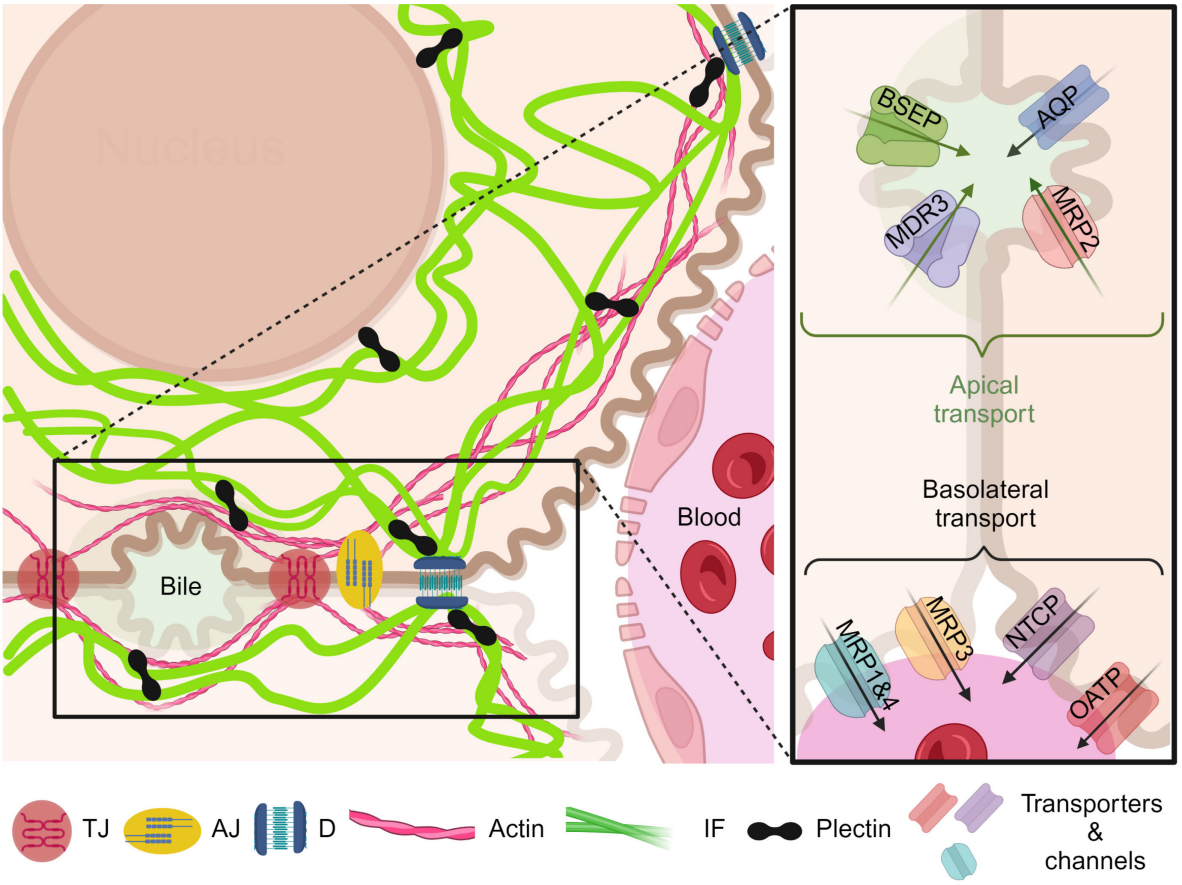

Figure 4. *Organization of hepatocytes.* Scheme of the hepatocellular cytoskeleton, cell junctions, and bile transport pathways. In the hepatocyte, the cytoskeleton is composed of microfilamntes, intermediate filaments, and microtubules. Here depicted actin filaments (pink), intermediate filaments (green) which are interconneted via plectin (black) to maintain cellular integrity. Tight junctions (TJs, red), adherens junctions (AJs, yellow), and desmosomes (Ds, blue) form essential cell-cell adhesion. The inset on the right illustrates the transporters involved in bile acid transport. Apical transporters, including bile salt export pump (BSEP), multidrug resistance protein 3 (MDR3), aquaporin (AQP), and multidrug resistance protein 2 (MRP2), direct bile acids into the bile canaliculi. Basolateral transporters, such as MRP3, MRP1&4, sodium/taurocholate cotransporting polypeptide (NTCP), and organic anion transporting polypeptide (OATP), regulate the flow of substances between the blood and hepatocytes. This diagram highlights the polarity of hepatocytes, with coordinated apical and basolateral transport critical for bile production and liver function. Created in BioRender.com.

1.2.2.2 Cytoskeleton

The cytoskeleton plays a pivotal role in maintaining hepatocyte polarity by providing structural support and facilitating the transport of cellular components. Actin filaments are particularly important for the formation and maintenance of bile canaliculi, supporting structures like microvilli that enhance bile secretion. Additionally, microtubules and intermediate filaments contribute to the stability and organization of the basolateral domain, ensuring proper cell-cell adhesion (Omary, Ku, and Toivola 2002; Ku et al. 2016).

The actin cytoskeleton forms a dense network beneath the apical membrane of hepatocytes, providing the necessary support for bile canaliculus formation and contraction (Tsukada, Ackerley, and Phillips 1995). This actomyosin network enables the dynamic regulation of bile canalicular shape, aiding in the rhythmic contractions that drive bile flow (Gupta et al. 2017). Additionally, actin filaments facilitate the trafficking of membrane proteins crucial for bile secretion (e.g. BSEP) (Roma, Crocenzi, and Mottino 2008). Perturbations in actin organization, such as those caused by chemical toxins (phalloidin) (Watanabe et al. 1983) or cholestatic conditions, can lead to the dysfunction and dilation of bile canaliculi, compromising bile flow (Gupta 2023). The remodeling of bile canaliculi, triggered by mechanical or chemical stress, further highlights the adaptive nature of the actin cytoskeleton in maintaining bile secretion during injury or regeneration (Meyer et al. 2020).

Dynamic microtubules play a pivotal role in facilitating the trafficking of both secreted and canalicular proteins. For instance, newly synthesized BSEP, the canalicular bile acid transporter, and other canalicular ABC transporters travel from the trans-Golgi network along microtubules (Wakabayashi, Lippincott-Schwartz, and Arias 2004). However, microtubules do not directly attach to the canalicular membrane. Instead, cargo endosomes are transferred to the pericanalicular actomyosin belt. It is known that microtubules become associated with actin through a pericanalicular actin-binding complex comprising proteins, such as cytoplasmic linker protein 170, adenomatous polyposis coli protein, HCLS1-associated protein X-1 and cortactin (Kong et al. 2014). Also syntaxin 3 has been proposed as a potential docking site, facilitating the fusion of protein sorting vesicles with the inner leaflet of the bile canalicular membrane (ter Beest et al. 2005). Radixin, as other expamle of adaptor protein linking actin to the plasma membrane, it has been shown that radixin is also involvedlinking certain cargo molecules like MRP2 to the pericanalicular actin network (Li et al. 2010). Studies involving radixin-knockout (*radixinKO*) mice have demonstrated impaired MRP2 localization to the bile

canaliculus, leading to progressive loss of microvilli and subsequent hepatocyte injury (Kikuchi et al. 2002).

1.2.2.2.1 The intermediate filaments

The intermediate filaments consist of a large family of tissue-specific proteins that include the cytoplasmic keratins as the largest subgroup (encoded by 54 different genes), vimentin, neurofilaments, and lamins, among others (Jacob et al. 2018). The secondary structure of keratins is composed of a central α-helical rod domain, flanked by N-terminal head and C-terminal tail domains, which are themselves arranged in a tripartite configuration. The structure of keratins consists of acidic type I and neural-basic type II keratins that form noncovalent heteropolymeric complexes, which polymerize to form filamentous arrays (10 nm wide). Different combinations of type I and type II keratins are expressed in various epithelial cell types. In hepatocytes, keratin filaments are formed by type I keratin 18 (K18) and type II keratin 8 (K8), which are present in equimolar ratio, whereas BECs express keratin 7/keratin 19 (K7/K19), K8/K18. Additionally, keratin 23 (K23) has been reported in human end-stage liver disease, but its expression is absent in healthy BECs (Gribben et al. 2024). Unlike microfilaments and microtubules, intermediate filaments enable cells and tissues to withstand deformations and mechanical challenges (Jacob et al. 2018). Additionally, keratins play nonmechanical roles such as facilitating protein targeting, modulating protein synthesis, positioning organelles, and guarding against apoptosis and necrosis. This has earned keratins the title "guardians of the liver" by Omary et al. as significant upregulation of keratin mRNA and protein levels has been observed during various stress conditions (Ku et al. 2016; Zatloukal et al. 2004; Omary, Ku, and Toivola 2002; Toivola et al. 2015). More intriguing insights into the role of intermediate filaments in liver disease will be explored in Chapter 1.4.2.

Keratin posttranslational modifications are fundamental to the regulation and function of the hepatocyte cytoskeleton, significantly influencing liver health and resilience. Key post-translational modification includes phosphorylation, glycosylation, ubiquitination, sumoylation, and acetylation. The most comprehensively understood modification of keratin filaments is phosphorylation, which plays a crucial role during cell injury, where increased keratin phosphorylation is often driven by the activation of stress-responsive and other kinases (Omary, Ku, and Toivola 2002; Toivola et al. 2024; Toivola et al. 2010). Glycosylation, although less studied, affects keratin stability and solubility by influencing keratin filament mechanical properties and overall cytoskeletal integrity (Majumdar et al. 2012). Moreover, Ku

et al. (2010) showed that glycosylation of K18 provides a protection in hepatic epithelium from injury induced by streptozotocin by promoting the phosphorylation and activation of pro-survival kinases (Ku et al. 2010). Ubiquitination prevents the accumulation of damaged or misfolded keratin filaments, maintaining cellular homeostasis (Rogel, Jaitovich, and Ridge 2010). The process of sumoylation has been demonstrated to exert a significant influence on the localization, stability and interactions of keratin filaments. Hyper-sumoylation has been observed in various human liver diseases (Li et al. 2024). Notably, common disease-associated variants of keratins (such as K8) have been shown to induce keratin hyper-sumoylation, leading to a significant reduction in keratin solubility (Snider et al. 2011). This altered sumoylation state may disrupt the normal function of keratins, contributing to liver disease pathogenesis (Snider et al. 2011). Acetylation and methylation impacts filament assembly, interactions with other cytoskeletal elements, and transcriptional regulation of keratin genes (Jang et al. 2019).

Building on the role of post-translational modifications in keratin stability, several studies have also linked the formation of keratin aggregates, specifically Mallory-Denk bodies, to dysregulated keratin expression, hyperphosphorylation, and cross-linking (Toivola et al. 2015; Strnad et al. 2012). These distinctive K8/K18 aggregates were first identified by Zatloukal et al. (2007) in liver biopsies from patients with chronic liver disease and were subsequently observed in liver tissues from experimental mouse models of cholestasis (Zatloukal et al. 2007). The formation of Mallory-Denk bodies is contingent upon an altered K8/K18 ratio, where an increased K8-to-K18 ratio predisposes hepatocytes to aggregate formation. Notably, overexpression of K8 or K18 in transgenic mice has been shown to promote the formation of these aggregates, emphasizing the critical role of balanced keratin expression in liver cell integrity and response to injury.

Proper organization of keratin filaments network is maintained by cytoskeletal linker proteins (cytolinkers) of the plakin protein family. It is noteworthy that proteins belonging to the plakin family, such as periplakin and epiplakin, have been identified as being upregulated in experimental cholestatic mouse models (Ito et al. 2013; Quick 2018; Szabo, Wogenstein, and Fuchs 2016; Szabo et al. 2015).

1.2.2.2.2 Plectin

Plectin is a multidomain protein of approximately 4500 amino acids, with a structure that includes an N-terminal actin-binding domain, a plakin domain, a central rod domain, and a C-terminal domain that binds intermediate filaments (Figure 5), previously reviewed in

(Bouameur, Favre, and Borradori 2014; Leung, Green, and Liem 2002; Prechova et al. 2022). This unique structure allows plectin to bridge various cytoskeletal components by linking intermediate filaments, such as keratins and vimentin, to actin filaments and microtubules, thereby enhancing mechanical stability and maintaining structural integrity of cells (Wiche 1998).

One of plectin's defining features is its isoform diversity, generated through the alternative splicing of variable first exons into a common exon 2 (Fuchs et al. 1999). This process produces isoforms with distinct N-terminal head domains, which determine their specific cellular localization and interaction partners (Rezniczek et al. 2003; Kostan et al. 2009; Burgstaller et al. 2010). These isoforms allow plectin to fulfill specialized roles in different cell types and tissues, tailoring its function to the mechanical demands of particular environment.

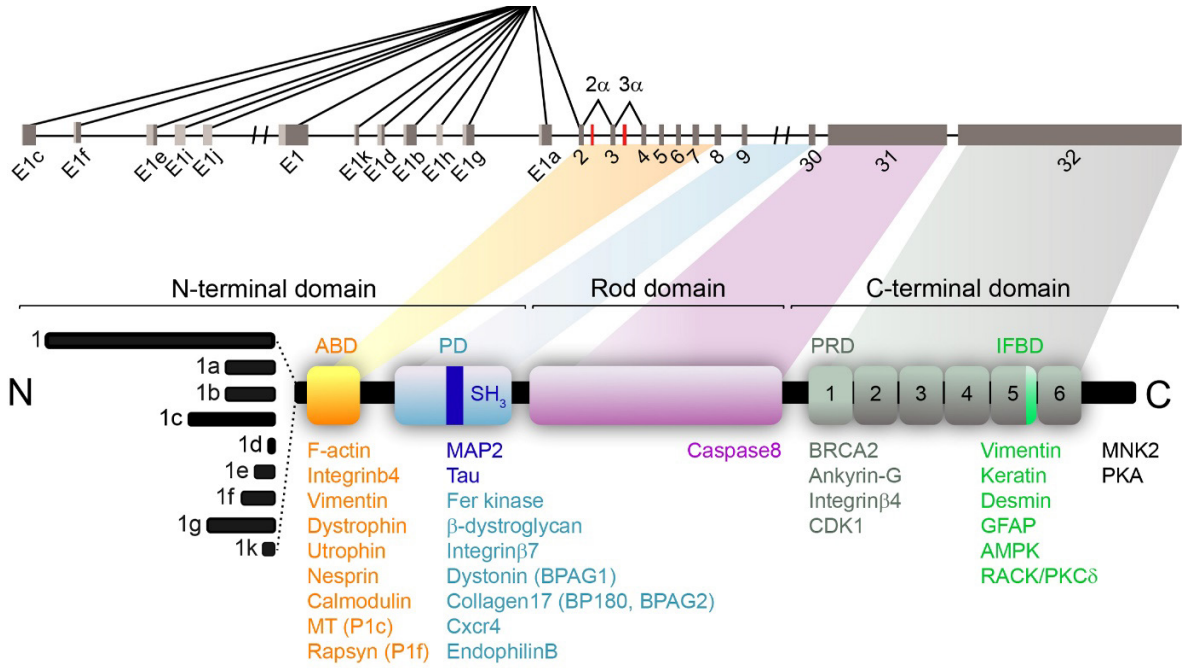

Figure 5. *Plectin structure*. Scheme of plectin gene and protein domains. plectin gene (upper part of the scheme) is encoded by 32 exons, untranslated regions (gray), and two optionally spliced exons: 2a and 3a (red). The plectin molecule has three main structural domains (N-terminal; Rod and C-terminal domain). N-terminal domain contains the actin- binding domain (ABD; yellow) and plakin domain (PD; light blue), which contains non-canonical SH3 domain (dark blue). The C-terminal domain consists of six plectin repeat domains (PRD; gray), with the linker region of the fifth PRD containing an IF-binding domain (IFBD, green). The corresponding interacting partners are indicated below (Prechova et al., review under revision).

For example, plectin isoforms in epithelial cells help anchor intermediate filaments to adhesion complexes, while in muscle cells, specific isoforms link the cytoskeleton to costameres, essential for muscle integrity (Wiche 2021).

Plectin serves as a crucial cross-linker of the cytoskeleton. In epithelial cells, keratin filaments form a submembranous network that provides mechanical resilience and links the cell cortex to the nuclear envelope (Quinlan et al. 2017). Plectin reinforces this network also by connecting keratins to desmosomes and hemidesmosomes, which are responsible for maintaining tissue cohesion (Prechova et al. 2022).

The role of plectin in cytoskeletal cross-linking is especially important in tissues subjected to mechanical stress. Under tension or compression, plectin helps maintain the integrity of the cytoskeletal network by stabilizing intermediate filaments and facilitating force transmission across the cell. *In vitro* studies of epithelial cells, such as Madin-Darby canine kidney (MDCK) cells, have shown that plectin supports the formation of the submembranous keratin rim, a structure critical for the spatial distribution of mechanical forces throughout the cell (Prechova et al. 2022). Loss of plectin results in a breakdown of this cytoskeletal network, leading to increased susceptibility to mechanical damage and compromised cell function (Osmanagic-Myers et al. 2006; Kah et al. 2021; Krausova et al. 2021; Prechova et al. 2022).

Plectin's role in anchoring intermediate filaments to cell adhesion structures is central to maintaining epithelial cell cohesion. At the molecular level, plectin binds keratin filaments to desmosomes and hemidesmosomes, ensuring the stability of epithelial sheets under mechanical load (Ketema et al. 2013). In addition to its structural role, plectin modulates the dynamic interactions between cytoskeletal components and cell adhesion complexes (Moch and Leube 2021; Walko, Castanon, and Wiche 2015). Studies have shown that plectin-knockout epithelial (PLEKO) cells exhibit impaired cell-cell adhesion, leading to weakened intercellular junctions and compromised barrier function. This highlights the critical role of plectin in regulating epithelial mechanics and suggests that plectin dysfunction may contribute to the pathogenesis of diseases characterized by epithelial fragility (Krausova et al. 2021; Osmanagic-Myers, Dechat, and Foisner 2015; Prechova et al. 2022).

Beyond its structural functions, plectin also acts as a scaffold for signaling pathways that regulate cytoskeletal dynamics and cellular responses to stress (Gregor, Zeöld, et al. 2006; Zheng and Cantley 2007). One of the key pathways influenced by plectin is the AMPK pathway. Plectin interacts with AMPK to coordinate cytoskeletal reorganization and preserve cell polarity under challenging conditions. In fibroblasts, for instance, plectin-mediated interactions between actomyosin and vimentin filaments at focal adhesions are crucial for

maintaining cell shape and migration during mechanical stress (Gregor, Osmanagic-Myers, Burgstaller, Wolfram, Fischer, Walko, Resch, Jörgl, et al. 2014).

Additionally, -plectin has been shown to regulate the p38 MAPK pathway, a key player in the cellular stress response (Osmanagic-Myers et al. 2006). Plectin-knockout cells PLEKO exhibit abnormal activation of p38 kinase in response to mechanical stress, leading to cytoskeletal instability and increased susceptibility to cell death. These findings suggest that plectin not only maintains the structural integrity of the cytoskeleton but also modulates the cellular signaling pathways that govern stress responses, further underscoring its importance in preserving cellular homeostasis.

1.2.2.3 Plectin-associated pathologies

Over 100 mapped mutations in the human plectin gene are implicated in plectinopathies, a diverse group of multisystem disorders that predominantly affect tissues exposed to mechanical stress, such as skin, muscle, and the gastrointestinal tract (Wiche 2022; Vahidnezhad et al. 2022). Among these, epidermolysis bullosa simplex (EBS) is the most prevalent, characterized by severe, early-onset skin blistering due to compromised cellular integrity. Autosomal recessive forms of EBS often involve additional complications, including muscular dystrophy (EBS-MD), myasthenic syndrome (EBS-MD-MyS), pyloric atresia (EBS-PA), and congenital myasthenia (EBS-CMS). These variants frequently result from mutations in exon 31 of plectin gene, which encodes the rod domain essential for plectin's structural role, leading to nonsense-mediated mRNA decay and reduced protein levels (reviewed in (Castañón et al. 2013; Winter and Wiche 2013). In contrast, the autosomal dominant EBS-Ogna, caused by a specific missense mutation in exon 31, presents predominantly as skin fragility without additional systemic complications, illustrating how different mutations within the same gene can produce distinct clinical outcomes (Castañón et al. 2013; Pfendner, Rouan, and Uitto 2005). This variability underscores the complex genotype-phenotype correlations associated with plectin gene mutations and highlights the need for a better understanding of how specific mutations influence plectin's structural and functional roles.

Strikingly, three recently published case reports from Taiwan (Wu et al. 2019), France (Thebaut et al. 2024), and Thailand (Kor-Anantakul et al. 2024) have documented severe cholestatic liver disease in infants with plectin mutations, all of whom required liver transplantation or succumbed to liver failure These reports will be discussed in more detail in Chapter 1.7. In brief, plectin mutations disrupt the cytoskeletal organization of hepatocytes,

compromising the localization and function of key bile transporters such as ABCB11 and MRP2. This impaired bile transport leads to cholestasis, where bile cannot be properly secreted, resulting in progressive liver damage. Furthermore, the variability in the clinical presentations and histological findings among cases highlights the potential for specific plectin gene mutations to cause varying degrees of liver injury, depending on the affected domain of the plectin protein.

1.2.2.4 Polarized protein trafficking

Cytoskeletal components and cell-cell adhesion are closely involved in protein trafficking within hepatocytes, both playing essential roles in preserving cellular polarity and integrity. The cytoskeleton provides not only structural support but also facilitates the directed movement of vesicles within the cell. Additionally, cell-cell adhesion complexes ensure the precise spatial organization of membrane proteins, maintaining the correct distribution across different cellular domains (reviewed in (Gissen and Arias 2015)).

The trans-Golgi network serves as the primary sorting hub, directing newly synthesized proteins to their appropriate destinations (Kipp and Arias 2000). In hepatocytes, the accurate targeting of membrane proteins to specific regions of the plasma membrane, such as the basolateral or apical (canalicular) domains, is essential for the proper functioning of the liver (Wakabayashi, Kipp, and Arias, 2006; Wojtal et al., 2006). Polytopic membrane proteins, such as ATP-binding cassette (ABC) transporters, are directly targeted to the bile canaliculi from the Golgi, or alternatively through the Rab11a recycling endosome pool (Wakabayashi et al., 2005). In contrast, single-pass transmembrane proteins (like dipeptidyl peptidase IV/ DPP4) and glycosylphosphatidylinositol-anchored proteins undergo transcytosis, being first directed to the basolateral plasma membrane before reaching the apical (canalicular) domain via endosomes (Kipp and Arias, 2000b; Polishchuk et al., 2014).

Several key players in hepatocyte trafficking have been identified, including tight junction proteins such as claudins, occludins, and zonula occludens proteins. Moreover, Rab proteins, particularly Rab11a and Rab35, and other endosomal components such as myosin Vb, are also critical in determining the localization of various membrane proteins. Mutations in genes encoding recycling endosome-associated proteins, like myosin Vb, have been linked to disorders such as microvillus inclusion disease and arthrogryposis, renal dysfunction, and cholestasis, underscoring the importance of the recycling-endosome machinery in maintaining hepatocyte polarity (Qiu et al., 2017). Interestingly, Belicova et al. (2021) demonstrated that

Rab35-positive vesicle clusters accumulate at the base of canalicular load-bearing structures, known as apical bulkheads (Belicova et al. 2021). Their findings suggest that Rab35 is essential for the formation and dynamic remodeling of these structures. This points to a possible coordination between vesicle trafficking and actin cytoskeleton organization, potentially involving the regulation of actin remodeling, as has been observed in neurons (Bhat et al., 2020).Together these findings highlight the complexity of protein trafficking and the interplay between vesicle transport, cytoskeletal dynamics, and cell polarity in hepatocytes (Treyer and Musch, 2013; Schulze et al., 2019).

1.2.3 Biliary tree

The biliary network, commonly referred to as the biliary tree (Figure 6A), serves as a conduit for bile, connecting the hepatocellular parenchyma of the liver to the lumen of the duodenum in the small intestine, facilitating the transport of bile essential for digestion. Hepatocytes secrete bile into bile canaliculi. These bile canaliculi drain bile into the interlobular ducts ensuring efficient bile flow from the liver to the intestine. Together, series of branching bile ducts are known as the biliary tree.

In the human liver anatomy, the classification of biliary epithelium branches follows Ludwig's original proposal from 1987, based on bile duct diameter (Figure 6B, (Ludwig 1987)).

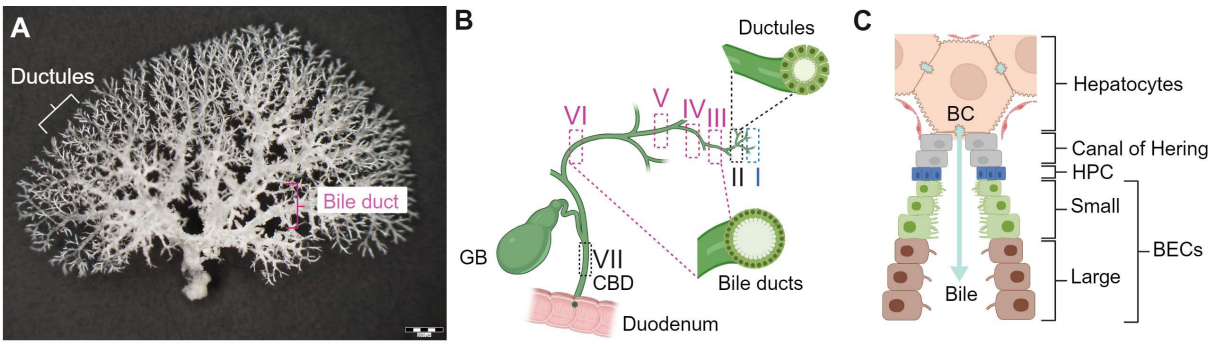

Figure 6. *Biliary tree*. A 3D-branching ductal network with increasing diameter that drains bile from hepatocellular parenchyma and transports it to duodenum. **(A)** Acrylic resin cast of murine biliary tree of left lateral lobe. Scale bar, 2 mm. The resin cast was prepared in the Laboratory of integrative biology at IMG by Helena Havelkova. **(B)** Biliary tree scheme of Ludwig's clasification categories based on diameter. This classification categorizes bile ducts (BD) into the canal of Hering (I), ductules (II), small BD (interlobular BD (III); septal BD (IV)), large BD (area ducts (V); segmental ducts (VI; 400 - 800 µm)) and common BD (CBD; VII) ultimately, these conduits deliver bile to the gallbladder (GB) and duoedenum. **(C)** Small scale schematic of biliary tree. The bile produced by hepatocytes is transported to BC. The canal of Hering, lined by both hepatocytes and BECs (grey), serves as a physical continuum between the bile canaliculi and the biliary tree (ductules; small BD; large BD). A hepatic progenitor cell (HPC, blue) niche reside at the interface of the canal of Hering and the parenchyma. BD shows significant biological differences among BECs subpopulations lining ducts of various sizes small BECs (green) and large BECs (brown). Adapted from (Boron and Boulpaep 2016). Created in BioRender.com.

This classification categorizes bile ducts into bile ductules (<15 μm), interlobular bile duct (15 - 100 μm), septal bile duct (100 - 300 μm), area (or zonal) ducts (300 - 400 μm), segmental ducts (400 - 800 μm), and hepatic ducts (above 800 μm). The canal of Hering, lined by both hepatocytes and BECs, acts as a bridge between the bile canaliculi and the biliary tree (Figure 6C). At the periphery of the biliary epithelium, bile ductules, composed entirely of BECs, transition into the canal of Hering, facilitating the flow of bile.

Beyond classification purposes, distinguishing bile ducts by diameter, reveals significant biological differences among BEC subpopulations lining ducts of various sizes. Previous research on BECs isolated from normal rat liver revealed two distinct subpopulations: small cholangiocytes (8 μm diameter) and large cholangiocytes (14 μm diameter) (Alpini et al. 1996). Small cholangiocytes were associated with ducts smaller than 15 μm in diameter, while large cholangiocytes were found in ducts larger than 15 μm. This pattern was consistent in both isolated small and large bile ducts units from rat liver (Alpini et al. 1996). Similar to rats, the intrahepatic BECs in mice exhibit both morphological and functional heterogeneity. The smallest bile ductules are lined by four to five cholangiocytes, which form a cohesive epithelial barrier. These cholangiocytes are interconnected by tight junctions, with microvilli projecting into the bile duct lumen to increase the absorptive and secretory surface area. As these ductules converge, they form interlobular ducts with a cross-sectional diameter ranging from 20 to 100 μm. In the larger bile ducts, cholangiocytes become more prominent, adopting a larger and more columnar shape to accommodate increased bile flow (Glaser et al. 2009). Additionally, morphological studies showed that nucleus-to-cytoplasm ratio of cholangicytes decreased inversely with duct size, with cells transitioning from cubic to columnar shapes, confirming the presence of two distinct cholangiocyte subpopulations shaping the biliary tree (Lleo et al. 2014). The large ducts are forming the common bile duct (CBD). In human adults, the CBD typically measures around 7 cm in length and 0.5 to 1.5 cm in diameter. In most cases, the CBD merges with the pancreatic duct before forming the ampulla of Vater. This common channel, as it passes through the duodenal wall, is surrounded by a thickened of smooth muscle layers, known as the sphincter of Oddi. This sphincter regulates bile flow by constricting the BD lumen. In humans, the total length of biliary tree is estimated to be ~2 km (Boron and Boulpaep 2016).

1.2.3.1 Bile canaliculi microarchitecture

The bile canaliculi represent the very beginning of the biliary tree, where bile secretion from hepatocytes first occurs. These tiny, tubular structures are formed by the invagination of the apical domains of adjacent hepatocyte´s plasma membranes, creating a network that channels bile toward the biliary system. The surface of the bile canaliculi is further amplified by numerous microvilli. The detailed structure of the bile canaliculus was first thoroughly described by Tsukada et al. (1995) (Figure 7), who used immunoblotting and electron microscopy techniques to characterize the distribution of cytoskeletal proteins within the bile canaliculi of normal human hepatocytes (Tsukada, Ackerley, and Phillips 1995).

Initially, three distinct regions of filamentous actin (F-actin) organization were described: (1) microvillus core filaments, these include villin and form the core structure of the microvilli; (2) membrane-associated microfilamentous network, this network provides structural support to the bile canaliculi; (3) circumferential pericanalicular actin filament band, this band contains a contractile actomyosin cortex and an intermediate filament network outer sheath, both anchored to cell-cell junctions. The actin filaments are associated with ezrin-radixin-moesin family proteins and junctional proteins. Intermediate filaments are anchored into desmosomes, likely stabilizing the canalicular compartment (Tsukada et al, 1995; Meyer et al, 2020; Fu et al, 2010; Cacho-Navas et al, 2022; Musch, 2014). However, the exact functions of intermediate filaments within the bile canaliculi need further elucidation.

Microtubules are present in the cytoplasm adjacent to the pericanalicular band (Tsukada, Ackerley, and Phillips 1995).

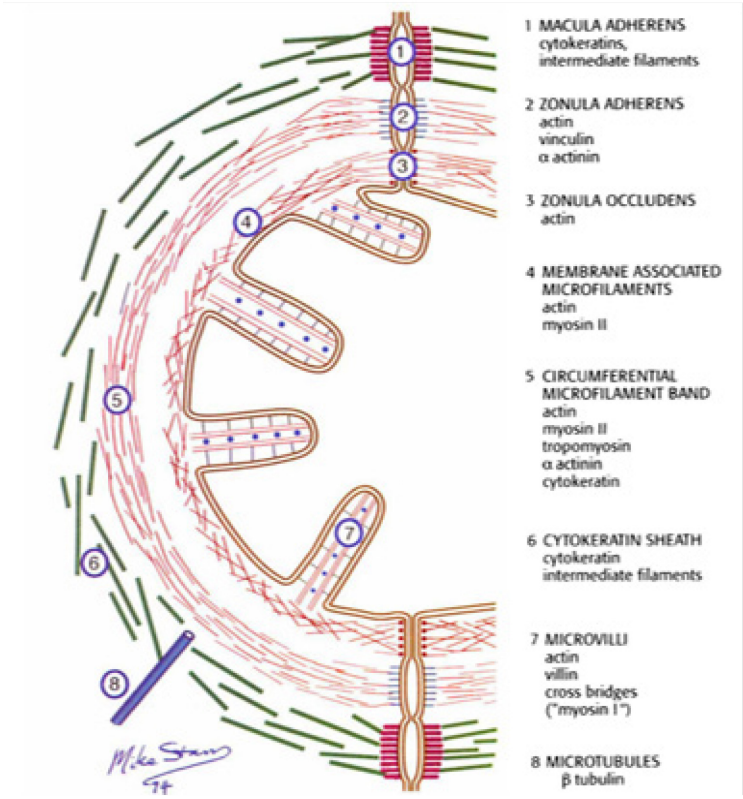

Figure 7. *Bile canaliculi microarchitecture*. Scheme of the bile canalicular (BC) architecture proposed by Tsukada et al. The bile canaliculus is cytoskeleton-rich structure containing actin filamnets in circumferential actomyosin cortex and microvilli (4; 5; 7), intermediate filaments (e.g. keratins) in the pericanalicular sheat (6), and microtubules in cytoplasm (8). The BC is sealed by cell-cell junctions (desmosomes, 1; adherens junction, 2; tight junction, 3). By using immunoblots Tsukada and el. show protein composition of individual microdomains of bile canaliculus (Tsukada, Ackerley, and Phillips 1995).

Actin-binding proteins, in particular, regulate the dynamic structure of the bile canaliculi, supporting hepatocyte function and liver homeostasis (Tsukada, Ackerley, and Phillips 1995).

Lumenogenesis, the process of lumen formation, occurs differently between liver epithelial cells. BECs form isotropic bile ducts, contributing to the biliary tree, while hepatocytes exhibit complex polarity, forming a branched, anisotropic bile canalicular network (Scholich et al. 2020; Datta, Bryant, and Mostov 2011; Bryant et al. 2010; Dasgupta et al. 2018). These structures rely heavily on cytoskeletal organization and polarized intracellular trafficking of proteins and lipids (Meyer et al. 2020). This difference in lumen formation

reflects the distinct roles of hepatocytes and BECs in bile secretion and flow (Tanimizu, Miyajima, and Mostov 2007; Antoniou et al. 2009).

1.2.3.1.1 The bile canaliculi lumen formation

The formation of the bile canalicular lumen begins during the developmental stages of the fetal and neonatal liver and recurs during liver regeneration following injury (Gissen and Arias 2015). In the embryonic phase, hepatoblasts initially lack polarity, but later polarize and aggregate into a central, lumen-containing cluster. This is followed by a transition to a multipolarized state, which is essential for the development of an interconnected bile canaliculi network (Feracci et al. 1987). The progression to a fully mature bile canalicular network depends on a combination of molecular cues and physical forces, both internal and external (Dasgupta et al. 2018; Deharde et al. 2016; Datta, Bryant, and Mostov 2011).

Internally, key molecular regulators of cell polarity, first identified in *Drosophila melanogaster*, guide the specification of future polarization domains in differentiating epithelial cells (Mostov 2003). For example, the Crumbs complex (Flores-Benitez and Knust 2015; Franz and Riechmann 2010) establishes apical identity and is linked to the partitioning defective (Par) complex (Nance and Zallen 2011; Campanale, Sun, and Montell 2017), which promotes tight junction formation and apical membrane targeting. On the other hand, the Scribble complex defines the basolateral domain (Rabino et al. 2024).

Externally, cues from the microenvironment help break cell symmetry, organize the actomyosin cortex, and direct protein trafficking. Tight junctions and polarity complexes further facilitate the segregation of membrane proteins into distinct apical, basal, and lateral domains (Gissen and Arias 2015). A key question is whether polarity establishment relies solely on external signals acting on individual cells or whether it involves collective responses from neighboring cells (Akhtar and Streuli 2013; Bryant and Mostov 2008). In a study by Zhang et al. (Zhang et al. 2020), primary hepatocytes cultured in synthetic microenvironments were shown to develop independent secretory apical poles, with junctional complexes and polarity markers forming at the single-cell level. This process relies on actomyosin cortex rearrangements, initiated by cadherin-mediated adherent junctions at early lateral cell-cell contacts, rather than neighboring cell responses (Zhang et al. 2020).

In vivo, lumen formation in organs can occur through various mechanisms, including wrapping, budding, cavitation, cell migration, and cord hollowing (Malinen et al. 2012; Wang et al. 2013; Deharde et al. 2016). Studies show a correlation between the 3D structure of bile

canaliculi and their elongation, guided by an anisotropic distribution of intercellular forces (Zhang et al. 2020; Navis and Nelson 2016). This contrasts with the previously suggested role of heterogeneous membrane adhesion in promoting elongation (Baum and Georgiou 2011; Datta, Bryant, and Mostov 2011).

Belicova et al. (2021) identified high-density actin structures within the bile canaliculi lumen, arranged in a quasi-periodic pattern and resembling bulkheads, which they named as apical bulkheads. (Belicova et al., 2021).

1.2.3.1.2 Apical bulkheads

Belicova et al. (2021) demonstrated that apical bulkheads are finger-like membrane extensions, sealed by tight junctions, that maintain the continuity of the bile canalicular lumen without forming separate compartments (Figure 8A - F) (Belicova et al. 2021). These structures consist of organized actin filaments, along with circumferential actin belts and microvilli, providing mechanical stability to prevent canaliculi expansion under pressure. In cholestasis,

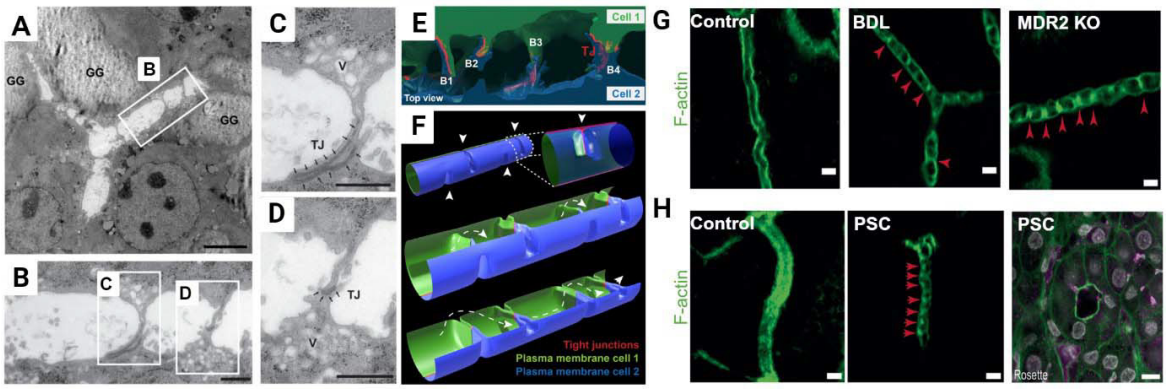

Figure 8. *Apical bulkheads as defined by Belicova et al.* **(A)** Trasmission electron micrographs of branched bile canaliculus (BC) between three hepatocytes sealed by tight junction (TJ), glycogen granules (GG). Scale bar, 2 µm **(B)** Detailed images of the white rectangle in (A), and images **(C)** and **(D)** are magnified versions of the corresponding white rectangles in (B). Membrane connections are formed by apical domains of both cells lining the bile canaliculi sealed by TJ (arrows). Vesicles (V); scale bar, 1 µm. **(E)** and **(F)** simplified mathematical model of bile canaliculus with periodic apical bulkhead (AB) membrane protrusion in the lumen (arrowheads). Dashed arrow shows direction of the bile flow. **(G)** High-resolution imaging of individual bile canaliculi in healthy mouse liver tissue, after the bile duct ligation (BDL) surgery, and multidrug-resistance-associated protein 2 knockout (*MDR2KO)* mouse. Immunofluorescence for F-actin (green). Scale bar, 10 µm. The AB are highlighted with red arrowheads. **(H)** High-resolution imaging of F-actin (green) showing individual BC in control or primary sclerosing cholangitis (PSC) human liver tissue. Moreover liver cell rosettes in PSC patients are formed by hepatocyte-like cells. Red arrowheads mark AB. Scale bar, 2 µm. Created using data of (Belicova et al. 2021; Mayer et al. 2023; Bebelman et al. 2023).

the liver adapts by inserting apical bulkheads, enhancing canalicular mechanical resistance and preserving bile flow despite elevated intraluminal pressure (Belicova et al., 2021; Mayer et al., 2023).

In liver diseases such as primary sclerosing cholangitis (PSC), increased bile stasis leads to dilated bile canaliculi, which in turn promotes the appearance of apical bulkheads and the formation of liver cell rosettes (Figure 8H). This adaptive response has also been observed cholestatic mouse models, including bile duct ligation (BDL) and MDR2-knockout (*MDR2KO*) mice, underscoring the role of apical bulkheads in preserving bile canalicular integrity under conditions of elevated bile pressure (Figure 8G) (Mayer et al., 2023). The dynamic organization of the actomyosin cytoskeleton is essential for forming and maintaining apical bulkheads, which protect the liver from bile-induced damage during impaired bile flow (Bebelman et al., 2023). Understanding their structure and function provides key insights into the liver's adaptive responses to mechanical and toxic stress in cholestatic diseases.

1.2.4 Biliary epithelial cells

The BECs are a type of epithelial cell that are found in both the intrahepatic and extrahepatic bile ducts, having undergone specialisation for the purposes of their function. Despite representing only 3 - 5% of the total liver mass, these cells play a vital role in the liver physiology, particularly in regulating bile acid synthesis and its transport. The BECs contribute to regulation of the fluidity and alkalinity of canalicular bile by secreting electrolytes, primarily chloride (Cl^-) and bicarbonate (HCO_3^-). Regulation of fluidity and alkalinity is essential for maintaining the equilibrium of bile acids, which are critical for the digestion and absorption of fats and for the excretion of cholesterol and other waste products. Integrity and functionality of cholangiocytes are vital for these processes; impairment of these cells can result in significant pathological conditions such as cholestasis (Boron and Boulpaep 2016).

Like other epithelial cells, BECs are polarized with distinct apical and basal plasma membrane domains and multiple transport functions, many of which are related to bile secretion (Figure 9). The establishment of osmotic gradients enhances the bile flow by inducing the secondary secretion of water. A several of membrane transport proteins and channels have been identified and described in the BECs. They facilitate the transport of bicarbonate into the bile (the Na^+-independent Cl^-/HCO_3^- exchanger; anion exchanger 2 (AE2)). AE2 functions as a secondary active transporter, driven by the high luminal concentrations of Cl^- (generated via a cyclic adenosine monophosphate (cAMP)-stimulated low-conductance Cl^- channel; cystic fibrosis transmembrane conductance regulator (CFTR)). Furthermore, water is transported

from the BECs into bile by the water-channel protein aquaporin 1 (AQP1). These secretory processes are regulated by a gastrointestinal hormone, secretin and have impact in bile fluidity and alkality. Recently, it was shown that transporters are stored in the same intracellular vesicles within BECs, and that upon secretin stimulation, they are dynamically trafficked to the apical membrane.

In healthy liver, the BECs play an important role in (I) bile modification and (II) forming a barrier. The bile secretion is regulated by external signals (peptides, nucleotides,

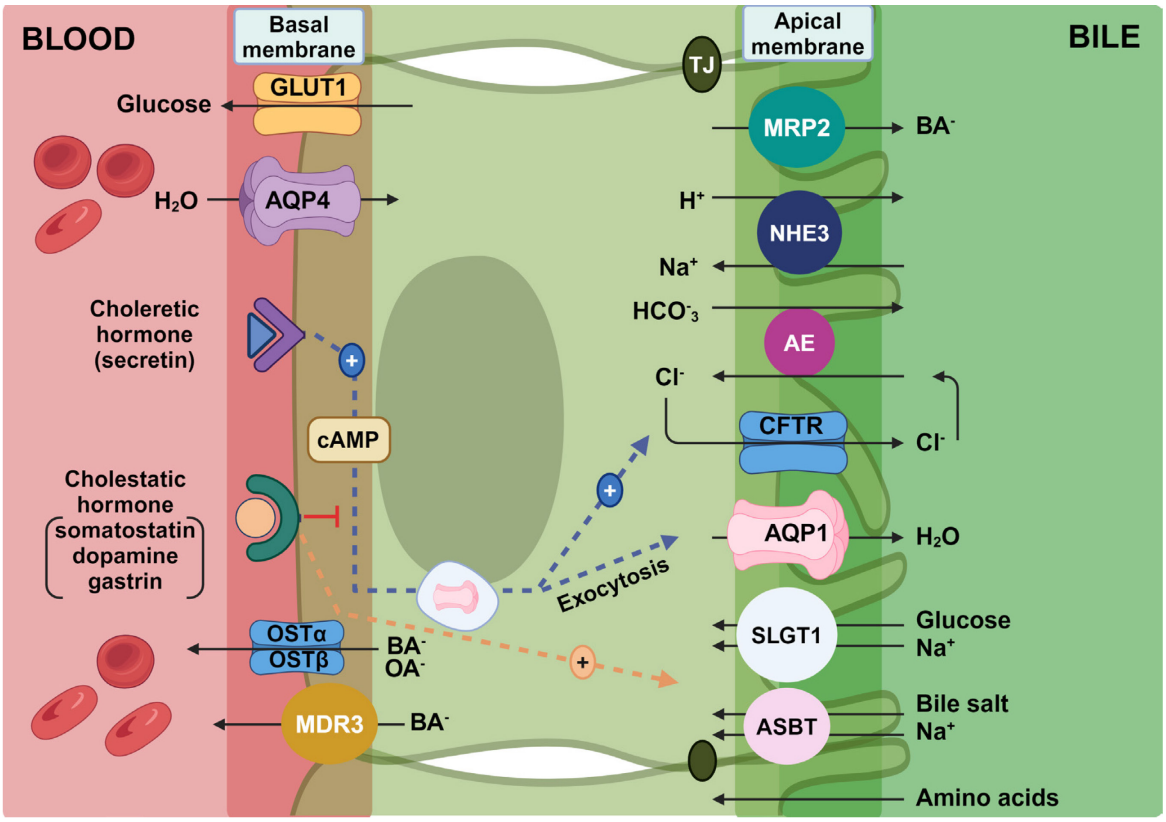

Figure 9. *The system of BEC transporters and channels*. Bile duct (BD) is sealted by tight junctions (TJs). The transports are associated with multiple transporters, exchangers, and channels expressed on the apical and basal plasma membrane domains of cholangiocytes. An elevation in intracellular cAMP or Ca^{2+} activates cystic fibrosis transmembrane conductance regulator (CFTR), or the Ca^{2+}-activated chloral channel, TMEM16A, resulting to the transport of Cl^- into the BD lumen. The anion-exchange protein 2 (AE2), provides HCO_3^- secretion into the BD lumen in exchange for Cl^-; HCO_3^- secretion is followed by osmotically driven transport of H_2O into the BD lumen via aquaporin 1 (AQP1). The AQP1-mediated H_2O transport from the BD lumen is a consequence of glucose and bile acid (BA) absorption by sodium-glucose transport protein 1 (SGLT1) and apical sodium-bile acid transporter (ASBT), respectively. At the basolateral plasma membrane domain, H_2O moves into and out via AQP4 and glucose is transported via glucose transporter 1 (GLUT1). Hormone secretin stimulates the apical insertion of intracellular vesicles containing AE2, CFTR, and AQP1, resulting in Cl^-secretion through CFTR that is exchanged with bicarbonate via AE2, whereas somatostatin, dopamine, and gastrin inhibit this process. Organic solute transporter (OST), α/β, multidrug resistance-associated protein 2 (MRP2), and multidrug resistance protein 3 (MDR3) are localised on basolateral membrane of cholangiocytes and are responsible for transport of bile acid salts and organic anionts. Sodium-hydrogen exchanger 3 (NHE3) is localized at apical membrane and it is responsible for fluid absorption. Created in BioRender.com.

hormones, and neurotransmitters), biliary constituents (bile acids, glucose, and vesicles) and physical forces (bile flow and pressure) that are reflected in various internal signaling pathways.

Large cholangiocytes are equipped with a specialized antenna-like structure known as the primary cilium (Figure 10). This organelle contains receptors and ion channels that detect changes in bile composition and flow, sensing mechanical, chemical, and osmotic stimuli. These stimuli activate signaling pathways that regulate both bile flow and composition (Scheuerle et al. 2023).

Under healthy conditions, BECs remain in a quiescent state, forming stable epithelial sheets and tubules. However, during liver injury, they become activated and contribute to dynamic regeneration, playing a crucial role in the pathobiology of various liver diseases (Raven et al. 2017). When hepatocyte regeneration is impaired, BEC proliferation becomes essential for liver recovery (Morell, Fabris, and Strazzabosco 2013; Alvaro et al. 2007). A

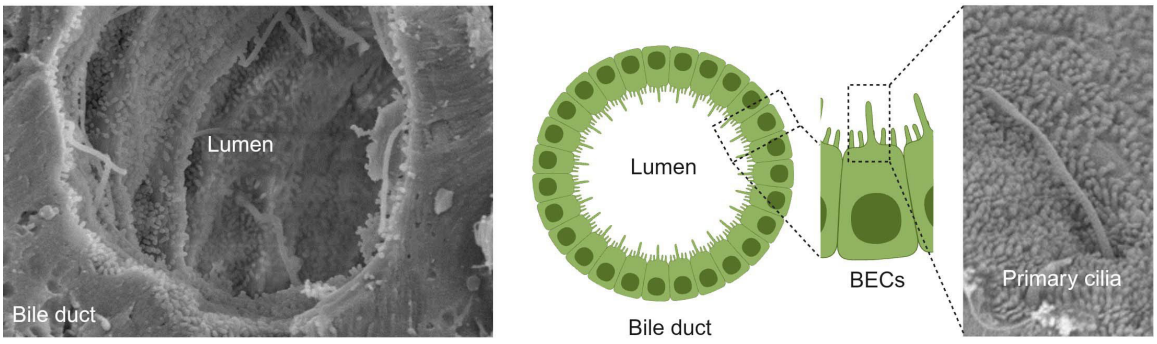

Figure 10. *Bile duct lumen and primary cilia.* SEM micrographs of bile duct, lumen is indicated, and its sceme. Enlarged ciliated apical plasma membrane of BEC, shown by SEM micrographs and scheme. SEM micrographs acquired in collaboration with Dr. Benada, Institute of Microbiology of the CAS. Created in BioRender.com

hallmark of liver injury is the ductular reaction, a phenomenon characterized by the proliferation of BECs and the expansion of bile ducts, often accompanied by fibrosis and inflammation. This reaction serves as a compensatory mechanism, providing a pool of bipotential progenitor cells capable of differentiating into both hepatocytes and cholangiocytes, particularly when hepatocyte function is compromised (Michalopoulos 2007). The ductular reaction is commonly observed in a wide array of liver diseases, including cirrhosis, cholestasis, and chronic hepatitis, and it is frequently seen in both human liver pathologies and animal models (Michalopoulos and DeFrances 1997).

Importantly, this process is closely linked to the activation of several key signaling pathways, such as the Wnt/β-catenin and Notch pathways, which regulate progenitor cell activation and differentiation during liver repair via their interactions with activated myofibroblasts or macrophages (Strazzabosco and Fabris 2013). While the ductular reaction is a vital response to liver injury, its persistence is often associated with progressive liver disease and fibrosis, underscoring the complex balance between regeneration and pathological remodeling in the liver (Sato et al. 2019).

Numerous factors, including genetic mutations, infectious agents, autoimmune disorders, and vascular diseases, can compromise the structural and functional integrity of cholangiocytes, the epithelial cells lining the bile ducts. This disruption often leads to bile stasis (cholestasis), which triggers inflammatory and fibrotic processes. Over time, these processes can extend beyond the biliary system, causing portal fibrosis, which may eventually result in widespread hepatic dysfunction, cirrhosis, and liver failure.

These conditions, collectively known as cholangiopathies, encompass a group of chronic, progressive diseases affecting the biliary tree. Examples include PSC, primary biliary cholangitis (PBC), and biliary atresia. Cholangiopathies present unique challenges in clinical hepatology due to their complex pathogenesis and lack of curative treatments. While cholangiopathies are individually rare, their cumulative impact on patient morbidity and mortality is substantial, with no curative therapies currently available beyond liver transplantation.

For instance, PSC, a chronic autoimmune disease that causes progressive inflammation and scarring of the bile ducts, often leads to liver failure. PSC is a leading indication for liver transplantation, accounting for approximately 10 - 15% of all liver transplants in the United States and Europe. Despite its prevalence among cholangiopathies, the pathogenesis of PSC remains poorly understood, and no effective medical therapies have been developed to halt or reverse disease progression. This highlights the urgent need for novel therapeutic strategies targeting the underlying mechanisms of cholangiopathies, beyond the current options focused on symptom management and transplantation (European Association for the Study of the Liver. Electronic address and European Association for the Study of the 2022).

1.3 Liver functions

The liver is a multifunctional organ essential for maintaining homeostasis, with key roles in metabolism, detoxification, and biosynthesis (Figure 11). It regulates carbohydrate metabolism by storing glucose as glycogen and releasing it during periods of energy demand. In lipid metabolism, the liver synthesizes cholesterol, lipoproteins, and triglycerides while breaking down fatty acids for energy production. The liver is also central to protein metabolism, producing vital plasma proteins such as albumin, which regulates oncotic pressure, and clotting factors that are critical for hemostasis. Additionally, it plays a crucial role in the detoxification of harmful substances, including drugs, alcohol, and metabolic waste, converting them into excretable forms via enzymatic pathways. The liver also produces bile, necessary for the emulsification and absorption of dietary fats in the intestines. Furthermore, the liver participates in the breakdown of old erythrocytes and the recycling of iron, contributing to blood regulation. Collectively, these functions underscore the liver's indispensable role in maintaining physiological balance and responding to both metabolic and toxic challenges (Boron and Boulpaep 2016).

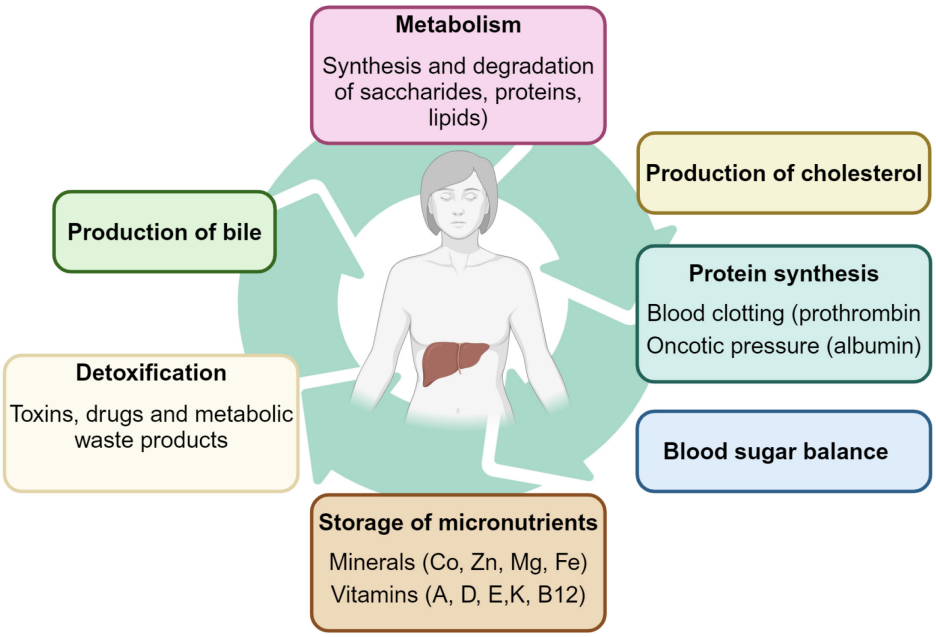

Figure 11. *Liver functions*. Adapted from (Boron and Boulpaep 2016). Created in BioRender.com.

1.4 Bile formation and secretion

Bile is a complex aqueous secretion produced by hepatocytes and modified as it passes through absorptive and secretory transport systems within BECs. Upon reaching the gallbladder, bile is concentrated before being either stored or delivered into the intestinal lumen. Composed of approximately 95% water, bile contains numerous solid constituents, including bile acids, bilirubin, phospholipids, cholesterol, amino acids, steroids, enzymes, porphyrins, vitamins, heavy metals, as well as exogenous substances like drugs, xenobiotics, and environmental toxins (Table 1) (Boron and Boulpaep 2016).

Parameter	Concetration in hepatic bile
pH	7.5
Na^+	141-165 mM
K^+	2.7-6.7 mM
Ca^{2+}	1.2-3.2 mM
Cl^-	77-117 mM
HCO_3^-	12-55 mM
Total phosphorous	0.15 g/L
Bile acids	3-45 g/L
Totall Fatty acids	2.7 g/L
Billirubin	1-2 g/L
Phospholipids	1.4-8.1 g/L
Cholesterol	1-3.2 g/L
Proteins	2-20 g/L

Table 1: *Bile composition.* Adapted from (Boyer et al. 2012)

As Boyer et al. reviewed, the bile serves several critical functions (Boyer and Soroka 2021):

(1) Excretion of harmful substances. Bile acts as a primary excretory route for potentially toxic exogenous lipophilic compounds, as well as endogenous substrates like bilirubin and bile salts. These substances typically have molecular weights exceeding 300 to 500 Da, which makes them unsuitable for renal excretion.

(2) Emulsification of dietary lipids. Bile salts, the principal organic solutes in bile, play a key role in emulsifying dietary fats, aiding their digestion and absorption in the small intestine.

(3) Cholesterol elimination. Bile is the main pathway through which cholesterol is removed from the body, thus preventing its accumulation.

(4) Protection against infections. Bile contributes to the defense against enteric infections by excreting immune factors such as IgA and inflammatory cytokines, as well as activating the innate immune response within the gut.

(5) Cholehepatic and enterohepatic circulation. Bile is integral to the recycling of bile salts and other solutes between the liver and intestine through cholehepatic and enterohepatic circulation.

(6) Excretion of hormones and pheromones. Many hormones and pheromones are excreted in bile, influencing the growth and development of the intestine in some species and serving as attractants for weaning in non-human vertebrates.

1.4.1 Bile flow

Recent reports have reignited the long-standing scientific debate about the mechanisms governing the transport of glandular secretions, such as saliva, bile, and exocrine pancreatic juice. In the context of bile flux, the liver can be divided into two functional domains: the bile canalicular network and the biliary tree. Hepatocytes contribute to both bile salt-independent and bile salt-dependent flow, while ductal secretion is mediated by BECs (Boyer and Soroka 2021).

Traditionally, bile secretion was thought to occur through active solute transport by hepatocytes, resulting in an osmotic gradient that draws water into the bile canaliculi, thereby generating bulk canalicular fluid flow (Boyer and Klatskin, 1970). However, recent studies challenge this model, showing a lack of measurable flow within the bile canaliculi. Instead, bile acids may move primarily via molecular diffusion until they reach the bile ducts, where true fluid flow emerges due to local secretion of inorganic ions. This ion-driven osmotic process draws water from cholangiocytes into the bile duct lumen (Boyer and Soroka, 2021; Gupta, 2023).

Additionally, ductal bile flow is also osmotically driven, primarily by the secretion of bicarbonate (HCO_3^-) and other ions. A pseudolinear relationship exists between bile acid concentration and extrahepatic bile flow, with different bile acid derivatives demonstrating varying choleretic potentials (Meyer et al. 2017).

The proper functioning of bile flow relies on the integrity of tight junctions and cytoskeletal elements in both hepatocytes and BECs, which maintain the directional secretion of bile. Disruptions in these structures, whether due to genetic mutations in junctional proteins, transporters, or cytoskeletal components, as well as inflammation or obstruction, can result in cholestasis. This condition, characterized by the accumulation of bile acids in the liver, can lead to liver damage and systemic toxicity. Understanding the mechanisms regulating bile flow is crucial for diagnosing and treating liver diseases associated with impaired bile production and transport.

1.5 **Pathophysiology of cholestatic liver disease**

Cholestasis induces a range of pathophysiological changes that impact both hepatocytes and cholangiocytes, disrupting bile flow and leading to liver damage, inflammation, and fibrosis. These processes are tightly linked to the cytoskeletal remodeling in both cell types, which plays a key role in maintaining structural integrity and bile secretion under stress (Jungst et al. 2013).

In hepatocytes the bile canaliculi are surrounded by the peri-canalicular F-actin cortex, which is essential for maintaining the contractility and stability of these channels (Tsukada, Ackerley, and Phillips 1995). During cholestasis, increased biliary pressure forces hepatocytes to undergo cytoskeletal remodeling, as described by Gupta et al. (2023), where actomyosin contraction driven by calcium signaling helps preserve the bile canalicular structural integrity (Gupta 2023). This remodeling prevents bile canaliculi dilation and bile leakage, allowing the liver to manage the elevated pressure.

Belicova et al. (2021) highlighted the role of apical bulkheads, which emerge from adjacent hepatocytes and act as load-bearing elements across the bile canalicular lumen (Belicova et al. 2021). These bulkheads are composed of organized actin filaments and provide mechanical reinforcement, preventing excessive canaliculi expansion and maintaining bile flow during cholestatic conditions (Mayer et al. 2023). The bulkheads are especially important under elevated intraluminal pressure, as they compartmentalize stress within the bile canaliculi and protect the hepatocyte from further injury (Bebelman et al. 2023).

In addition to actin, keratins (particularly hepatic K8/K18) play an important role in cellular stability during cholestasis (Omary, Ku, and Toivola 2002). Under stress, these keratins undergo post-translational modifications like phosphorylation and sumoylation, leading to the formation of Mallory-Denk bodies, which signify cellular injury (Zatloukal et al. 2007; Snider et al. 2011). The aggregation of keratin filaments reduces hepatocyte resilience to bile acid toxicity (Zatloukal et al. 2007).

BECs also undergo significant changes during cholestasis. As bile acid accumulation and pressure increase, cholangiocytes activate proliferative and remodeling responses, contribution to the ductular reaction to compensate restricted bile flow by expanding the bile duct network (Michalopoulos 2007). Vartak et al. (2016) described prominent remodeling within the biliary tree as an adaptive response to bile flow obstruction. They observed that the intrahepatic bile ducts undergo structural changes, including increased ductal surface area and

enhanced corrugation, which serve to maximize bile reabsorption and accommodate elevated bile pressure. This remodeling involves the expansion and proliferation of cholangiocytes, which form the lining of the bile ducts, as a means to counteract the effects of cholestatic stress. Additionally, Vartak et al. highlighted that this adaptive remodeling is a dynamic and progressive process, which may help prevent bile duct rupture under conditions of chronic bile retention. However, these changes, while protective in the short term, can contribute to pathological fibrosis if the underlying cholestatic conditions persist (Vartak et al. 2016).

The role of microtubules and vesicular transport is crucial in both hepatocytes and cholangiocytes for trafficking bile transporters such as BSEP, MRP2, and SLC10A1 to the apical membrane (Hutchins and Gollan 2004; Marinelli, Tietz, and Larusso 2005). Disruption of microtubule dynamics during cholestasis impairs this transport, resulting in the mislocalization of bile transporters, further exacerbating bile retention and liver damage (Hutchins and Gollan 2004).

In summary, cholestasis induces profound cytoskeletal changes in both hepatocytes and cholangiocytes. Hepatocytes form apical bulkheads to withstand bile pressure within the canaliculi, while both cell types remodel their actin cytoskeletons to adapt to the increased mechanical stress. These adaptations are critical for temporarily maintaining bile flow and structural integrity but have their limits. Prolonged cholestasis eventually breaches these defenses, leading to progressive fibrosis, cirrhosis, and liver failure.

1.5.1 Rodent models of cholestatic liver disease

Understanding the mechanisms of cholestasis is crucial for developing effective therapies and diagnostics. Large body of research has focused on unraveling the pathophysiology of cholestatic liver injuries and identifying novel strategies for treatment and diagnosis. Animal models play an essential role in these efforts, providing a platform to study disease mechanisms and test therapeutic interventions. These models are selected based on their ability to closely mimic specific aspects of human cholestatic diseases, ensuring the relevance and translatability of research findings.

1.5.1.1 Surgery induced rodent models

One of the most commonly utilized surgery-induced animal models of cholestasis involve BDL, wherein a ligature is placed surgically on the CBD. This procedure induces an obstruction in the extrahepatic biliary system, leading to cholestasis and subsequent

inflammation (Van Campenhout, Van Vlierberghe, and Devisscher 2019). The BDL model is particularly effective in inducing acute extrahepatic obstructive biliary lesions, which closely resemble the pathophysiology seen in clinical conditions such as gallstone liver disease and biliary atresia (Mariotti et al. 2018; Geerts et al. 2008; Garrido et al. 2017). Although BDL primarily causes extrahepatic obstruction, it has been extensively employed to investigate the subsequent pathophysiological changes in hepatic morphology and function resulting from obstructive cholestasis. Consequently, the BDL model has also found utility in studying PSC (Tag, Weiskirchen, et al. 2015; Tag, Sauer-Lehnen, et al. 2015; Pollheimer and Fickert 2015; Pollheimer, Trauner, and Fickert 2011). Initially developed for rats due to their lack of a gallbladder (Mariotti et al. 2018), the BDL model has been successfully used in mice. In mice, BDL leads to jaundice, increased transaminase release, elevated serum bilirubin levels, bile duct proliferation, leukocyte infiltration, and eventual liver fibrosis. Unlike rats and humans, mice exhibit a biliary type of hepatocytic necrosis known as bile infarcts, rather than apoptosis (Miyoshi et al. 1999). Additionally, mice may experience gallbladder dilation and perforation post-BDL, which can be fatal. To mitigate these risks, two strategies are employed: cholecystectomy or placement of a surgical clip on the cystic duct. In recent years, modifications of the BDL model have been developed, including partial BDL and selective BDL (Heinrich et al. 2011; Yokota et al. 2018). Selective BDL involves ligating the left hepatic bile canaliculus before it joins the common bile duct, while partial BDL entails a single ligation around the common bile duct, leaving a defined lumen allowing limited bile flow. Selective BDL offers the advantage of inducing cholestatic injury specifically in the left hepatic lobe, leading to bile infarcts and infiltrating neutrophils (Starkel and Leclercq 2011; Van Campenhout, Van Vlierberghe, and Devisscher 2019).

1.5.1.2 Genetically modified mice models

The advantage of genetically manipulated laboratory mice (*mus musculus*) has ushered researchers into a new era of modeling human diseases. Mice are especially pertinent due to their remarkable similarity to humans in terms of anatomy, physiology, and genetics. Genetically modified mouse models are often colloquially referred to as "spontaneous" models, indicating that they naturally develop the corresponding liver pathology without the need for surgical, toxic, or infectious interventions to induce cholestasis (Gijbels et al. 2021). This term underscores the inherent development of the disease phenotype within these mice without external manipulations. Such models offer invaluable insights into the underlying mechanisms

and progression of human diseases, providing valuable tools for studying and developing potential therapeutic interventions.

For example, it is well known that the malfunctioning of the BSEP, whether due to drug inhibition, internalization, mutations, or altered expression, significantly disrupts bile acid homeostasis and is considered a primary triggering factor of drug-induced cholestasis (Vinken et al. 2013). BSEP-knockout *(BSEPKO)* mice thus represent a valuable tool for elucidating the downstream effects of BSEP dysfunction and identifying potential alternative bile acid transport systems. One limitation of this model is the development of mild, non-progressive cholestasis, likely attributable to the inherently more hydrophilic nature of endogenous bile acids in mice compared to humans (Gooijert et al. 2015). This can be addressed by supplementing *BSEPKO* mice with additional cholic acids (Wang et al. 2003). Additionally, *BSEPKO* mice can serve as a model for studying various genetic forms of cholestasis characterized by *BSEP* mutations, such as PFIC2 and benign recurrent intrahepatic cholestasis 2 (Gooijert et al. 2015).

One of the earliest genetically modified models designed to study hepatobiliary diseases associated with PSC was introduced in 1994, known as the *MDR2KO* mice. The *Mdr2* gene, analogous to the human *MDR3 (ABCB4)* gene, encodes a transporter responsible for secreting phospholipids into bile across the bile canalicular membrane (Mauad et al. 1994). Consequently, *MDR2* ablation leads to the absence of phospholipids in bile, hindering the formation of biliary micelles and resulting in liver injury, particularly manifesting as cholelithiasis and sclerosing cholangitis. Although initially utilized to explore the role of PFIC3, the *MDR2KO* mouse model also exhibits histological lesions resembling human PSC, including rapid progression into hepatic fibrosis. However, a notable limitation of this model is the absence of concurrent inflammatory bowel disease (IBD) and the spontaneous development of hepatocellular carcinoma *in vivo* (Tam et al. 2018; Ikenaga et al. 2015).

Another model was established based on the observed similarities between PSC and liver phenotype in cystic fibrosis disease. Both conditions involve cholestasis, chronic inflammation, and portal tract injury. Given that mutations in the cystic *CFTR* gene are implicated in cholestatic liver injury, CFTR-knockout (*CFTRKO*) mice with an exon 10 deletion were hypothesized to develop a comparable liver disease. While these mice did exhibit progressive liver disease, characterized by focal cholangitis, inspissated bile, and bile duct proliferation, conflicting reports exist regarding their suitability as a PSC model, with some

studies suggesting that *CFTRKO* mice primarily manifest an intestinal phenotype resembling distal intestinal obstruction syndrome rather than the typical IBD phenotype seen in PSC. Additionally, erythropoietic protoporphyria, an inherited disorder characterized by protoporphyrin accumulation due to reduced ferrochelatase activity, can lead to severe liver diseases requiring transplantation (Martin et al. 2012; Pall et al. 2006; Blanco et al. 2004; Durie et al. 2004).

Mice with a homozygous mutation in the ferrochelatase gene (*fch/fch*) demonstrate an extreme cholestatic phenotype marked by increased serum liver injury markers (liver enzymes such as AST, ALT, and ALP), elevated bile salt levels, and conjugated hyperbilirubinemia, although bile formation remains unaffected (Bloomer et al. 1998). However, further research is warranted to comprehensively characterize the longitudinal changes and underlying pathogenetic mechanisms in *fch/fch* mice (Libbrecht et al. 2003; Meerman et al. 1999)

1.5.1.3 Chemical-induced cholestasis

Chemical-induced cholestasis is a major health concern, often resulting from exposure to various substances such as medications, pesticides, food additives, cosmetic ingredients, and industrial chemicals. Different types of cholestatic liver injuries have been identified depending on the causative agent, ranging from (hepato)canalicular, hepatocellular to ductular cholestasis (Lewis and Zimmerman 1999).

The α-naphthylisothiocyanate (ANIT) is a chemical compound commonly used in the preparation of cationic aromatic urethane. It is well-known for its ability to induce cholestasis in rats and mice by specifically targeting BECs, leading to hepatocellular necrosis. Chronic exposure to ANIT via the diet mimics the experimental setting of chronic cholangitis, bile duct hyperplasia, and peribiliary fibrosis. Mechanisms underlying peribiliary fibrosis in chronic ANIT models show similarities with other chronic cholestasis models, such as long-term BDL and *MDR2KO* (Han et al. 2024; Wu et al. 2022; Wu et al. 2020; Wang et al. 2019; Gayathri and Padmanaban 1974).

Additionally, lithocholic acid, an endogenous bile acid, can induce cholestasis when present in abnormally high concentrations. This effect has been extensively studied in rodents to understand its potential role in the pathogenesis of cholestasis. Cholestasis induced by lithocholic acid is attributed to partial obstruction of the bile ducts due to crystal formation, along with bile infarcts, destructive cholangitis, and periductal fibrosis. The lithocholic acid rodent model is considered a valid short-term model for investigating early changes in PSC

due to the rapid changes induced by lithocholic acid administration (Fickert, Fuchsbichler, et al. 2006; Trauner et al. 2008).

Another compound, 3,5-diethoxycarbonyl-1,4-dihydrocollidine (DDC), is also known to induce cholestasis. DDC is a porphyrinogenic agent and a strong initiator of δ-aminolevulinate synthetase (Vilas-Boas et al. 2019; Fickert et al. 2014). Its administration leads to increased secretion of hepatotoxic protoporphyrins, along with the formation of protoporphyrin plugs that obstruct the small bile ducts, initiating cholestasis. DDC-induced cholestasis is characterized by sclerosing cholangitis, pronounced biliary fibrosis, and ductular proliferation. DDC feeding in rodents serves as a model for investigating intrahepatic cholestasis (Gayathri and Padmanaban 1974; Fickert et al. 2007; Fickert 2014).

Bile acid-induced cholestasis in murine models is a widely utilized approach to investigate the pathophysiology of cholestatic liver disease and test potential therapeutic interventions. In these models, cholic acid (CA), one of the primary bile acids, is administered through diet supplementation, resulting in the accumulation of bile acids in hepatocytes and cholangiocytes. This leads to liver damage characterized by jaundice, weight loss, elevated serum bile acids, and increased liver enzymes (Wang and Boyer 2004). The excess of bile acids disrupts hepatocyte function, causing oxidative stress, mitochondrial damage, and the release of inflammatory cytokines, which drive liver inflammation and fibrosis (Cai et al. 2017; Cai and Boyer 2021). Cholic acid-induced cholestasis models are particularly valuable because they mimic BSEP deficiencies observed in human diseases like PFIC (Wang et al. 2003). Additionally, these models enable the study of bile acid homeostasis, hepatic bile flow, and the role of alternative bile acid transport systems in cholestasis (Wang et al. 2003). Overall, cholic acid-induced cholestasis provides a robust platform for investigating the mechanisms of bile acid toxicity and testing novel therapeutic strategies for cholestatic liver diseases.

1.6 Intermediate filaments in liver disease

The disruption of intermediate filaments due to the accumulation of hydrophobic bile acids in cholestatic conditions can lead to dilated bile canaliculi and compromised tight junctions, exacerbating cholestasis (Fickert et al. 2009; Fickert et al. 2014). In a study of PBC patients, six disease-associated keratin variants were identified, with four mutations being novel. This suggests that K8/K18/K19 variants could act as genetic modifiers in PBC, influencing disease progression (Zhong et al. 2009).

Hepatocytic keratins are essential for maintaining the structural integrity of the bile canaliculus, although their exact role in bile secretion remains unclear. During obstructive cholestasis, the pericanalicular sheath thickens due to the accumulation of intermediate filaments driven by increased bile canalicular pressure (Ku et al. 2010; Omary et al. 2009). Mutations in keratin genes, which cause unstable or abberantly organized keratin ifilament network, increase susceptibility to a range of liver diseases, including cholangiopathies. Mouse models lacking K8 or K18, or those mimicking human keratin mutations, exhibit increased hepatocyte fragility, necrosis, and hemorrhage, often leading to lethal outcomes (Toivola et al. 2015; Zhong et al. 2009).

Additionally, Chen et al. (2015) explored the role of K19 in biliary and hepatic progenitor cells, particularly during the ductular reaction, which is a regenerative response to chronic liver injury (Chen et al. 2015). In K19-knockout mice, subjected to models of liver injury such as CA feeding and BDL altered keratin intermediate filament networks were observed in BECs. This deficiency attenuates the ductular reaction and reduced bile duct proliferation, although K19 absence did not affect the severity of liver injury or fibrosis induced by CA or BDL (Chen et al. 2015). These findings highlight the crucial role of K19 in liver regeneration during cholestatic injury (Toivola et al. 2015; Toivola et al. 2024; Chen et al. 2015).

The evolving understanding of the keratin-desmosome scaffold has also shed light on the important role of keratin filaments in simple epithelia. K8/K18 keratins are particularly important in the liver, where they contribute to maintaining cellular integrity under mechanical stress (Toivola et al. 2024). In both human liver disease and transgenic mouse models, keratin mutations not only predispose liver to damage but also influence disease severity, particularly in conditions such as cholestasis and PBC (Toivola et al. 2024).

1.7 **Plectin mutation in liver disease**

As discussed earlier, plectin gene mutations have recently been linked to the pathogenesis of cholestatic liver disease, particularly in infants with severe, early-onset forms. Initially presenting with symptoms resembling PFIC, these cases were later confirmed through next-generation sequencing to involve plectin gene mutations (Thebaut et al. 2024; Wu et al. 2019; Kor-Anantakul et al. 2024). Diagnosed within the first few months of life, these findings highlight the critical role of plectin in liver function and expand the known clinical spectrum of plectinopathies.

Plectin mutations, particularly in the rod domain essential for plectin dimerization and intermediate filament interaction, were observed in all cases, broadening the scope of plectinopathies to include liver disease. Two cases also had mutations in the SH3 domain (Wu et al. 2019; Thebaut et al. 2024), while Kor-Anantakul et al. (2024) reported a mutation in the N-terminal actin-binding domain specific to isoform 1f (Kor-Anantakul et al. 2024). These findings suggest that plectin dysfunction in bile transport and hepatocyte structure contributes to cholestasis.

Histopathology varied across cases, indicating a heterogenity of plectin-related liver disease. Kor-Anantakul et al. (2024) described that, there was abnormal localization of bile transporters BSEP and MRP2, mislocalization of plectin, and dilated bile canaliculi (Kor-Anantakul et al. 2024). In contrast, Thebaut et al. (2024) showed less severe canalicular abnormalities but notable ductular proliferation, suggesting variability in how specific plectin mutations affect liver damage (Thebaut et al. 2024). The Kor-Anantakul et al. (2024) highlighted the disruption of the actin-binding domain, with scattered plectin signals and mislocalized bile transporters (Kor-Anantakul et al. 2024).

These findings suggest that plectin gene mutations contribute to cholestasis through impaired cytoskeletal integrity and bile transporter function. The association of plectin mutations with a PFIC-like phenotype expands our understanding of cholestatic liver disease, emphasizing the need for further research into plectin's role in bile secretion and potential therapeutic interventions targeting the cytoskeleton or bile transporter localization.

2 Aims

Plectin, a highly versatile cytolinker protein, plays a pivotal role in regulating the cytoarchitecture of keratin filaments and the cellular stress response. Moreover, plectin plays a role in maintaining epithelial cytoarchitecture by anchoring keratin filaments to cell adhesion structures, including desmosomes and hemidesmosomes, as well as to the nucleus. The ablation of plectin results in ablation of the circumferential keratin rim, the bundling of keratin filaments, defects in cell cohesion, and the general destabilisation of aberrant keratin filament networks in epithelial cells.

The objective of this thesis is to investigate the role of plectin in the liver under basal conditions and in experimental cholestasis. We hypothesised that cytoskeletal stability and the integrity of the liver epithelium, both biliary and parenchymal, is critical to withstand a cholestatic insult. Moreover, properly integrated cytoskeletal networks are required for the reorganization of cellular cytoarchitecture and cell adhesion of the epithelium during adaptation response to cholestasis. In order to test this hypothesis, we characterized liver-specific PLEKO ($Ple^{\Delta alb}$) mice and analyzed plectin's role in three cholestatic liver injury models: bile duct ligation (BDL), 3,5-diethoxycarbonyl-1,4-dihydrocollidine (DDC) feeding, and cholic acid (CA) feeding.

The aims of this thesis are as follows:

Aim I. The effect of liver- specific plectin deficiency on liver organization.

- To characterize plectin-deficient mutant mouse ($Ple^{\Delta alb}$).
- To describe the plectin's role in the maintenance of the structural integrity of the hepatocellular cytoarchitecture.
- To define the effects of plectin deficiency on biliary architecture.

Aim II. The role of plectin in maintaining liver tissue integrity by enabling an adaptive cellular response to cholestatic stress.

- To characterize biliary and hepatocellular damage in $Ple^{fl/fl}$ (as defined above) and $Ple^{\Delta alb}$ mice using three cholestatic liver injury models: bile duct ligation (BDL), 3,5-diethoxycarbonyl-1,4-dihydrocollidine (DDC) feeding, and cholic acid (CA) feeding.
- To ddefine cholestasis-induced adaptive remodeling of interlobular bile ducts and hepatic bile canaliculi in plectin deficient environment.

3 Materials and Methods

3.1 Animal experiments

Liver-specific deletion of the plectin was achieved by breeding plectin$^{flox/flox}$ mice (Ackerl et al. 2007) with an *Alb-Cre* transgenic mice (MGI 2176228; The Jackson Laboratory) to generate *Plectin$^{lox/lox}$/Alb-Cre* mice. All experiments were performed using age-matched littermate male mice. All animal studies were performed in accordance with European directive 86/609/EEC and were approved by the Czech Central Commission for Animal Welfare.

3.1.1 Mouse injury models

Animals were housed under standard pathogen-free conditions, had free access to regular chow and drinking water, and were kept under a 12-hour-dark/12-hour-light cycle.

Obstructive cholestasis was induced by ligation of common bile duct (BDL). 10-week-old male mice were anesthetized with ketamine (80 mg/kg) and xylazine (10 mg/kg) and subjected to the surgery. Common bile duct was exposed through a midline abdominal incision, double-ligated using 4-0 silk, and sectioned between the ligatures. Sham-operated control mice had their common bile duct exposed and manipulated but not ligated. After 1, 5 or 14 days, mice were sacrificed by cervical dislocation and blood and liver samples were collected.

To study the effects of DDC-diet, mice were fed with a diet supplemented with 0.1% DDC (Sniff, Soest) for 14 days. Control animals were fed with regular chow for the same time period. For recovery studies mice were fed for 14 days with DDC and then let recover for 3 days of standard chow. Additionally, to investigate the consequence of disrupted bile acid homeostasis mice were fed with diet supplemented with 0.5% cholic acid (Sniff, Soest, Germany) for 14 days.

Serum levels of aspartate transaminase (AST), alanine transaminase (ALT) and alkaline phosphatase (ALP), total/conjugated bilirubin were measured using commercial kits (Roche Diagnostics). Total bile acids (tBA), cholesterol and triglycerides were measured. Liver were dissected, the respective liver lobes isolated and either fixed in 4% buffered formalin (pH 7.4) and embedded in paraffin or directly embedded for cryo-sectioning (OCT Tissue-Tek; Sakura Finetek).

3.2 Histology, immunohistochemistry and immunofluorescence

Formalin-fixed liver sections (4 µm) were stained with haematoxylin and eosin (H&E), Sirius Red, Masson's trichrome (Sigma Aldrich) and periodic acid of Schiff (PAS) kit (Sigma-Aldrich). Prior staining the liver slides were deparaffined with xylen and ethanols and rehydrated in PBS or water.

3.2.1 Hematoxylin and Eosin (H&E)

Deparaffinized and rehydrated slides of liver section were immersed with Mayer's hematoxylin for 10 minutes and differentatied under tap water for 12 minutes. After rinsing in destiled water (dH_2O), the slides were placed in a 96% ethanol for 2 minutes, followed by staining with Eosin Y for 0.5 minute, and then washed in 96% ethanol for 2 minutes followed by 100% ethanol for 5 minutes. Finally, the slides were placed in xylene for 1 minute and cover with coverslips using DPX hardening mounting media (Sigma Aldrich).

3.2.2 Sirius Red (SR) staining

Deparaffinized and rehydrated slides of liver section were immersed with 0.1% (wt/vol) SR in picric acid for 1.5 hours, then washed with dH_2O. Subsequently, the slides were rinsed in a 96% ethanol for 2 minutes, followed by 100% ethanol for 5 minutes. Finally, the slides were placed in xylene for 1 minute and cover with coverslips using DPX hardening mounting media (Sigma Aldrich, St. Louis).

3.2.3 Masson's trichrome

Deparaffinized and rehydrated slides of liver section were placed in preheated Bouin's Solution (75 % (vol/vol) picric acid, 10% (vol/vol) formaldehyde, 5% (vol/vol) glacial acetic acid) at 37°C for 45 minutes. Then the slides were cooled in tap water for 10 minutes. The slides were counterstain Mayer's hematoxylin for 10 minutes, differentiated in running tap water for 12 minutes and rinsed in dH_2O. Afterwards the liver sections were stained in Biebrich Scarlet-Acid Fucshin solution for 5 minutes, rinsed in dH_2O and differentiate in phosphomolybdic-phosphotungstic acid solution for 5 minutes. The slides were placed in aniline blue solution for 5 minutes, rinsed briefly in distilled water and differentiated in 1% acetic acid solution for 2 minutes, then washed in 96% ethanol for 2 minutes followed by 100% ethanol for 5 minutes. Finally, the slides were placed in xylene for 1 minute and cover with coverslips using DPX hardening mounting media (Sigma Aldrich).

3.2.4 Periodic acid of Schiff (PAS)

The PAS staining was performed according the manufacturer's instructions (Sigma Aldrich). Briefly, deparaffinized and rehydrated slides of liver section were incubated in Periodic Acid Solution for 5 minutes, washed in dH_2O 3x5 minutes, and incubated in Schiff's Reagent for 15 minutes. Subsequently, they were washed with running tap water for 5 minutes. Liver sections were then counterstained in Hematoxylin Solution, Gill No. 3 (Sigma Aldrich), for 90 seconds, rinsed under running tap water, and washed in 96% ethanol for 2 minutes, followed by 100% ethanol for 5 minutes. Finally, the slides were placed in xylene for 1 minute and cover with coverslips using DPX hardening mounting media (Sigma Aldrich).

3.2.5 Immunohistochemistry

For immunohistochemistry deparaffinized and rehydrated slides of liver section were subjected to heat induced antigen retrieval in Tris-EDTA (pH 9) or citrate (pH 6) buffer for 15 minutes and further permeabilized with 0.1 M glycine, 0.1% (vol/vol) Triton X-100 for 15 minutes. cryo-sections (8 µm) were fixed with ice-cold acetone for 10 minutes or 4% (wt/vol) paraformaldehyde for 20 minutes at room temperature. Blocking of unspecific antigen interactions was performed with 5% (wt/vol) BSA in PBS + 0.1% Tween20 (PBS-T) for 60 minutes at room temperature. Afterwards, sections were incubated with primary antibodies at 4°C overnight than extensively washed 3x15 minutes in PBS-T, followed by incubation with secondary antibodies at room temperature for 2 hours. The F-actin was labelled on 30- µm thick cryo-sections fixed with 4% (wt/vol) paraformaldehyde for 20 minutes using fluorescently conjugated phalloidins (diluted 1:400; AF405, AF488, Thermo Fisher Scientific, Waltham, USA) incubated for 2 hours. The following primary antibodies were used: mouse monoclonal antibodies (mAbs) to K18 (diluted 1:40; Progen), mouse mAbs to K7 (diluted 1:100; Abcam), mouse mAbs to E-Cadherin (diluted 1:250; BD Biosciences), mouse mAbs to desmoplakin (undiluted; Progen), mouse mAbs to desmoglein (diluted 1:5; Progen), rat mAbs to A6 (diluted 1:100; kindly provided by V. Factor), rat mAbs to K8 (diluted 1:120; Troma I, Developmental Studies Hybridoma Bank, University of Iowa), rat mAbs to K19 (diluted 1:250; Troma III, Developmental Studies Hybridoma Bank, University of Iowa), rabbit mAbs, rabbit mAbs to ZO-1 (diluted 1:250; Life Technologies), , rabbit mAbs to ABCB11/Bsep (diluted 1:100; Thermo Fisher Scientificrabbit mAbs to Ki-67 (diluted 1:50; Genetex); affinity-purified rabbit anti-pan-K (diluted 1:250; DAKO) and guine pig anti-plectin (diluted 1:250; Progen) antibodies. As secondary antibodies we used donkey anti-mouse IgG Alexa Fluor (AF) 488,

goat anti-mouse horseradish peroxidase (HRP)-conjugated, donkey anti-rabbit AF488, AF594 and AF647, goat anti-rabbit HRP-conjugated, donkey anti-rat AF488, goat anti-rat HRP-conjugated, donkey anti-guinea pig AF488 and AF594 (all from Jackson ImmunoResearch), and goat anti-guinea pig HRP-conjugated (Sigma-Aldrich). Nuclei were counterstained with Hoechst 33258 (1:1000, Sigma-Aldrich) for 15 minutes than washed 3x5 minutes in PBS-T and 5 minutes in dH_2O. Finally, the liver sections were covered with cover glass using ProLong™ Gold Antifade Mountant (Thermo Fisher Scientific). Antibodies in IHC were visualized by diaminobenzidine (DAB) using the DAB Substrate (peroxidase buffer: DAB metal concentrate; 10:1) (Roche Diagnostics, Prague, Czech Republic) for 7.5 minutes followed by wash 3x5 minutes in dH_2O and counterstained with Mayer's hematoxylin (Sigma-Aldrich) already described in H&E. Finally, the slides were placed in xylene for 1 min and cover with cover slides using DPX hardening mounting media (Sigma Aldrich).

3.2.6 3D fluorescent imaging of mouse liver tissues

Whole-liver samples from adult mice were prepared as follows. Mice were anesthetized the by intramuscular injection of tiletamine (60 mg/kg), zolazepam (60 mg/kg) and xylazine (4.5 mg/kg). Than 10 µL of heparin (5000 U/mL, Zentiva) was injected into vena cava using a 30G insulin syringe. The liver was cannulated and perfused via the vena cava sequentially with 5 mm of PBS followed by 10 ml of 2% (wt/vol) paraformaldehyde in PBS, and 10 ml of 4% (wt/vol) paraformaldehyde in PBS. Upon harvest, the liver was placed into a 50 ml tube containing 4% (wt/vol) paraformaldehyde in PBS, and incubated for 12 hours. After fixation, the liver was incubated in 10% (wt/vol) sucrose in PBS for 8 hours, and in 20% (wtl/vol) sucrose in PBS overnight. Finally, the liver was embedded in Tissue-Tek O.C.T. compound (Sakura Finetek, Japan) and snap frozen. The frozen liver samples were cut into 80-µm-thick sections using the cryostat-microtome (Leica Microsystems). The sections were subjected to heat induced antigen retrieval in Tris-EDTA buffer (pH 9) for 15 minutes in water-bath on hot plate (CB302, Stuart) and further blocked and permeabilized with 3% (vol/vol) FBS, 0.02% (wt/vol) sodium azide, and 0.2% (vol/vol) Triton X-100 in PBS for 90 minutes at room temperature. Afterwards, sections were incubated with primary antibodies K19 (Troma III, Developmental Studies Hybridoma Bank, USA, diluted 1:100 in blocking solution) and DPP4 (AF954, RD diluted in block 1:100) at 4°C for 48 hours followed by extensive washing 3x45 minutes in PBS-T. After washing the sections were incubated with secondary antibodies at room temperature for 48 hours followed by extensive washing 3x45 minutes in PBS-T. After staining and washing, samples were treated with the tissue-clearing reagent SeeDB (Ke et al.,

2013) as follows. Stained samples were serially incubated in 2–3 ml of 20%, 40% and 60% (wt/vol) fructose, each for 4 hours with gentle shaking at room temperature. Samples were then incubated in 80% (wt/vol) fructose for 16 hours, 100% (wt/vol) fructose for 12 hours and finally in SeeDB (80.2% wt/wt fructose) for 72 hours with gentle shaking at room temperature. 3D immunofluorescence stacks of liver sections were obtained on a Leica TCS SP8 confocal microscope (Leica Microsystems, with HC PL APO 63x/1.40 NA, oil-immersion objective lens).

3.2.7 Image acquisition

Immunofluorescence images were acquired using DeltaVision OMX™ super-resolution microscope (GE Healthcare Life Sciences, with PlanApo N 60x/1.42 NA, oil-immersion objective lens), Leica STELLARIS 8 FALCON with the LIGHTNING adaptive deconvolution (Leica Microsystems, with HC PL AP with HC PL APO 63x/1.40 OIL CS2), Leica TCS SP8 confocal microscope (Leica Microsystems, with HC PL APO 63x/1.40 NA, oil-immersion objective lens) and LSM 880 Airyscan super-resolution microscope (Zeiss, equipped with Alpha Plan-Apochromat 100X, NA 1.46, oil immersion, WD 0.11 mm). Immunohistochemistry images were acquired with inverted fluorescence microscope DM6000 (Leica Microsystems, with HC PL Apo 10x/0.40 NA, PH1 HC PLAN Apo 20x/0.70 NA, and PH2 HCX PL Apo 40x/0.75 NA, objective lenses). All fluorescence images were acquired as Z-stacks and deconvolved with Huygens Essential 4.0.0 software (Huygens; Scientific Volume Imaging, Hilversum) using blind deconvolution. Post-acquisition processing was performed with open-source Fiji image processing package and Imaris software (Bitplane).

3.3 Electron microscopy

Whole liver perfusion was performed as follows. Mice were anesthetized the by intramuscular injection of tiletamine (60 mg/kg), zolazepam (60 mg/kg) and xylazine (4.5 mg/kg). Than 10 µL of heparin (5000 U/mL) was injected into IVC using a 30G insulin syringe. The liver was cannulated and perfused via the IVC by peristaltic pump with cold 1.5% (vol/vol) glutaraldehyde in PBS for 20 minutes (flow rate 1.5 ml/minute). For transmission electron microscopy (TEM) were liver pieces immersed in fixative solution (1% (vol/vol) glutaraldehyde and 4% (wt/vol) paraformaldehyde in PBS) for 48 hours and post-fixed in a mixture of 1% osmium tetroxide and 1% potassium ferricyanide in PBS for 12 hours at 4 °C. Fixed and washed samples were dehydrated via ethanol solutions and embedded into resin (EPON 812 resin). Ultrathin sections (60 nm) were contrasted using uranyl acetate and lead

citrate and examined in a FEI/Philips CM100 electron microscope (FEI). For scanning electron microscopy (SEM) 3-mm-thick blocks of liver were dehydrated in an ethanol series followed by 100% acetone and after critical point drying sputter coated with 3 nm of platinum. Livers were imaged with Nova Nanosem 450 scanning electron microscope (FEI).

3.3.1 Histological and morphometric analysis

Blinded histopathology evaluation was performed by a trained pathologist (O. Fabian) on liver sections stained with H&E, Sirius Red, Masson's trichrome, and PAS.

3.3.1.1 Quantification of necrotic area

Liver sections stained with H&E and scanned with microscope DM6000 (Leica Microsystems, with HC PLAN Apo 20x/0.70 NA objective lense). Necrotic areas in liver parenchyma were measured and quantified using open-source Fiji software.

3.3.1.2 Quantification of SR-positive area

Liver sections stained with SR and scanned with microscope DM6000 (Leica Microsystems, with HC PLAN Apo 20x/0.70 NA objective lense). SR-positive collagen deposits were measured and quantified using open-source Fiji software

3.3.1.3 Quantification of K19-positive area

Liver sections immunolabeled with K19 antibody and scanned with microscope DM6000 (Leica Microsystems, with HC PLAN Apo 20x/0.70 NA objective lense). K19 positive areas in liver tissue were measured and quantified using open-source Fiji software. 10 portal vein fields per animal were scoored. 3 animals per genototype were analysed.

3.3.1.4 Quantification of Ki67-positive area

Liver sections immunolabeled with Ki67 antibody and scanned with microscope DM6000 (Leica Microsystems, with HC PLAN Apo 20x/0.70 NA objective lense). Ki67-positive areas in liver tissue were measured and quantified using open-source Fiji software. 10 portal vein fields per animal were scoored. 3 animals per genototype were analysed.

3.3.1.5 Quantification of A6-positive area

Cryo liver sections immunolabeled with A6 antibody and scanned with microscope DM6000 (Leica Microsystems, with HC PLAN Apo 20x/0.70 NA objective lense). A6-positive areas in liver tissue were measured and quantified using open-source Fiji software. 10 portal vein fields per animal were scoored. 3 animals per genototype were analysed.

3.3.1.6 Quantification of keratin aggregates

Liver sections immunolabeled with K8 antibody and scanned with microscope DM6000 (Leica Microsystems, with HC PLAN Apo 20x/0.70 NA objective lense). K8-positive areas in liver tissue were measured and quantified using open-source Fiji software. 3 animals per genotype were analysed.

3.3.1.7 Quantification of biliary tree morphology

The morphology of bile canaliculi (length, width) and ducts (perimeter, luminal area, largest and the smallest orthogonal diameter) was evaluated either from maximal projections of image stacks of the liver sections immunolabelled for ZO-1 or CK19 or SEM micrographs using open-source Fiji software. The circularity of bile duct was calculated as 4π x area/perimeter^2; thus, perfectly round bile ducts have a shape factor of 1, whereas more elongated or stellate bile ducts exhibit lower values. The axial ratio of duct is defined as the ratio of the largest and the smallest orthogonal diameter. The canalicular tortuosity was calculated from 10 μm segments between canalicular branches as the ratio of the straight-line distance between end-points of this line and the canalicular length. The number of canalicular branching points was determined from 3-dimensional reconstructions generated from 10-μm-thick liver sections immunolabeled for ZO-1 using Imaris software (Bitplane).

3D stacks images were deconvolved with Huygens Essential 4.0.0 software (Huygens; Scientific Volume Imaging) using blind deconvolution. These Z-stacks were used for surface reconstructions and morphometric analyses in 3D. Surface reconstructions of the 3D stacks were generated using Imaris software (Bitplane). Measurement of duct diameter, eccentricity, tortuosity, volume, duct branching, biliary tree complexity, luminal surface area, luminal surface corrugation, was performed using custom software developed by Vartak et al. (Vartak et al. 2016).

3.3.1.8 The apicobasal distribution of K18 and K19

The apicobasal distribution of K18 and K19 filaments in cholangiocytes was evaluated from maximal projections of image stacks of the liver sections immunolabeled with respective antibodies. Apical and basal fluorescence signal intensities were determined using a 1-pixel freehand line in Fiji software. The relative intensities were calculated as the area below the curve of signal intensity using MATLAB software (MathWork) and normalized to total signal intensity determined per individual cholangiocyte.

3.4 Bile flow and bile composition analysis

Bile flow was measured based on protocol of Fickert et al. (2006) (Fickert, Wagner, et al. 2006). Mice were fasted for 4 hours prior surgery with free access to water. Mice were anesthetized the by intramuscular injection of tiletamine (60 mg/kg), zolazepam (60 mg/kg) and xylazine (4.5 mg/kg). Mice were placed on warming pad. The CBD was cannulated via a sphincter of Oddi with polyethylene tubing. After a 5 minutes equilibration period bile was collected for 1 hour in pre-weighted tubes every 15 minutes. After collection the bile was snap frozen on dry ice a stored at -80°C. Bile flow was determined gravimetrically (assuming a density of 1.0 g/ml) and normalized to mouse body weight.

Biliary phospholipid and cholesterol concentrations were determined using commercial kits: Bile acid analysis was performed using liquid chromatography-tandem mass spectrometry (LS-MS/MS) method. Chromatographic separation was carried out using UHPLC system Infinity 1290 coupled to mass spectrometer 6550 iFunnel Q-TOF with Dual Agilent Jet Stream ESI ion source (Agilent Technologies). The samples were separated on Poroshell EC-C18 column (Agilent Technologies) with gradient elution by 2 mM ammonium formiate and acetonitrile. The MS/MS detection was operated in negative mode.

3.5 Quantitative reverse-transcriptase polymerase chain reaction

Total RNA was isolated from frozen liver samples using TRIzol® RNA isolation reagent (Thermo Fisher Scientific) according to the manufacturer's instructions. Concentration of RNA was determined using a Nanodrop ND-1000 (Thermo Fisher Scientific). Unique primers were designed for approximately 100 bp segments of targeted gene transcripts using QuantPrime online software. Following sequences were used (*Abcb4* – TAAAGCGATGCTAAGGCAGGAC; *Bsep* – CAAACGGAACAAGCTGTGGGTTG; *Slc10a1* – ATGTACCCTACGTCCTCAAGGC). Complementary DNA was prepared from 500 ng of RNA sample using Superscript II Reverse transcriptase (Life Technologies, Carlsbad) and random oligo (dT)18 primers. Quantitative RT-PCR was performed with SYBR Green JumpStart Taq ReadyMix (Sigma-Aldrich). RNA expression levels were calculated using a comparative threshold cycle method (delta-delta Cq) using GAPDH as internal control.

3.6 Protein extraction and immunoblot analysis

Snap-frozen liver samples were homogenized in RIPA buffer (150 mM NaCl, 1 mM Na_2EDTA, 1 mM EGTA, 1% NP-40 1% sodium deoxycholate, 2.5 mM sodium pyrophosphate,

1 mM glycerophosphate, 1 mM Na_3VO_4, and 20 mM Tris-HCl, pH 7.5) supplemented with Halt protease and phosphatase inhibitor Cocktail (Thermo Fisher Scientific) using a TissueLyser II (Qiagen). Protein concentrations were determined using the BCA Protein Assay Kit (Thermo Fisher Scientific). Proteins were separated by SDS-10% PAGE and transferred to nitrocellulose membranes. For immunoblotting, the following primary antibodies were used: rabbit mAbs to actin, GAPDH (both Sigma-Aldrich), phospho-p38-MAPK; anti-p38-MAPK (all Cell Signaling), and goat anti-collagen 1 (Santa Cruz Biotechnology) antibodies. Secondary antibodies were HRP-conjugated goat anti-mouse IgG, goat anti-rabbit IgG, goat anti-rat IgG (all from Jackson ImmunoResearch, USA), and goat anti-guinea pig IgG (Sigma-Aldrich). Signals were detected by ECL plus Western Blotting Detection System (GE Healthcare Life Sciences) and recorded with a Luminescent Image Analyzer LAS-3000 (Fujifilm Life Science). Densitometry of blots was analysed using QuantiScan version 1.5 software (Biosoft).

3.7 Isolation and cultivation of primary hepatocytes

3.7.1 Solutions for primary hepatocytes isolation

Stock Solution A (10x): NaCl (80 g/l); KCl (4g/l); $MgSO_4$. $7H_2O$ (1.97 g/l); Na_2HPO_4. $2\ H_2O$ (0.598 g/l); KH_2PO_4 (0.6g/l) dissolved in water.

Stock Solution B (10x): NaCl (69 g/l); KCl (3.6 g/l); KH_2PO_4 (1.3 g/l); $MgSO_4$. $7H_2O$ (2.94 g/l); $CaCl_2$ (2.772 g/l) dissolved in water.

Solution C: 5 ml of stock solution A (10x); $NaHCO_3$ (0.1094 g/50 ml); EGTA (0.0095 g/50 ml); pH adjusted to 7.3; water to 50 ml.

Solution D: 3 ml of stock solution A (10x); $NaHCO_3$ (0.065 g/30 ml); $CaCl_2$ (0.0125 g/30 ml); water to 30 ml; Collagenase I (5mg/30 ml); pH adjusted to 7.3

Solution E: 5 ml of solution B (10x); $NaHCO_3$ (0.1 g/50 ml); glucose (0.45 g/50 ml); pH adjusted to 7.3; water to 50 ml; Albumin V (0.65g/50 ml).

Primary hepatocytes were isolated from 8 – 12-week-old animals by a collagenase perfusion as follows. Mice were anesthetized the by intramuscular injection of tiletamine (60 mg/kg), zolazepam (60 mg/kg) and xylazine (4.5 mg/kg). Than 10 µL of heparin (5000 U/mL) was injected into IVC using a 30G insulin syringe. The liver was cannulated and perfused via the IVC by peristaltic pump with the pre-warmed (37°C) solution C for 2 minutes (at flow rate of 2.5 ml/minutes 5 ml of perfusion solution). Change to the solution D and continue the

perfusion for further 10 minutes (25 ml of solution D). Than the liver was placed into 20 ml of solution E. Followed by centrifugation at 50xg for 5 min at 4°C. Supernatant was aspirated. To remove the dead cells and increase the viability percentage of the cells, the pellet was resuspended in 20 ml of 40% (vol/vol) Percol. (Sigma-Aldrich) in DMEM and centrifugated at 100xg for 7 minutes. The. supernatant containing the dead cells was aspirated and the pellet was resuspended in 20 ml of solution E and centrifuged at 50xg for 5 minutes at 4°C. Finally, the supernatant was aspirated and the pellet was resuspended in 10 ml of solution E. The primary hepatocytes yield and viability was estimated using Tryptan Blue. And the cell number was adjusted to 6x 10^5 viable cells/ ml in hepatocytes culture medium (15 µl of glucagon (1 mg/ml), 15 µl of hydrocortisone (50 mg/ml) and 40 µl of insulin (10 mg/ml) in 50 ml of complete medium (DMEM, high glucose, 10% FBS, 1% Penicillin-Streptomycin).

For OA treatment cells were seeded on collagen-coated dishes or cover slips and cultured under standard conditions for 18 hours.

To study canalicular formation and morphology *in vitro*, isolated primary hepatocytes were grown in 3D collagen sandwich culture as follows. Day before primary hepatocytes isolation the 1st layer of collagen I Sandwich. Was prepared. Firstly, collagen I solution (354249, Corning) was neutralized according manufacturer protocol (100 µl of neutralized collagen I (1.5 mg/ml) per experimental sample (one well of 6-well plate). To prepare 1 ml of neutralized collagen (1.5 mg/ml) 100 µl of 10x DMEM, 11.5 µl of 1M NaOH and 488.5 µl of dH_2O was added into 500 µl of collagen. Plate was incubated over-night in an incubator with 5% CO^2 at 37°C. At the day of primary hepatocytes isolation 1 ml of pre-warmed (37°C) PBS was added on 1st layer of collagen. 1 ml (6x10^5 cells/ml) of viable primary hepatocytes were seeded into pre-coated well of 6-well plate. Plate was kept with 5% CO_2 at 37°C for 3 hours. After cells were attached, the 2nd layer of neutralized collagen I (100 µl/ well of 6-well plate) was added and the plate was. incubated (5% CO2 at 37°C) for 45 minutes. Finally, 2 ml of hepatocytes culture medium was added. Cells were cultured for 4 days. The hepatocytes culture medium was changed every second day.

3.7.2 Okadaic acid treatment

Primary hepatocytes were cultured overnight on collagen coated cover slips and then exposed to 30 nM okadaic acid (Sigma-Aldrich) in serum free DMEM for 60 minutes. After incubation with 30 nM okadaic acid, cells were fixed with 4% paraformaldehyde, immunolabeled with antibodies recognizing pan-keratin and mounted mounted with antifadde

mounting media for microscopy. After 24 hours, the samples were visualized with inverted fluorescence microscope Delta Vision Core (Olympus). Analysis of the keratin cytoarchitecture was performed and the presence of collapsed keratin filaments network was quantified in more than 600 cells per genotype and treatment.

3.7.3 Deoxycholic acid treatment

Primary hepatocytes were cultured for 4 day in 3D collagen sandwich and then exposed to 100 µM; 200 µM deoxycholic acid (Sigma-Aldrich) diluted in DMSO or DMSO only in controls, in hepatocytes culture medium for 16 hours. After incubation were cells washed with PBS and fixed with 4% paraformaldehyde for 30 minutes. For analysis of bile canalicular width cells were visualized with inverted brightfield microscope Leica DM (Leica Microsystems).

3.7.4 Immunolabeling of 3D collagen sandwich

The cells were fixed with 4% paraformaldehyde in PBS for 30 minutes at room temperature. After fixation, the cells were washed 3x10 minutes in 2 ml PBS-T. The cells were permeabilized with 0.1M glycine, 0.2% Triton X-100 in PBS at room temperature for 1 hour. Followed by extensive washing 3x10 minutes in PBS-T. The top layer of collagen was disrupted by fine aspiration using 10-µl tip to ensure better antibody penetration. Unspecific antibody bidding was blocked with 1 ml of 5% BSA in PBS-T for 2 hours. Primary antibodies diluted in blocking solution were incubated overnight at room temperature. Than the cells were washed 3x15 minutes in PBS-T. After washing, the cells were incubated with secondary antibody and phalloidin at 37°C for 5 hours. The cells were mounted with antifadde mounting media for microscopy (ProLong™ Gold Antifade Mountant (Thermo Fisher Scientific, USA)).

3.8 Quantification of bile canaliculi *in vitro*

For analysis of the bile canaliculi cytoarchitecture *in vitro*, cells were immunolabeled and visualised Leica TCS SP8 confocal microscope (Leica Microsystems; with HC PL APO 63x/1.40 NA oil-immersion objective lens) and Leica STELLARIS 8 FALCON with the LIGHTNING adaptive deconvolution (Leica Microsystems, with HC PL APO 63x/1.40 OIL CS2), the analysis was performed using open-source Fiji software in more than 50 cells per genotype and treatment.

3.9 Statistical analysis

All parametric data are presented as mean ± SEM. Statistical analyses were performed with GraphPad Prism 5 (GraphPad Software) from independent experiments. Differences

between 2 groups were tested using a two-tailed unpaired Student's *t*-test. Two-tailed one-way ANOVA or Bonferroni post-test was used for comparison of multiple groups when appropriate. Statistical significance was determined at the level of $*p < 0.05$, $**p < 0.01$, $***p < 0.001$; the N value is specified in the figure legends.

4 Results

4.1 Plectin localization in mouse liver epithelial cells

To investigate the localization of plectin, we performed immunofluorescence microscopy on paraffin-embedded mouse liver sections. In both hepatocytes and BECs, plectin distinctly marked cell boundaries, partially colocalizing with pan-keratin (pan-K)-positive intermediate filaments (Figure 12A). Additionally, plectin extensively colocalized with the tight junction protein zonula occludens-1 (ZO-1, Figure 12B), adherens junction protein E-cadherin (Figure 12C), and desmosomal protein desmoplakin (Figure 12D) at the surface of BECs and apical domain (canalicular) of hepatocytes.

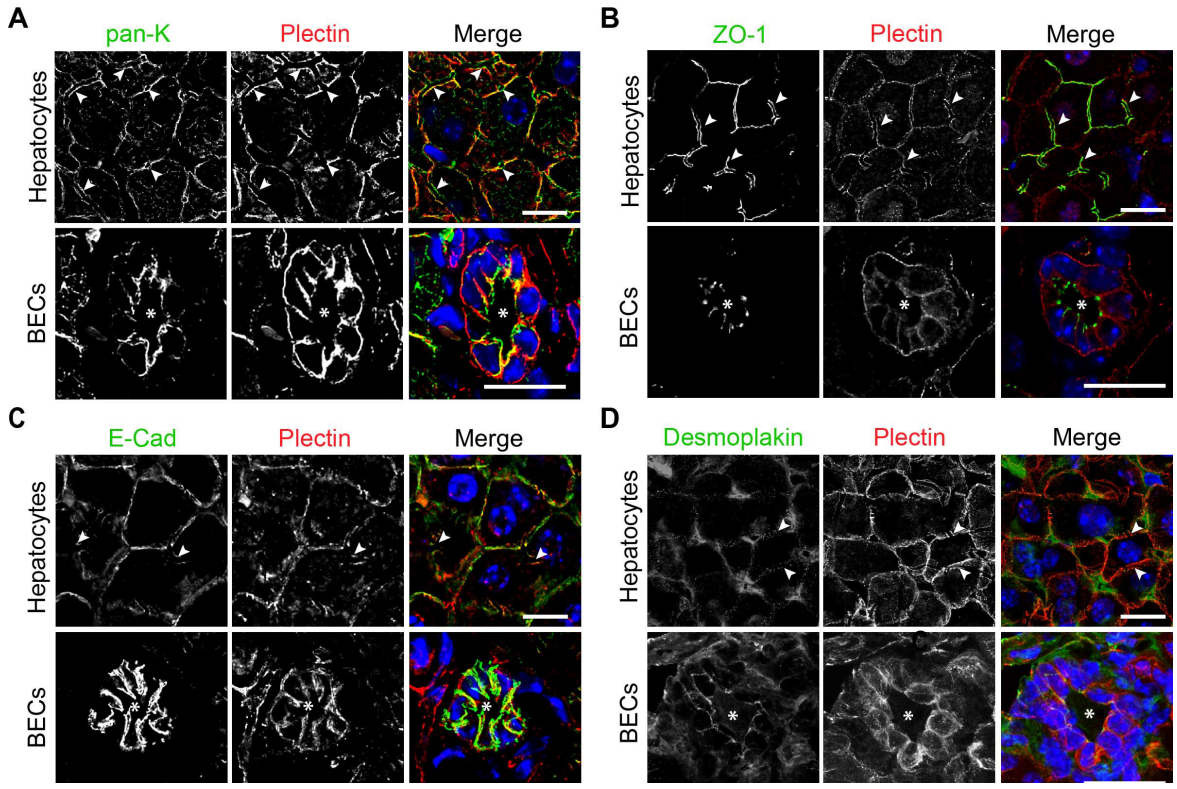

Figure 12. Plectin is expressed in hepatocytes and BECs and partially colocalizes with keratin filaments and junctional complexes in mouse liver epithelial cells. Paraffin mouse liver sections were double immunolabelled using antibodies to plectin (red) and pan-keratin (pan-K, green, **A**), zonula occludens-1 (ZO-1, green, **B**), E-cadherin (E-Cad, green, **C**), or desmoplakin **(**green, **D)**. Detailed images of hepatocytes and biliary epithelial cells (BECs) are shown. Nuclei were stained with DAPI (blue). The arrowheads indicate bile canaliculi, the asterisks mark bile duct lumen. Scale bars, 10 µm.

4.1.1 Plectin defines the cytoarchitecture of keratin filaments of liver epithelial cells

In order to identify plectin's functions in liver epithelium we generated plectin liver specific knockout mouse. Liver-specific deletion of plectin was achieved by crossing Plectin$^{flox/flox}$ mice (*Ple$^{fl/fl}$*) (Ackerl et al. 2007) with Alb-Cre transgenic mice (MGI 2176228; The Jackson Laboratory, Bar Harbor, ME) to generate Plectin$^{lox/lox/Alb\text{-}Cre}$ (*Ple$^{\Delta alb}$*) mice. Successful plectin deletion was confirmed by immunofluorescence images of liver tissue immunolabeled for plectin and pan-keratin (Figure13A). The ablation of *plectin* gene was confirmed at mRNA and proteomic levels in lysates isolated from primary hepatocytes and liver tissue (Figure 13B).

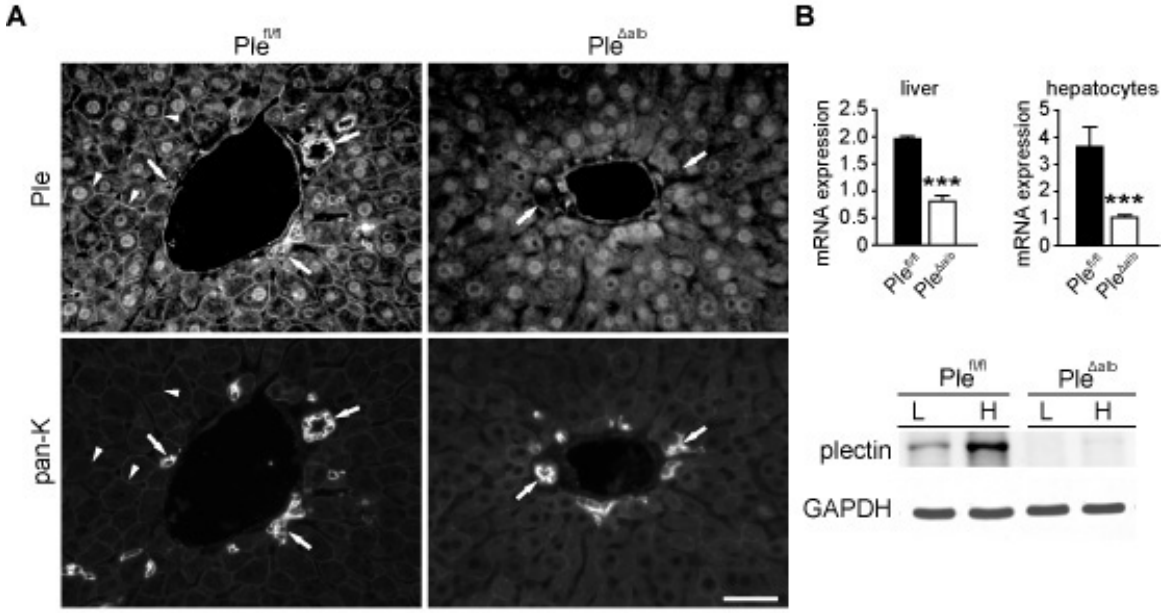

Figure 13. *Characterization of liver-specific plectin knockout (Ple$^{\Delta alb}$) mice.* **(A)** Immunofluorescence images of portal veins (PV) from *Ple$^{fl/fl}$* and *Ple$^{\Delta alb}$* mice, showing staining for pan-keratin (pan-K) and plectin. Arrows indicate bile ducts and surrounding tissue. Scale bar, 50 µm. **(B)** Quantification of plectin expression. Relative mRNA levels of plectin in whole liver lysates and primary hepatocytes isolated from *Ple$^{fl/fl}$* and *Ple$^{\Delta alb}$* mice (N = 6 animals per group). Immunoblot analysis of plectin expression in liver lysates (L) and primary hepatocytes (H), with GAPDH used as a loading control. A significant reduction in plectin expression is observed in *Ple$^{\Delta alb}$* mice. ***$p < 0.001$ calculated using Student's *t*-test. Data are presented as mean + SEM.

To examine plectin depletion in greater detail, we utilized confocal microscopy, which confirmed the loss of plectin in *Ple*$^{\Delta alb}$ mice across all liver tissue, including BECs and hepatocytes as well in 3D collagen sandwich culture of primary hepatocytes (Figure 14).

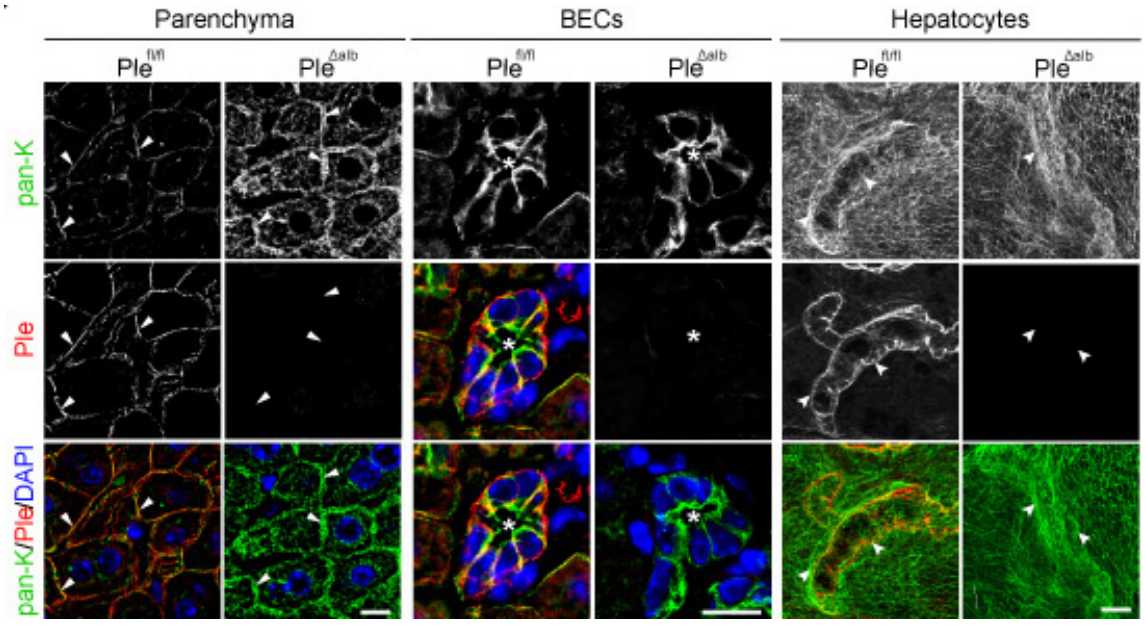

Figure 14. *Successful ablation of plectin in BECs and hepatocytes in Ple*$^{\Delta alb}$ *mouse.* High-resolution immunofluorescence images showing depletion of plectin in the liver parenchyma, bile duct epithelial cells (BECs), and primary hepatocytes isolated from *Ple*$^{fl/fl}$ and *Ple*$^{\Delta alb}$ mice. Nuclei are stained with DAPI (blue). Arrows indicate bile ducts; arrowheads point to bile canaliculi; asterisks mark biliary lumens. Scale bars, 10 µm for parenchyma and BECs; 1 µm for primary hepatocytes.

We next characterized plectin-deficient liver using a range of histological methods to identify possible major liver pathology in plectin-deficient livers. Livers of *Ple*$^{\Delta alb}$ mice at various ages (4- and 12-week-old) showed no significant signs of major pathology during aging (Figure 15A). In more detail, hematoxylin and eosin (H&E) staining revealed normal liver architecture without any apparent signs of inflammation, fibrosis, or cellular damage. Sirius Red and Masson's Trichrome staining showed no detectable collagen deposition or fibrosis. Additionally, periodic acid-Schiff (PAS) staining with diastase treatment demonstrated intact glycogen storage with no abnormal glycogen accumulation in hepatocytes. These findings were supported by the absence of obvious differences in body weight, liver weight, and serum levels of liver injury biomarkers (alanine transaminase (ALT), alkaline phosphatase (ALP), aspartate transaminase (AST), total bilirubin, cholesterol, triglycerides, and total bile acids (tBA)) between *Ple*$^{\Delta alb}$ and control (*Ple*$^{fl/fl}$) mice (Figure 15B).

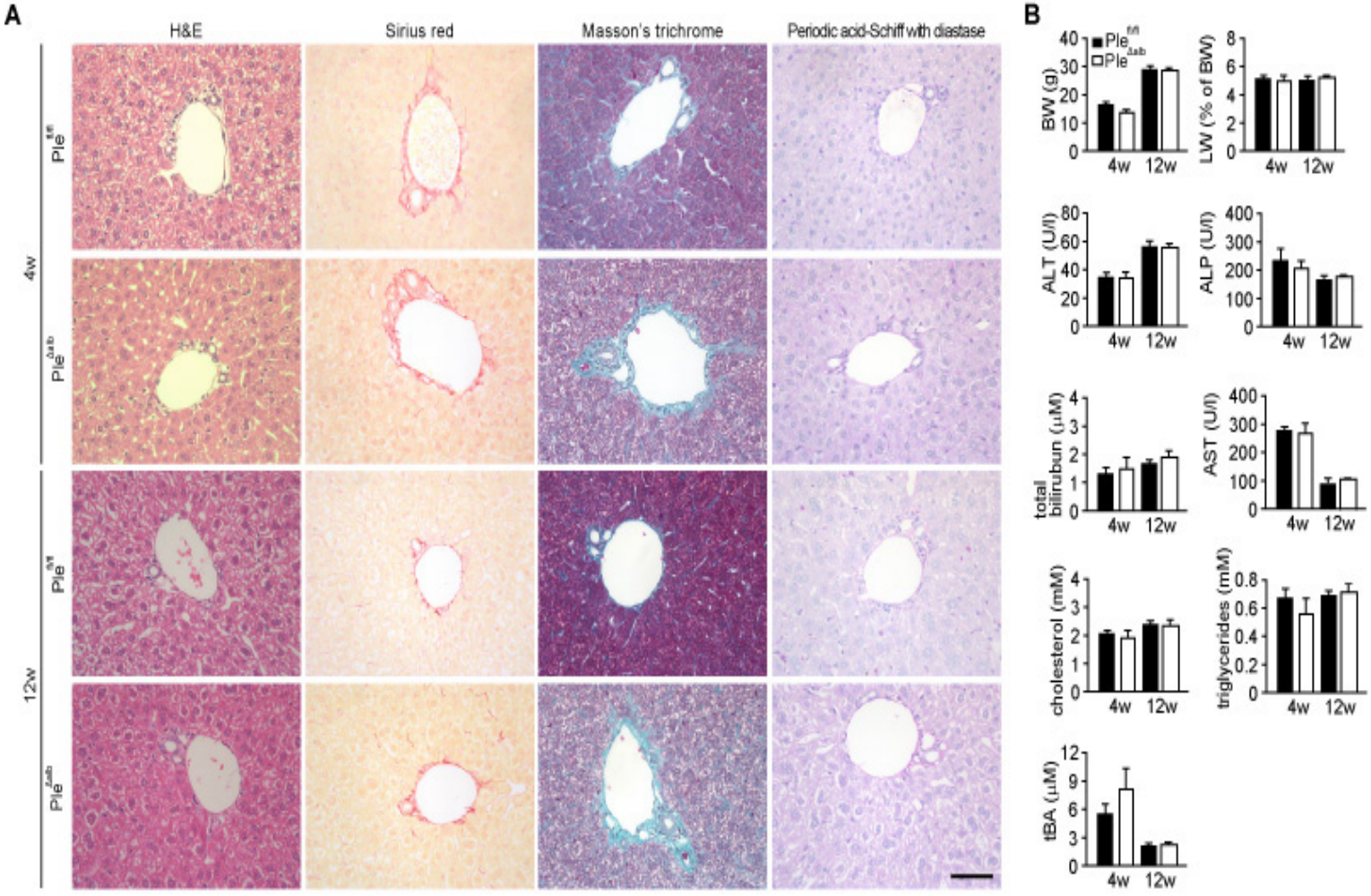

Figure 15. *Histological and biochemical analysis of liver-specific plectin knockout Ple$^{\Delta alb}$ revealed no gross pathology or functional alteration*. **(A)** The *Ple$^{\Delta alb}$* mice exhibit no obvious signs of major pathology. Paraffin liver sections stained with H&E, Sirius red, Masson's trichrome, and Periodic acid-Schiff with diastase (age of animals is indicated in week (w)). **(B)** The *Ple$^{\Delta alb}$* mice show comparable body weight, liver weight, and serum levels of liver injury biomarkers. The graphs show body and liver weights, serum liver markers alanine transaminase (ALT), alkaline phosphatase (ALP), aspartate transaminase (AST), total bilirubin, cholesterol, triglycerides and total bile acids (tBA) analysed in *Ple$^{fl/fl}$* and *Ple$^{\Delta alb}$* mice (age of animals indicated). (N = 4 - 9 animals per group). Student's *t*-test. Scale bar, 250 µm. Data are presented as mean + SEM.

Moreover, analysis of bile flow in untreated *Ple*$^{\Delta alb}$ mice revealed a trend of progressively increased bile flow with age (Figure 16A), bile flow in *Ple*$^{\Delta alb}$ mice was elevated compared to *Ple*$^{fl/fl}$ controls at both 12- and 24-week-old. Notably, this difference became more pronounced in 24-week-old animals, indicating an age-dependent aggravation of bile flow in *Ple*$^{\Delta alb}$ mice.

The analysis of bile 12-week-old animals, showed no distinct differences in bile acid composition between *Ple*$^{\Delta alb}$ and *Ple*$^{fl/fl}$ mice. Despite the increased bile flow in *Ple*$^{\Delta alb}$ mice, there were no substantial changes in the distribution of bile acids. Taurocholic acid and tauro-β-muricholic acid remained the predominant bile acids in both genotypes, though *Ple*$^{\Delta alb}$ mice exhibited subtle alterations in the proportion of some bile acids, including α- and β-muricholic acids. These results suggest that *Ple*$^{\Delta alb}$ mice adapt to increased bile flow by modulating bile acid composition, which may play a role in maintaining bile secretion under conditions of increased bile pressure with aging.

4.1.2 Plectin plays a pivotal role in maintaining the structural integrity of the hepatic cytoarchitecture

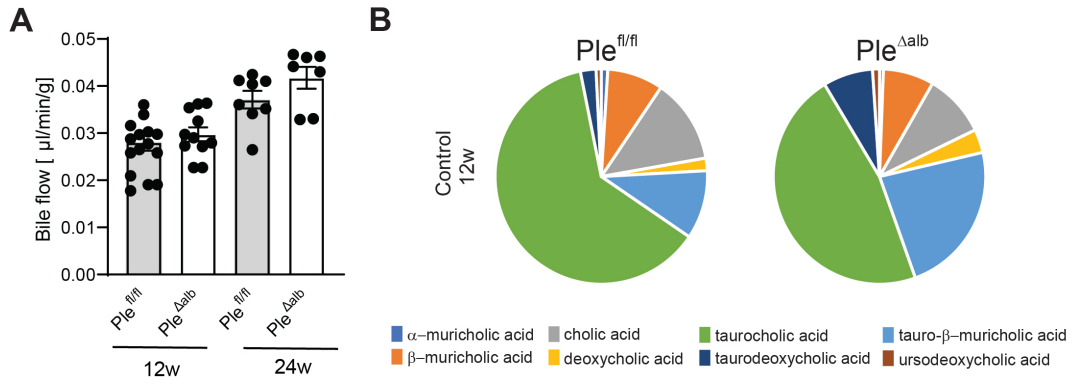

Figure 16. *Bile flow and composition in Ple*$^{fl/fl}$ *and Ple*$^{\Delta alb}$ *untreated mice.* **(A)** The bar graph shows bile flow measured in untreated 12- and 24-week-old *Ple*$^{fl/fl}$ and *Ple*$^{\Delta alb}$ mice (age of animals is indicated in week (w)). 24-week-old *Ple*$^{\Delta alb}$ mice showed a trend of increased bile flow, compared to *Ple*$^{fl/fl}$ controls. (N = 8 - 16 animals per group). Data are presented as mean ± SEM. **(B)** Pie charts show the bile acid composition in untreated *Ple*$^{fl/fl}$ and *Ple*$^{\Delta alb}$. The distribution of bile acids, including taurocholic acid, tauro-β-muricholic acid, and others, reveals changes in bile acid profiles between *Ple*$^{fl/fl}$ and *Ple*$^{\Delta alb}$ mice.

Plectin acts as a cytolinker, connecting intermediate filaments, such as keratin filaments, to other cytoskeletal components like actin filaments and microtubules, providing structural stability and mechanical resilience to cells. We focused on the expression and organization of the keratin filament network in mouse liver parenchyma by immunohistochemistry and immunoblotting. In parallel, we also evaluated other cytoskeletal components, including F-actin, which plays a key role in maintaining the shape and polarity of

hepatocytes. By studying organization of these elements, we aimed to assess how plectin depletion impacts the overall cytoskeletal architecture in the liver.

In healthy *Ple*$^{fl/fl}$ mice, keratin filament network (pan-K, K8 and K18) of the liver parenchyma, displays peri-membranous pattern (Figure 17A), which has been described as a circumferential keratin rim in keratinocytes and MDCKs (Quinlan et al. 2017; Prechova et al. 2022). Keratin immunofluorescence staining exhibited particularly dense distribution around bile canaliculi (Figure 17A).

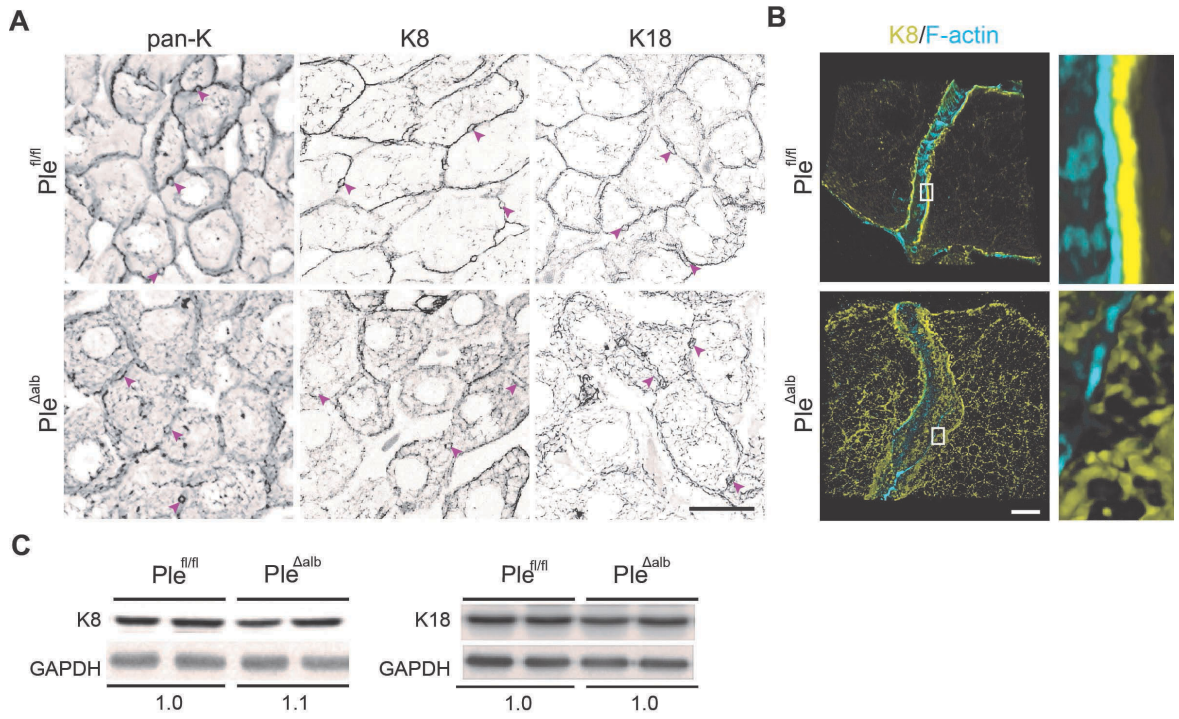

Figure 17. *Plectin organizes keratin filamnets in hepatocytes.* **(A)** Representative images of liver parenchyma where keratin network displays a peri-membranous pattern in control (*Ple*$^{fl/fl}$) mice, whereas keratin filamentsin *Ple*^{Δalb} are lateraly aligned into thicker structures (bundles) throughout the cytoplasm. Immunofluorescence images of pan-keratin (pan-K), K8, and K18. Arrowheads indicate bile canaliculi. Scale bar, 10 µm. **(B)** 3D reconstruction of super-resolution images of hepatic cytoarchitecture in primary hepatocytes (isolated from *Ple*$^{fl/fl}$ and *Ple*^{Δalb} mice), cultured in 3D collagen sandwich, labeled for F-actin (cyan), using phalloidin, and K8 (yellow). Boxed areas show 10x magnified images of bile canaliculus. Scale bar, 1 µm. **(C)** Liver lysates subjected to immunoblotting using antibodies to K8 and K18. GAPDH as loading control. Numbers below lines indicate relative band intensities normalized to average control values. (N = 3 animals per group).

To gain deeper insights into the cytoarchitecture of the bile canaliculi, we utilized super-resolution microscopy, enabling us to observe the intricate structural details of the bile canalicular network and its associated cytoskeletal components with exceptional precision. In primary hepatocytes isolated from *Ple*$^{fl/fl}$ mice, in 3D collagen sandwich culture, K8 (yellow) is distinctly localized along the bile canaliculus, in close proximity to F-actin (cyan) (Figure

17B), which outlines the apical membrane and emphasizes the bile canalicular structure. This close association between K8 and F-actin suggests that these cytoskeletal elements collaboratively provide structural stability to the bile canalicular domain, ensuring its integrity and proper organization.In contrast, the keratin filament networks in $Ple^{\Delta alb}$ hepatocytes appears visibly disorganized, lacking the condensed peri-membranous pattern observed in controls. Instead, the keratin filaments are lateraly aligned into thicker structures (bundles) within the cytoplasm, with a significantly diminished connection to the apical membrane (Figure 17A). Super-resolution images of plectin-deficient mouse primary hepatocytes, in 3D collagen sandwich cultures, further reveal that the keratin filaments collapse inward to the cytoplasm, with a clear separation from the F-actin-rich apical membrane domain (bile canaliculi (Figure 17B)). The alterations observed in the keratin filaments organization were not a consequence of altered keratin expression levels, as no differences were detected in liver lysates by immunoblotting (Figure 17C).

To analyse structural features of bile canalicular network in more detail, we compared canalicular ultrastructure in mouse liver tissue of *Ple*$^{fl/fl}$ and *Ple*$^{\Delta alb}$ mice as well as in 3D collagen sandwich cultures of mouse primary hepatocytes using scanning electron microscopy (SEM) and light microscopy techniques. The SEM micrographs revealed in *Ple*$^{\Delta alb}$ liver distorted, wider, and more meandering bile canaliculi with frequent blind end loops (Figure 18A), which was in sharp contrast with regularly shaped *Ple*$^{fl/fl}$ canaliculi. A quantitative analysis of bile canalicular morphology showed a significantly wider range of the bile canaliculus widths in *Ple*$^{\Delta alb}$ compared to *Ple*$^{fl/fl}$ livers (Figure 18A, histogram). The 3D reconstructions and filament tracing analysis of 10-µm-thick liver sections immunolabeled with ZO-1 showed the presence of an increased number of branching points, further indicating a denser and more complex canalicular network in *Ple*$^{\Delta alb}$ compared to *Ple*$^{fl/fl}$ liver (Figure

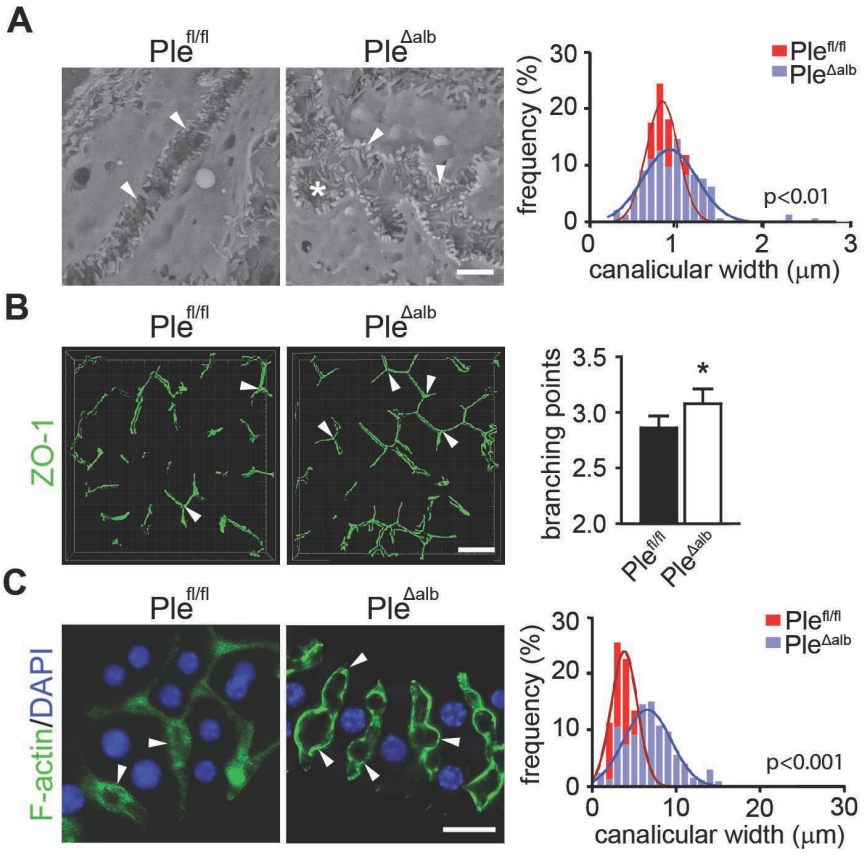

Figure 18. *Alterations in morphology and spatial arrangement of bile canaliculi network in response to plectin deficiency.* **(A)** Representative SEM micrographs of bile canaliculi. The arrowheads indicate bile canaliculi; the asterisk, blind loop in *Ple*$^{\Delta alb}$ canaliculi only. Scale bar, 1 µm. Histogram of morphometric analysis of canalicular (N = 2 animals per group, 6 images). **(B)** 3D reconstruction of ZO-1-immunolabelled bile canaliculi (the arrowheads pointing to branching points). Scale bar, 10 µm. The bar graph shows the average number of branching points. (N = 6 animals per group). Data are presented as mean + SEM. **(C)** Primary hepatocytes isolated from *Ple*$^{fl/fl}$ and *Ple*$^{\Delta alb}$ mice, in 3D collagen sandwich culture, labelled with phalloidin to visualize F-actin (green). Nuclei were stained with DAPI (blue). The arrowheads indicate bile canaliculi. Scale bar, 1 µm. The histogram shows the canalicular width distribution. (N = 3 biological replicates, 68-80 bile canaliculi). *$p < 0.05$ calculated using Student's *t* -test.

18B). Additionally, immunofluorescence microscopy of F-actin labelled 3D collagen sandwich cultures of *Ple*$^{fl/fl}$ and *Ple*$^{\Delta alb}$ primary hepatocytes exhibited highly irregular and significantly wider *Ple*$^{\Delta alb}$ canaliculi with grossly dilated segments (Figure 18C), which closely recapitulate the abnormalities observed in a canalicular network *Ple*$^{\Delta alb}$ *in vivo* (Figure 18A).

4.1.3 Plectin deficiency affects BECs cytoarchitecture

Unlike in hepatocytes, the keratin filament network in BECs displays polarized pattern that is associated with secretory processes (Omary et al. 2002; Zatloukal et al. 2004). The BECs express K8 and K18, as evidenced by the immunoflurescence images (Figure19). The results of the quantitative fluorescence microscopy demonstrated that the absence of plectin resulted in a considerable reduction in K18 fluorescence intensity at the apical membrane of BECs (Figure19), the box plot).

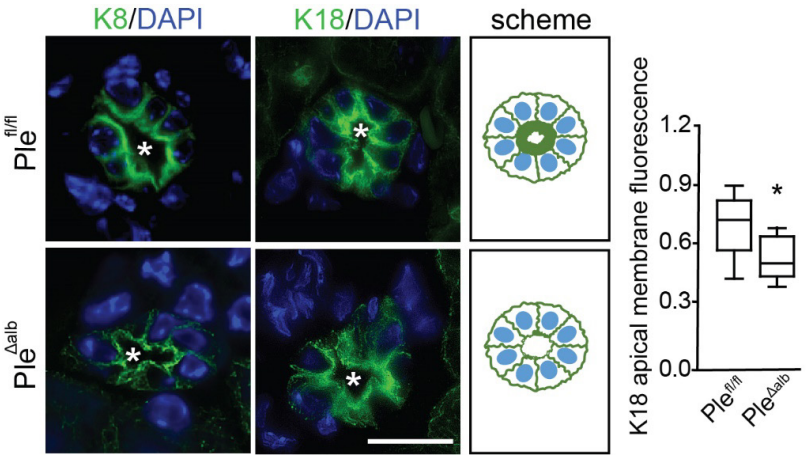

Figure 19. *Plectin controls K8/18 organization in BECs.* BECs of *Ple*$^{\Delta alb}$ are losing polarized K8/18 cytoarchitecture. Detailed images of bile duct and individual BECs immunolabeled for K8/18 (green). Nuclei were stained with DAPI (blue). Drawn scheme illustrates reduced apical membrane K18 staining in *Ple*$^{\Delta alb}$ BECs. The asterisks indicate biliary lumen. Scale bars, 10 µm. The graph shows the quantification of the apical membrane fluorescence intensities in individual BECs normalized to total fluorescence intensity per cell. The box represents the 25-75th percentiles, and the median is indicated. (N = 3 animals per group, BECs >250). *$p < 0.05$ calculated using Student's *t* test.

Unlike hepatocytes, the BECs additionally express K7 and K19 (Figure 20A, immonoflurescence images). The quantitative fluorescence microscopy indicated that the absence of plectin resulted in an elevated fluorescence intensity of K19 at the basal membrane of BECs (Figure 20A, the box plot). At the same time, overall K19 levels in liver lysates were not grossly affected (Figure 20B).

The relocalisation of K18 and K19 implies the potential partial loss of the typically polarized keratin cytoarchitecture in *Ple*$^{\Delta alb}$ BECs with unaltered expression levels (Figure 17C and Figure 20B).

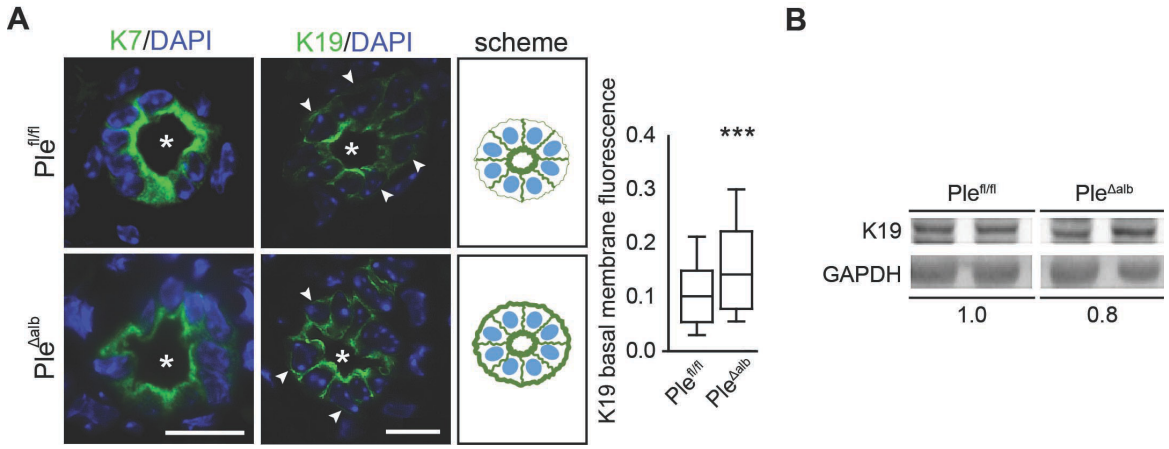

Figure 20. *Plectin controls K7/19 organization in BECs.* **(A)** BECs of *Ple*$^{\Delta alb}$ are losing polarized K7/19 cytoarchitecture. Detailed images of bile duct and individual BECs immunolabeled for K7/19 (green). Nuclei were stained with DAPI (blue). Drawn schemes illustrate increased basal membrane K19 staining in *Ple*$^{\Delta alb}$ BECs. The asterisks indicate biliary lumen; the arrowheads point to basal membrane of BECs. Scale bars, 10 µm. The graph shows the quantification of the apical membrane fluorescence intensities in individual BECs normalized to total fluorescence intensity per cell. The box plot represents the 25-75th percentiles, and the median is indicated. (N = 3 animals per group, BECs >250). ***$p < 0.001$ calculated using Student's *t* test. **(B)** Liver lysates subjected to immunoblotting using antibodies to K19. GAPDH as loading control. Numbers below lines indicate relative band intensities normalized to average control values.

Given the canalicular dysmorphology in *Ple*$^{\Delta alb}$ parenchyma and *in vitro* hepatocytes we next assessed whether plectin ablation also affected formation and morphology of the bile ducts. The morphometric analysis, conducted on K19-immunolabelled intralobular bile ducts and luminised ductules in mice during aging (4-, 12-, 20- and 40-week-old animals), exhibited a reduction in the cross-sectional luminal area both bile ducts and ductules in *Ple*$^{\Delta alb}$ mice, while no differences in the luminal perimeter were observed when compared to *Ple*$^{fl/fl}$ mice (Figure 21). Further characterization of the luminal shape by quantification of the circularity and axial ratio revealed significantly irregular and elongated ductular lumens in *Ple*$^{\Delta alb}$ livers in comparison to more rounded lumens in *Ple*$^{fl/fl}$ livers (Figure 21).

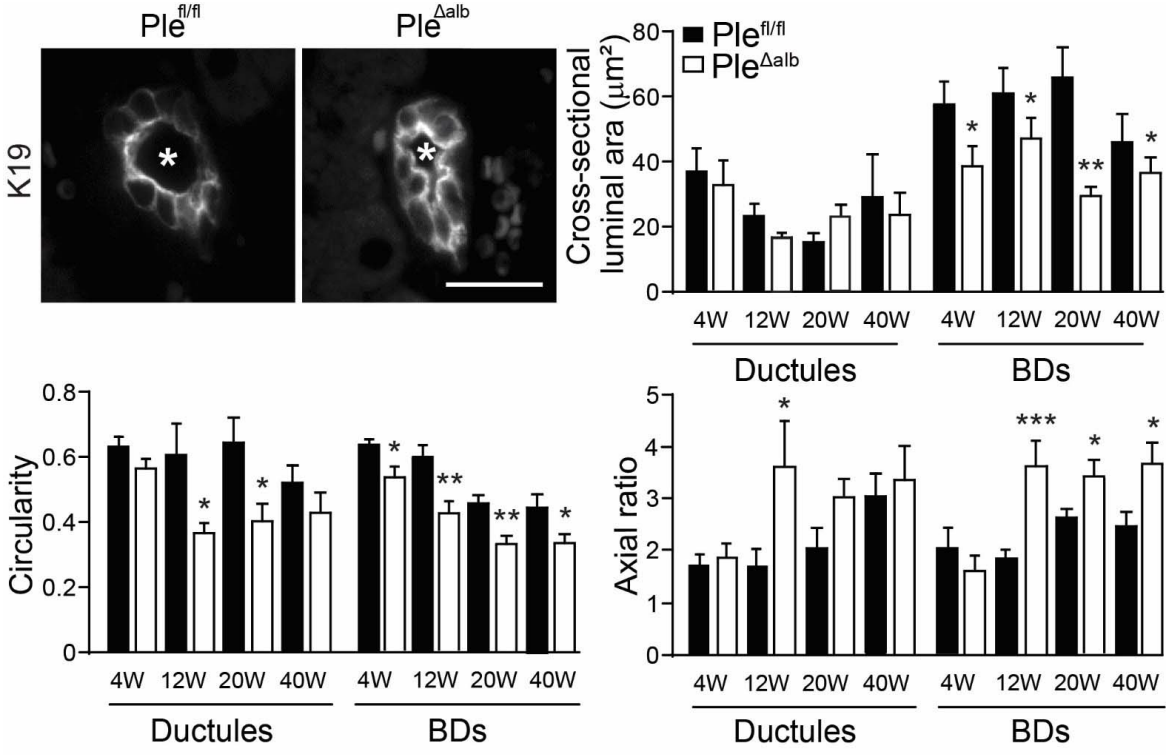

Figure 21. *Biliary tree malformation in Ple$^{\Delta alb}$ mice.* Immunofluorescence images for BECs immunolabelled with K19. The bar graphs indicate malformation of biliary lumen shown by morphological quantification of interlobular ductules and bile ducts (BD) in *Ple$^{fl/fl}$* and *Ple$^{\Delta alb}$* liver sections from 4-, 12-, 20- and 40-week-old mice. Age of animals indicated in week (w). The asterisks indicate biliary lumen. Scale bar, 10 µm. (N = 3 animals per group). *$p < 0.05$, **$p < 0.01$, ***$p < 0.001$ calculated using Student's *t* -test. Data are presented as mean + SEM.

The ductular dysmorphology was accompanied by a significant increase in the number of ductules and K19-positive (K19$^+$) cells per portal field in *Ple$^{\Delta alb}$* livers (Figure 22A). In contrast, there was no significant change in the number of interlobular bile ducts or individual K19$^+$ cells compared to *Ple$^{fl/fl}$* livers (Figure 22A). A further analysis demonstrated a comparable content of A6-positive (A6$^+$) progenitor/oval cells between the *Ple$^{fl/fl}$* and *Ple$^{\Delta alb}$* livers (Figure 22B). These findings imply that under physiological conditions, aberrant keratin filaments cytoarchitecture in plectin-deficient BECs results in the collapse of ductular lumens leading thus to mild ductular reaction.

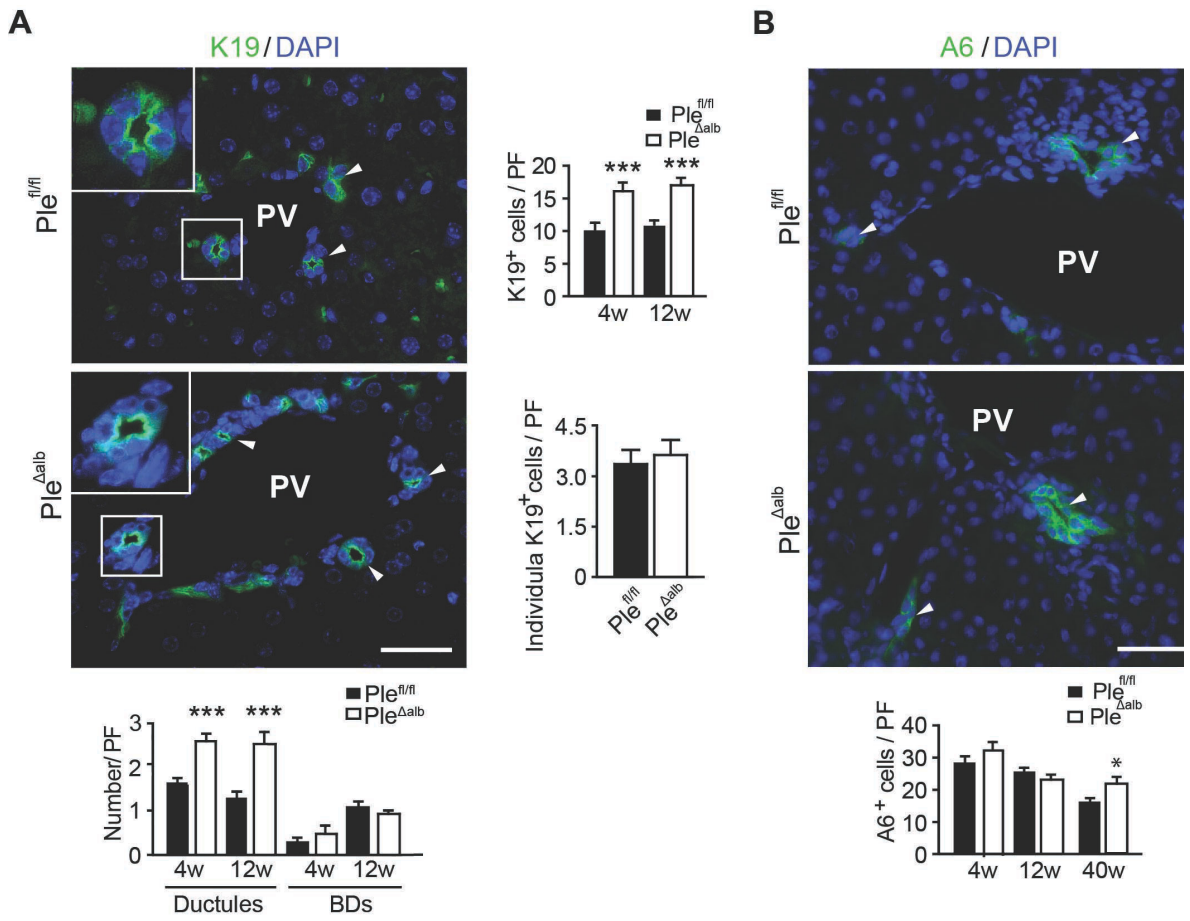

Figure 22. *Mild ductular reaction in Ple$^{\Delta alb}$ mice.* **(A)** Representative immunofluorescence images of portal vein (PV) fields from liver sections immunolabelled for K19 (green). Nuclei stained with DAPI (blue). The arrowheads indicate ductular structures. Boxed images show 2x magnified bile duct (BD). The *Ple$^{\Delta alb}$* BDs are misshaped. The bar graphs show the number of K19-positive (K19^{+}) cells, the number individual K19^{+} cells and the number of ductules and bile ducts per portal field (PF). (N = 3 animals per group, >10 PF). Scale bar, 50 µm. **(B)** Representative immunofluorescence images of portal fields from liver sections immunolabelled for A6 epitope (green), the marker of the progenitor cells. The bar graph shows the number of A6-positive (A6^{+}) cells per PF. Age of animals indicated in week (w). (N = 3 animals per group, >10 PF). Scale bar, 75 µm. *$p < 0.05$, ***$p < 0.001$ calculated using Student's *t* test. Data are presented as mean + SEM.

4.2 Plectin plays a crucial role in maintaining tissue integrity by enabling an adaptive cellular response to cholestatic stress

Given that plectin has been reported to protect keratin filament cytoarchitecture from various stresses (Moch et al. 2016), we examined how plectin liver expression changes with injury. In two experimental mouse models of cholestasis, we observed significantly elevated levels of plectin at mRNA and protein levels in livers subjected to BDL or in animals fed with a diet containing 3,5-diethoxycarbonyl-1,4-dihydrocollidine (DDC) (Figure 23A, B). Consistent with previous studies, this upregulation was accompanied by increased expression of K18 and K19 (Figure 23B). These findings suggest a potential role for plectin in the response

to cholestatic liver disease, in line with recent case reports documenting severe cholestasis in infants with plectin mutations (Wu et al. 2019; Thebaut et al. 2024; Kor-Anantakul et al. 2024).

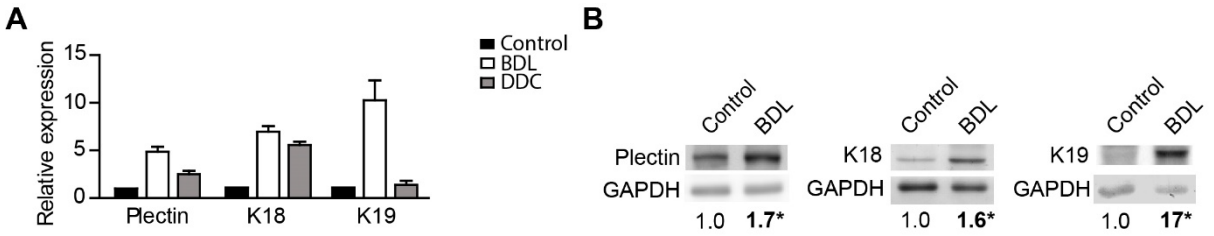

Figure 23. *Expression levels of plectin and keratins are elevated in cholestatic mouse models.* **(A)** The relative mRNA levels of *plectin*, *K18,* and *K19* in livers of mice challenged with BDL, the DDC diet, and untreated controls. (N = 4 animals per group). **(B)** Immunoblots of liver lysates prepared from mice challenged with BDL or unchallenged controls using antibodies to plectin, K18 and K19. GAPDH, as loading control. Numbers below lines indicate relative band intensities normalized to average control values. (N = 3-4 animals per group). **p* < 0.05 calculated using Student's *t* test. Data are presented as mean + SEM.

To determine whether the considerable elevation in plectin expression observed during cholestatic challenge reflects its protective role in liver injury, we subjected $Ple^{fl/fl}$ and $Ple^{\Delta alb}$ mice to various experimental cholestatic models, including BDL, the DDC diet, and the cholic acid (CA) diet.

4.2.1 Plectin deficiency exacerbates BDL-induced liver injury

Mice subjected to BDL for 5 and 14 days exhibited a pronounced development of jaundice, accompanied by significant elevations in serum liver injury biomarkers, including ALT, ALP, total bilirubin, and tBA, when compared to the sham-operated control group.

Although $Ple^{fl/fl}$ and $Ple^{\Delta alb}$ mice both exhibited increased levels of serum liver injury

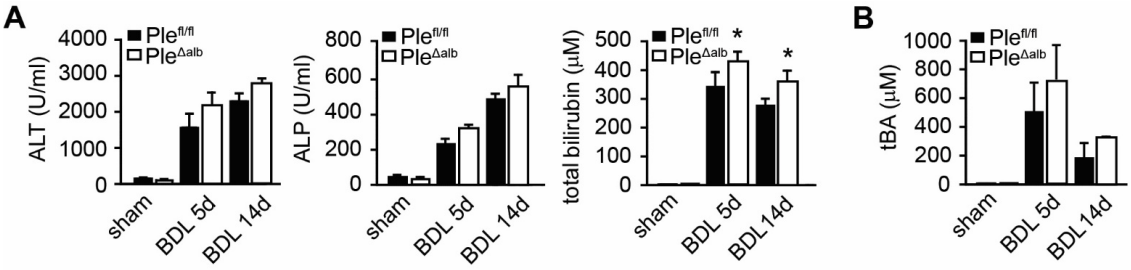

Figure 24. *Liver-specific deficiency of plectin caused elevated levels of liver injury biomarkers in BDL-induced cholestasis*. **(A, B)** The bar graphs show serum levels of liver injury makters (ALT, ALP, total bilirubin (A) and total serum bile acid (tBA; B)) in $Ple^{fl/fl}$ and $Ple^{\Delta alb}$ sham-operated controls (Sham) and mice 5 and 14 days (5d and 14d) post-BDL. (N = 6 - 7 animals per group). *p < 0.05 calculated using Student's *t* -test. Data are presented as mean + SEM.

biomarkers following BDL, $Ple^{\Delta alb}$ mice demonstrated more pronounced liver injury. Notably,

ALT and ALP levels were elevated in both genotypes, but the increase in total bilirubin was significantly higher in *Ple*$^{\Delta alb}$ mice, particularly at 14 days post-BDL (Figure 24A). This suggests that the absence of plectin exacerbates the cholestatic injury, as indicated by the excessive jaundice. Additionally, while tBA levels increased in both groups, they remained higher in *Ple*$^{\Delta alb}$ mice, suggesting a greater impact on bile acid homeostasis (Figure 24B). These findings indicate that plectin deficiency aggravates liver injury, with *Ple*$^{\Delta alb}$ mice displaying more severe cholestasis compared to controls.

A histological analysis of liver sections 14 days post-BDL demonstrated a significant increase in the number and area of biliary type of hepatocytic necrosis (known as bile infarcts) in *Ple*$^{\Delta alb}$ compared to *Ple*$^{fl/fl}$ livers (Figure 25A). Furthermore, an analysis of Sirius red-stained liver sections and immunoblot analyses for collagen I and α-smooth muscle actin revealed that *Ple*$^{\Delta alb}$ livers exhibited more extensive fibrosis (Figure 25B).

The regenerative changes observed in the biliary tree revealed significantly elevated rate of BECs proliferation in *Ple*$^{\Delta alb}$ mice following a 14-day injury period, as demonstrated by Ki67 staining (Figure 26A). It is noteworthy that A6 antigen staining revealed a two-fold

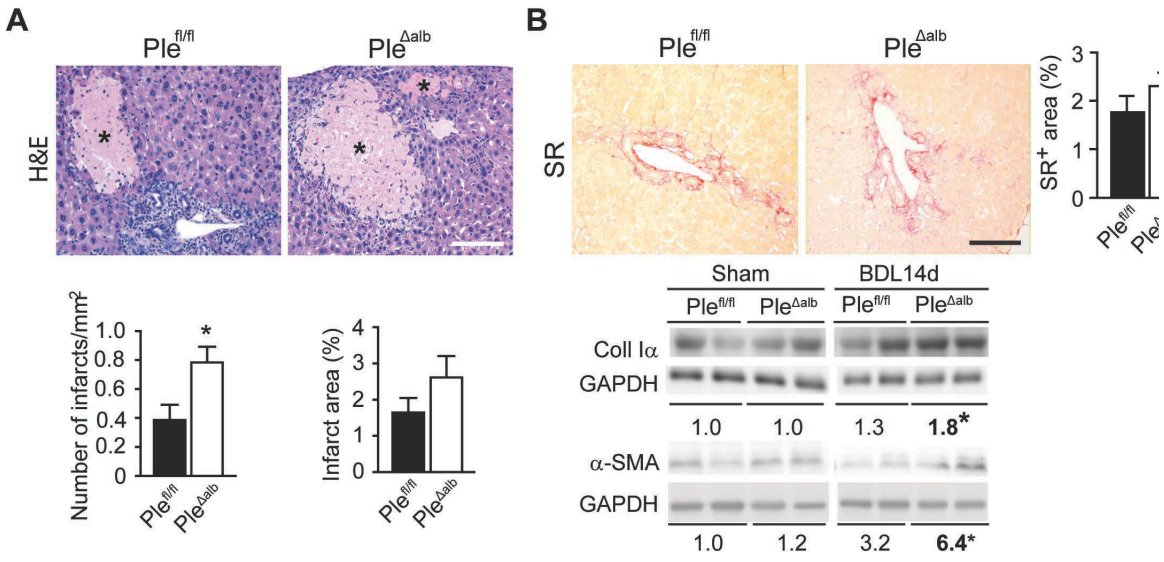

Figure 25. *Liver-specific deficiency of plectin exacerbates BDL-induced injury.* **(A)** Representative images of H&E-stained liver sections of *Ple*$^{fl/fl}$ and *Ple*$^{\Delta alb}$ mice 14 days (14d) post-BDL showing hepatic bile infarcts (the asterisks). The bar graphs show bile infarct scoring (number and area of infarct per liver area). (N = 6 animals per group). **(B)** Representative images of Sirius red (SR)-stained liver sections from BDL-treated mice. Scale bar, 200 µm. The bar graph shows the percentage of the SR-positive (SR^+) area per liver section. (N = 8 animals per group). Immunoblots labelled for to collagen I and α-smooth muscle actin (α-SMA). GAPDH, as loading control. The numbers below lines indicate relative band intensities normalized to average control values. (N = 3 - 4 animals per group). *p < 0.05 calculated using Student's *t* -test. Data are presented as mean + SEM.

increase in the progenitor cell area in *Ple*$^{\Delta alb}$ mice following both 5 and 14 days post-BDL recovery (Figure 26B). The overall ductular reaction described as K19^{+} areas on liver sections

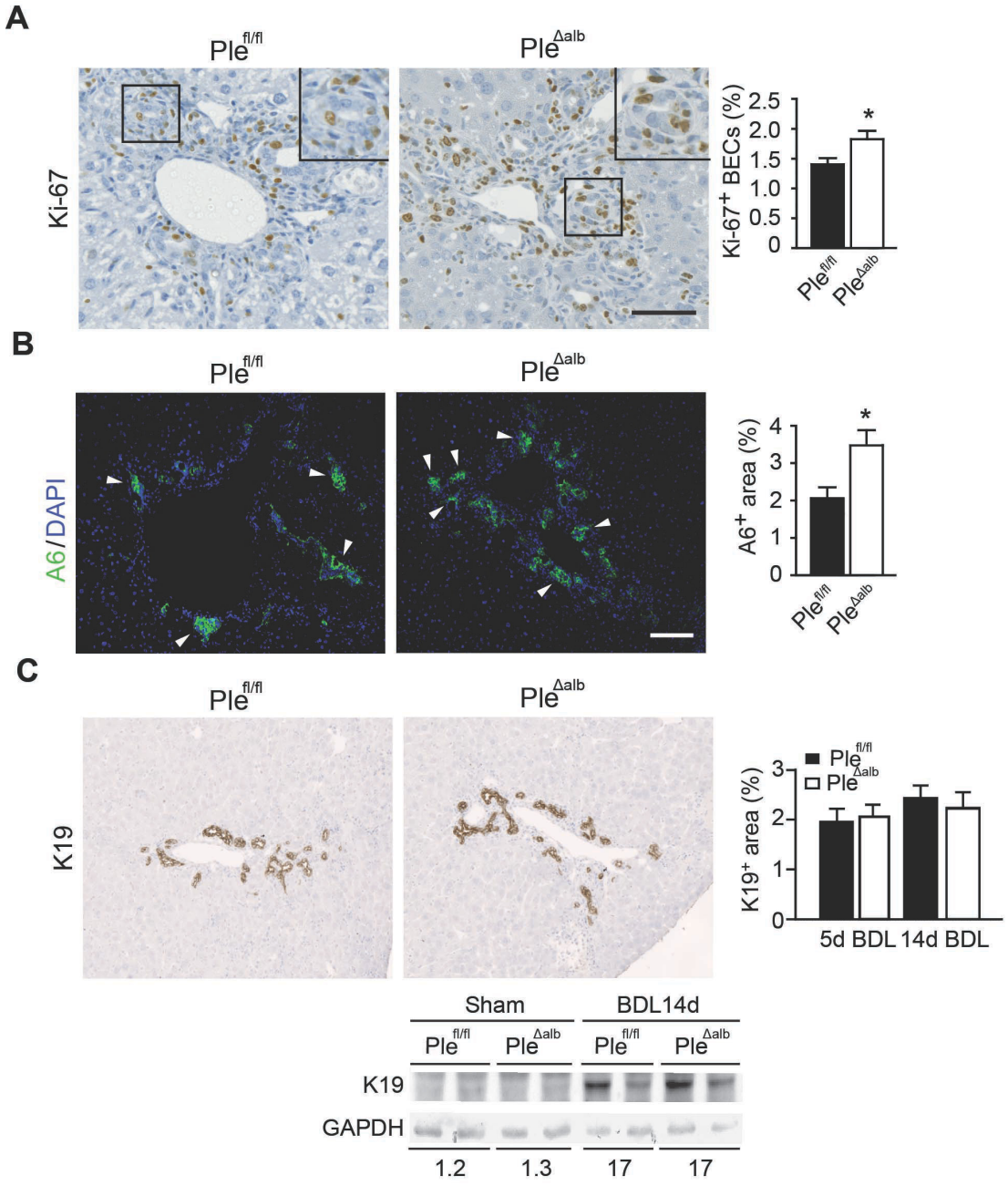

Figure 26. *Liver-specific plectin deficiency increases the ductular proliferation in response to BDL-induced injury.* **(A)** Representative images of liver sections from mice 14 days (14d) post-BDL immunolabelled for Ki-67. Boxed images show 2x magnified of bile duct. Nuclei stained with hematoxylin (blue). Scale bar, 150 µm. The bar graph shows the percentage of Ki67-positive (Ki67^{+}) BECs. (N = 3 - 4 animals per group). **(B)** Immunofluorescence images of liver sections 14d post-BDL immunolabelled for A6 epitope (green), nuclei stained with DAPI (blue). The arrowheads indicate A6-positive (A6^{+}) cells. Scale bar, 200 µm. The bar graph shows the percentage of the A6^{+} area per liver section. (N = 3 animals per group). **(C)** Immunofluorescence images of liver tissue 14d post-BDL immunolabeled for K19, nuclei stained with hematoxylin (blue). Scale bar, 200 µm. The bar graph shows the percentage of the K19^{+} area per liver section. (N = 3 animals per group). **p* < 0.05 calculated using Student's *t*-test. All data are presented as mean + SEM.

and an immunoblot analysis of liver lysates, was comparable between $Ple^{fl/fl}$ and $Ple^{\Delta alb}$ mice both 5 and 14 days post-BDL (Figure 26C). Nevertheless, the collective evidence indicates that $Ple^{\Delta alb}$ mice exhibit increased susceptibility to BDL-induced injury, characterized by augmented portal fibrosis and substantial BECs proliferation and activation of progenitor cells.

4.2.2 Plectin is required for the restoration of liver tissue upon DDC-induced injury

As BDL-induced cholestasis primarily affects large bile duct epithelial cells, modeling extrahepatic cholestasis, we further investigated the role of plectin in a second cholestatic model, the DDC-feeding model, which predominantly targets small bile ducts and ductules, thus mimicking intrahepatic cholestasis. In contrast to the findings from the BDL model, after 14 days of DDC feeding, $Ple^{fl/fl}$ mice displayed significantly higher levels of ALT and tBA compared to $Ple^{\Delta alb}$ mice, indicating more pronounced hepatocellular damage and slower bile flow in the controls $Ple^{fl/fl}$ (Figure 27A and B). This suggests that plectin deficiency in $Ple^{\Delta alb}$ mice might offer partial protection to liver epithelia under DDC-induced injury.

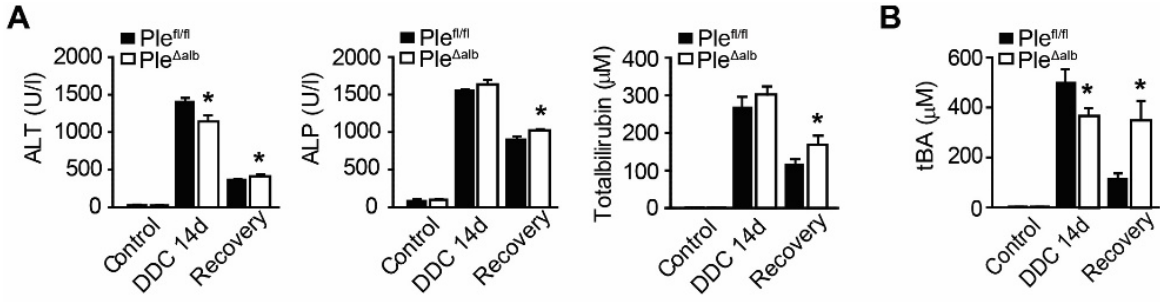

Figure 27. *Liver-specific deficiency of plectin hampers recovery from DDC-induced cholestasis.* **(A, B)** The bar graphs show serum levels of liver injury markers of $Ple^{fl/fl}$ and $Ple^{\Delta alb}$ mice determined in samples from untreated controls, mice fed with the DDC for 14 days (14d), and allowed to recover from the injury for 3 days (recovery). ALT, ALP, total bilirubin (A), and total serum bile acid (tBA; B). (N = 3-7 animals per group). $*p < 0.05$ calculated using Student's *t*-test. Data are presented as mean + SEM.

Interestingly, this reduced hepatocellular damage in $Ple^{\Delta alb}$ mice was accompanied by reduced fibrosis, as shown by Sirius Red staining of liver sections (Figure 28A). However, the extent of the ductular reaction and proliferative response to DDC-induced injury was comparable between genotypes, with no significant differences observed in $K19^+$ areas, K19 expression levels, or Ki-67 staining, indicating similar levels of ductal cell proliferation and regeneration across both genotypes (Figure 28B and C). Surprisingly, we observed a more than threefold increase in $A6^+$ progenitor cell area in treated $Ple^{\Delta alb}$ mice, indicating a stronger activation of progenitor cells in response to DDC-induced injury (Figure 28D).

After a 3-day recovery period from 14 days of DDC-induced injury, $Ple^{fl/fl}$ mice exhibited a fivefold reduction in tBA levels, indicating significant recovery and efficient bile acid clearance. In contrast, $Ple^{\Delta alb}$ mice showed almost no reduction in tBA levels, which remained elevated, suggesting impaired bile acid clearance and delayed recovery from cholestatic injury in absence of plectin (Figure 27B).

Moreover, persistent fibrosis was consistently observed in $Ple^{\Delta alb}$ mice during the recovery phase, as shown by Sirius red-stained sections (Figure 28A). Interestingly, despite the ongoing fibrosis, both $Ple^{fl/fl}$ and $Ple^{\Delta alb}$ mice displayed a similar extent of ductular reaction and proliferative response, with $A6^+$ progenitor cells returning to levels comparable to treated $Ple^{fl/fl}$ mice during recovery. This suggests that plectin loss enhances progenitor cell activation during injury but does not significantly affect their numbers during recovery.

These findings indicate that in the DDC model, plectin deficiency increases the susceptibility of BECs to DDC-induced injury, leading to elevated progenitor cell activation. However, plectin deficiency appears to protect the hepatic parenchyma, as evidenced by the reduced hepatocellular damage observed in $Ple^{\Delta alb}$ mice. Despite the reduced liver injury, plectin deficiency impairs the resolution of cholestasis and bile acid clearance, leading to persistent fibrosis and delayed recovery.

Collectively, these results suggest that while plectin plays a crucial role in bile acid homeostasis and recovery from cholestatic injury, its absence may provide a protective asvantage to hepatocytes during injury, but at the cost of prolonged fibrosis and impaired bile acid clearance.

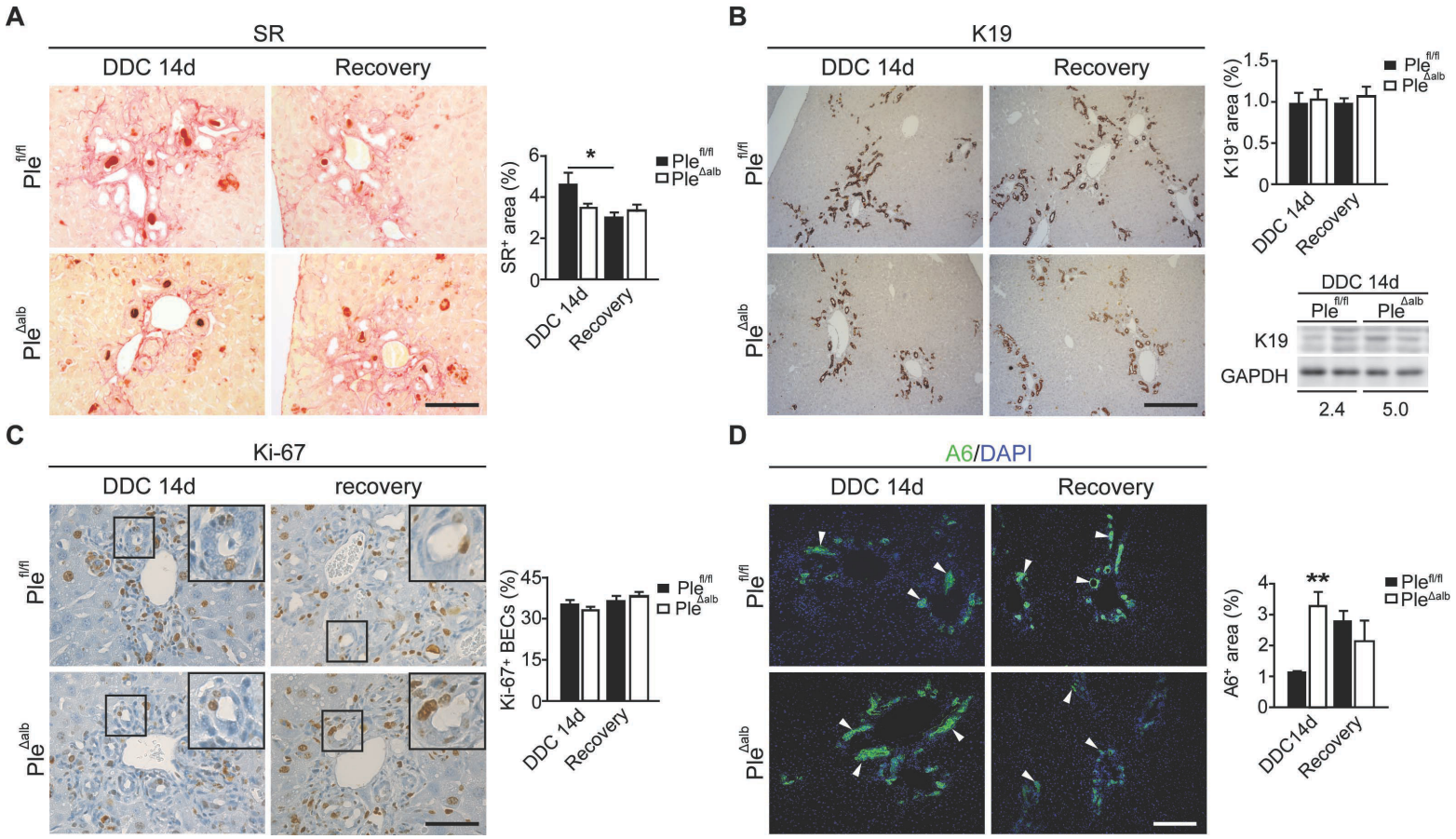

Figure 28. *Ple$^{\Delta alb}$ mice show impaired recovery from DDC-induced injury.* **(A)** Representative images of paraffin sections of *Ple$^{fl/fl}$* and *Ple$^{\Delta alb}$* untreated control mice and mice fed with the DDC diet for 14 days (14d), or allowed to recover from the injury for 3 days (recovery). Sirius red (SR)-stained sections from DDC-fed and recovering mice show less extensive fibrosis in *Ple$^{\Delta alb}$*. Scale bar, 150 µm. The bar graph shows the percentage of the SR-positive (SR$^+$) area per liver section. (N = 6 animals per group). **(B)** Representative images of K19-immunolabeled liver sections from DDC-fed and recovering mice. Scale bar, 250 µm. The bar graph shows the percentage of the K19$^+$ area per liver section. (N = 6 animals per group). Expression levels of K19 are comparable between genotypes as shown by immunoblots of liver lysates using antibodies to K19. GAPDH, as loading control. Numbers below lines indicate relative band intensities normalized to average control values. (N = 3 - 4 animals per group). **(C)** Representative images of Ki67-immunolabeled liver section from DDC-fed and recovering mice. Boxed images show 2x magnified bile duct. Nuclei stained with hematoxylin (blue). Scale bar, 150 µm. The bar graph shows the percentage of the Ki67$^+$ BECs. (N = 6 animals per group). **(D)** Representative immunofluorescence images of A6 (green) immunolabelled liver sections from DDC-fed and recovering mice. Nuclei stained with DAPI (blue). The arrowheads indicate A6$^+$ cells. Scale bar, 200 µm. The bar graph shows the percentage of the A6$^+$ area per liver section. (N = 3 - 4 animalsper group). *$p < 0.05$, **$p < 0.01$ calculated using Student's *t*-test. Data are presented as mean + SEM.

4.2.3 Plectin deficiency aggravates CA-induced liver injury

Unlike obstructive models of cholestasis, CA-induced cholestasis represents a non-obstructive model that affects the entire biliary tree, offering a unique perspective for studying cholestatic liver injury. This model provides insight into how bile acid overload, rather than physical blockage, contributes to biliary dysfunction and liver pathology. The findings from the CA-feeding experiment align with those observed in previously described cholestatic models, but also reveal unique aspects of cholic acid (CA)-induced cholestasis. After a 14-day CA-feeding period, *Ple*$^{\Delta alb}$ mice exhibited elevated levels of liver injury biomarkers, including ALT, AST, and tBA, compared to *Ple*$^{fl/fl}$ mice (Figure 29A). The slightly elevated tBA levels in the serum suggest impaired bile acid clearance and more severe cholestasis in *Ple*$^{\Delta alb}$ mice. Pronounced increase in ALT and AST levels signifies more extensive hepatocellular damage in the absence of plectin, highlighting plectin's protective role in maintaining liver integrity during cholestatic stress.

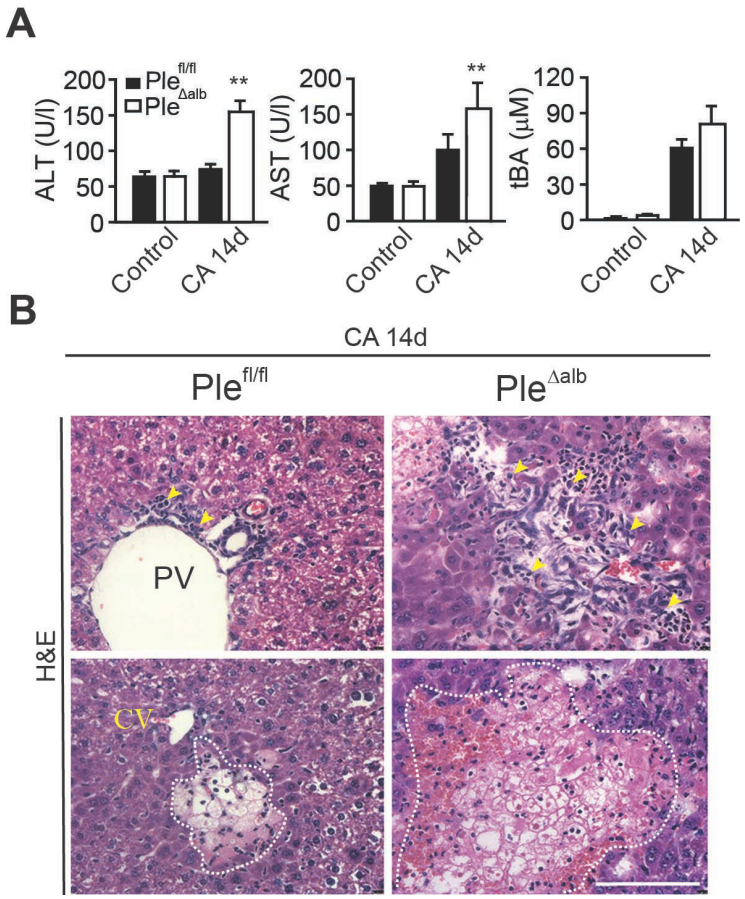

Figure 29. *Liver-specific deficiency of plectin aggravates biochemical and histopathological outcomes of CA-induced injury.* **(A)** Serum levels of liver injury markers *Ple*$^{fl/fl}$ and *Ple*$^{\Delta alb}$ determined in samples from untreated controls and mice fed with the CA diet for 14 days (14d). The bar graphs show the levels ALT, AST, and tBA. (N = 3 - 7 animals per gorup). **(B)** Histopathological evaluation revealed elevated infiltration of immune cells (yellow arrowheads) at periportal zone (portal vein; PV) and an increased size and number necrotic foci at pericentral zone (central vein; CV; marked by dashed line). Representative images of H&E-stained liver tissue of *Ple*$^{fl/fl}$ and *Ple*$^{\Delta alb}$ mice fed with CA for 14d. $^{**}p < 0.01$ calculated using Student's *t*-test. Data are presented as mean + SEM.

Histological examination using H&E staining supported these biochemical findings, revealing increased infiltration of immune cells around the periportal region and larger and more numerous necrotic foci in the pericentral region of *Ple*$^{\Delta alb}$ mice compared to *Ple*$^{fl/fl}$ controls (Figure 29B). The presence of immune cell infiltration

indicates an inflammatory response, a hallmark of cholestatic liver injury, while the expanded necrotic foci in *Ple*$^{\Delta alb}$ mice suggest a more severe bile necrosis.

Further histological analysis of Ki67-positive (Ki67^{+}) proliferating epithelial cells across different liver regions revealed that Ki67^{+} cells were predominantly BECs. No significant difference was detected between *Ple*$^{\Delta alb}$ and *Ple*$^{fl/fl}$ mice. However, hepatocyte proliferation was significantly increased in both the pericentral and periportal zones of *Ple*$^{\Delta alb}$ mice after 14 days of CA feeding (Figure 30), which correlates with the higher hepatocellular damage observed in plectin-deficient livers (Figure 29).

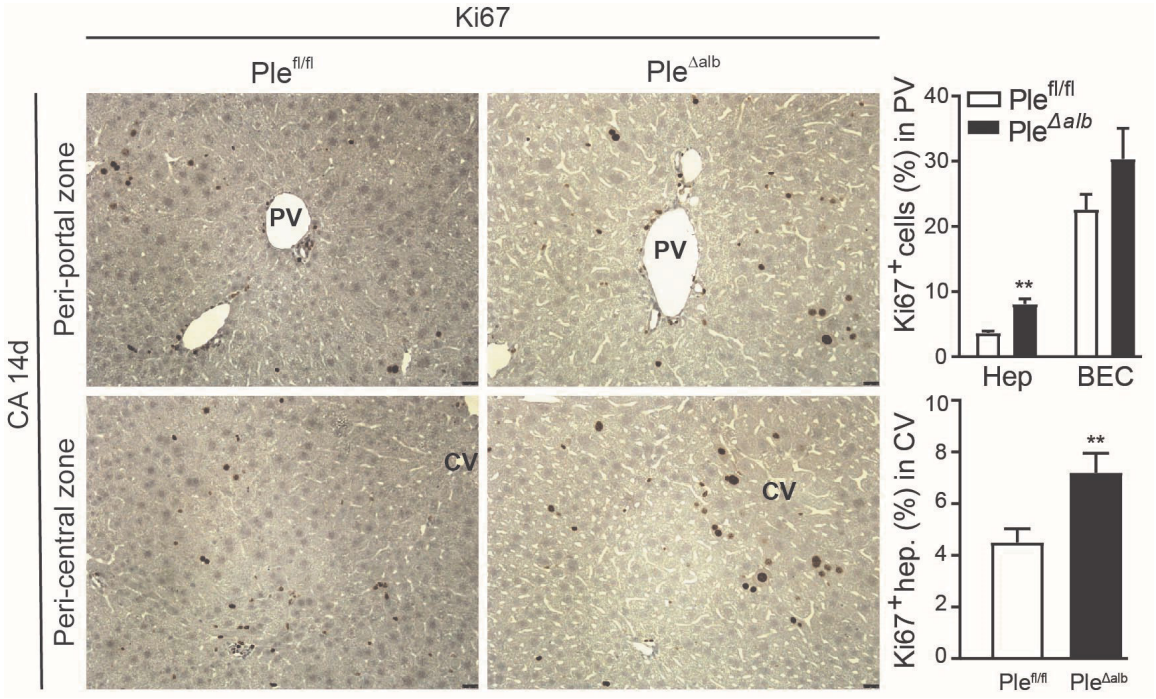

Figure 30. *Liver-specific plectin deficiency leads to enhanced hepatocyte proliferation in response to CA-induced injury*. Representative images of liver tissue of *Ple*$^{fl/fl}$ and *Ple*$^{\Delta alb}$ mice fed with the CA diet for 14 days (14d) immonulabeled for Ki67. Nuclei stained with hematoxylin (blue). Representative images show Ki67-positive (Ki67^{+}) cells in the periportal zone (portal vein; PV) and pericentral zone (central vein; CV). Scale bar, 25 µm. The bar graphs show the percentage of the Ki67^{+} cells (hepatocytes (Hep) and BECs) per field. (N = 3 animals per group). **p < 0.01 calculated using Student's t -test. Data are presented as mean + SEM.

Moreover, the ductular reaction, as assessed by $K19^+$ areas on liver sections, was significantly more pronounced in $Ple^{\Delta alb}$ mice compared to $Ple^{fl/fl}$ controls following 14 days of CA feeding (Figure 31A). In addition, A6 antigen staining revealed a two-fold increase in the progenitor cell area in $Ple^{\Delta alb}$ mice (Figure 31B). Collectively, these findings indicate that

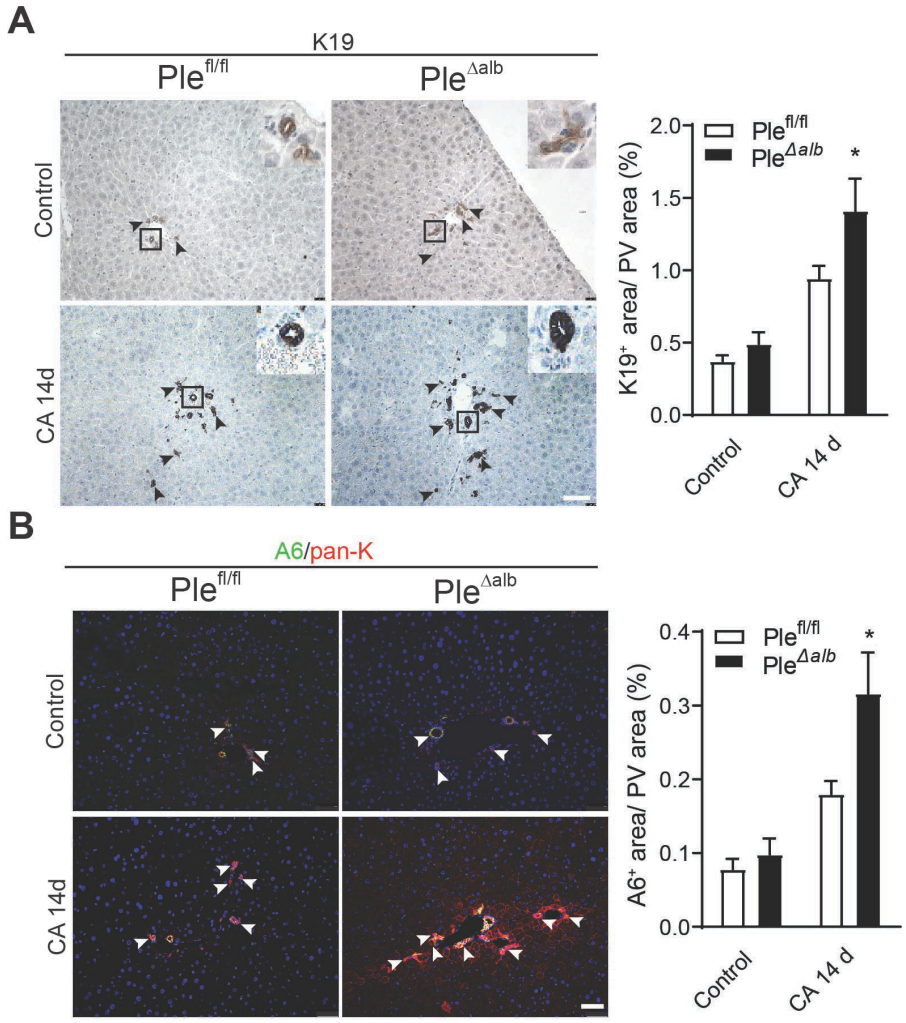

Figure 31. *Liver-specific deficiency of plectin aggravates the ductular reaction in response to CA-induced injury.* **(A)** Representative images of liver sections from $Ple^{fl/fl}$ and $Ple^{\Delta alb}$ untreated control mice and mice fed with the 0.5% CA diet for 14 days (14d) immunolabelled for K19. Boxed images show 4x magnified bile duct. Nuclei stained with hematoxylin (blue). The arrowheads indicates $K19^+$ cells Scale bar, 150 µm. The bar graph shows the percentage of $K19^+$ per poral vein (PV) area. (N = 3 animals per group). **(B)** Representative imunnofluorescence images of liver tissue immonolabellaed for A6 (green) and pan-keratin (red). Nuclei stained with DAPI (blue). Boxed images show 4x magnified bile duct.The arrowheads indicates $A6^+$ cells. Scale bar, 200 µm. The bar graph shows the percentage of the $A6^+$ area per PV area. (N = 3 animals per group). *$p < 0.05$ calculated using Student's *t*-test. Data are presented as mean + SEM.

Ple$^{\Delta alb}$ mice exhibit higher susceptibility to CA-induced injury, characterized by promounced ductular reaction and progenitor cell proliferation.

The administration of CA also resulted in an elevated bile flow rate in both genotypes compared to untreated animals. Strikingly, *Ple*$^{\Delta alb}$ mice showed a significantly faster bile flow rate than *Ple*$^{fl/fl}$ mice under CA-feeding conditions (Figure 32A), further suggesting altered bile acid transport and regulation in the absence of plectin.Additionally, the expression of bile acid transporters, including *Abcb4, Bsep,* and *Slc10a1*, was significantly upregulated in CA-treated *Ple*$^{\Delta alb}$ mice, with *Bsep* expression showing a five-fold increase compared to controls (Figure 32B). These findings were further confirmed at the protein level, with Bsep levels 1.5-times higher in *Ple*$^{\Delta alb}$ mice following CA treatment (Figure 32C).

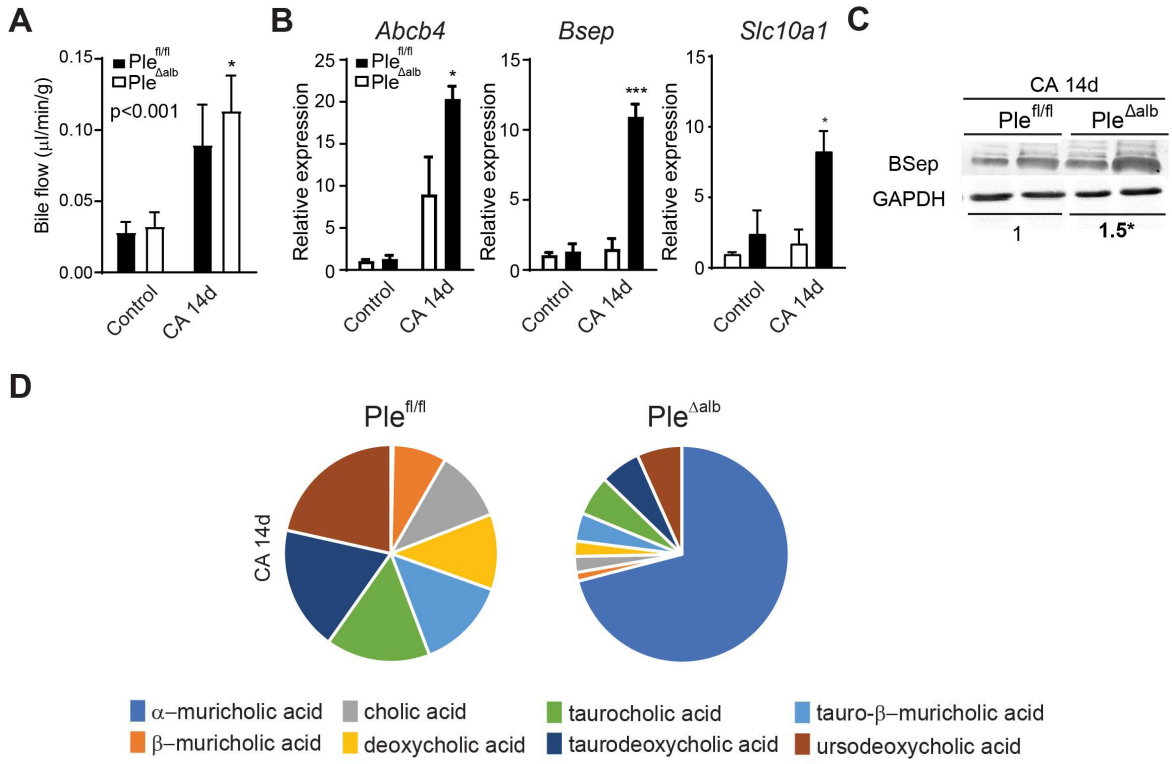

Figure 32. *CA feeding increases bile flow rate and induces changes in expression of bile acids transporters, and bile composition in Ple*$^{\Delta alb}$ *mice.* **(A)** The bar graph shows bile flow determined in *Ple*$^{fl/fl}$ and *Ple*$^{\Delta alb}$ untreated and mice fed with CA for 14days (14d) (N = 5 animals per group). **(B)** The bar graphs show relative mRNA levels of bile acid transporters. (N = 3 animals per group). Data are presented as mean + SEM. **(C)** Immunoblots of lysates prepared from mouse liver of *Ple*$^{fl/fl}$ and *Ple*$^{\Delta alb}$ mice fed with the CA for 14 days using BSEP and GAPDH antibody. GAPDH as loading control. The numbers below lines and the bar graphs indicate relative band intensities normalized to average *Ple*$^{fl/fl}$ values. (N = 3 animals per group). **(D)** The bile acid composition of *Ple*$^{fl/fl}$ and *Ple*$^{\Delta alb}$ mice untreated controls and mice fed with the CA diet for 14 days analysed using liquid chromatography-tandem mass spectrometry. (N = 5 animals per group). **(***p < 0.05, ***p < 0.001 calculated using Student's *t*-test.

Moreover, bile acid composition analysis revealed clear difference between *Ple*$^{fl/fl}$ and *Ple*$^{\Delta alb}$ mice following CA treatment. This is in contrast with comparable bile acid composition between two genotypes under basal conditions (Figure 16B). After CA feeding, *Ple*$^{\Delta alb}$ mice displayed marked increase in α-muricholic acid, cholic acid, and deoxycholic acid (Figure 32D).

4.2.4 Plectin preserves bile duct integrity under cholestatic stress

Plectin deficiency results in aberrant keratin filament organization in *Ple*$^{\Delta alb}$ BECs, leading to the collapse of ductular structures and unfavorable outcomes cholestatic injury. To further investigate how the cholestatic injury affects the bile duct morphology under BDL challenge, we performed morphometric analysis of liver sections immunolabeled for pan-K and E-cadherin that revealed clear differences between genotypes. In *Ple*$^{fl/fl}$ mice, intralobular bile ducts 14 days post-BDL were generaly round, with tightly packed BECs and a nuclear long axis perpendicular to the ductal wall (Figure 33A). In contrast, the bile ducts of *Ple*$^{\Delta alb}$ mice exhibited significantly larger luminal areas, with loosely packed and misaligned BECs that had lost their polarized orientation (Figure 33A, bar graphs). Moreover, the bile ducts of *Ple*$^{\Delta alb}$ mice under cholestatic conditions were markedly more dilated and rounder compared to untreated *Ple*$^{\Delta alb}$ livers (Figure 21), suggesting that reduced stability of the bile ducts leads to prominent dilation under increased intraluminal pressure following BDL. Furthermore, *Ple*$^{\Delta alb}$ bile ducts exhibited a greater number of ruptures (Figure 33A, arrowhead), correlating with more severe BDL-induced liver injury (Figures 24, 25, 26).

Interestingly, no comparable alterations in bile duct morphology were observed in DDC-treated animals, despite the enlargement of the bile duct lumen in *Ple*$^{\Delta alb}$ mice compared to untreated controls (Figure 33B). As BDL and DDC are both obstructive cholestasis models

leading to increased pressure within the bile ducts, the bile duct dilatation and ruptures reflect the capacity of BECs to cope with increased mechanical loading.

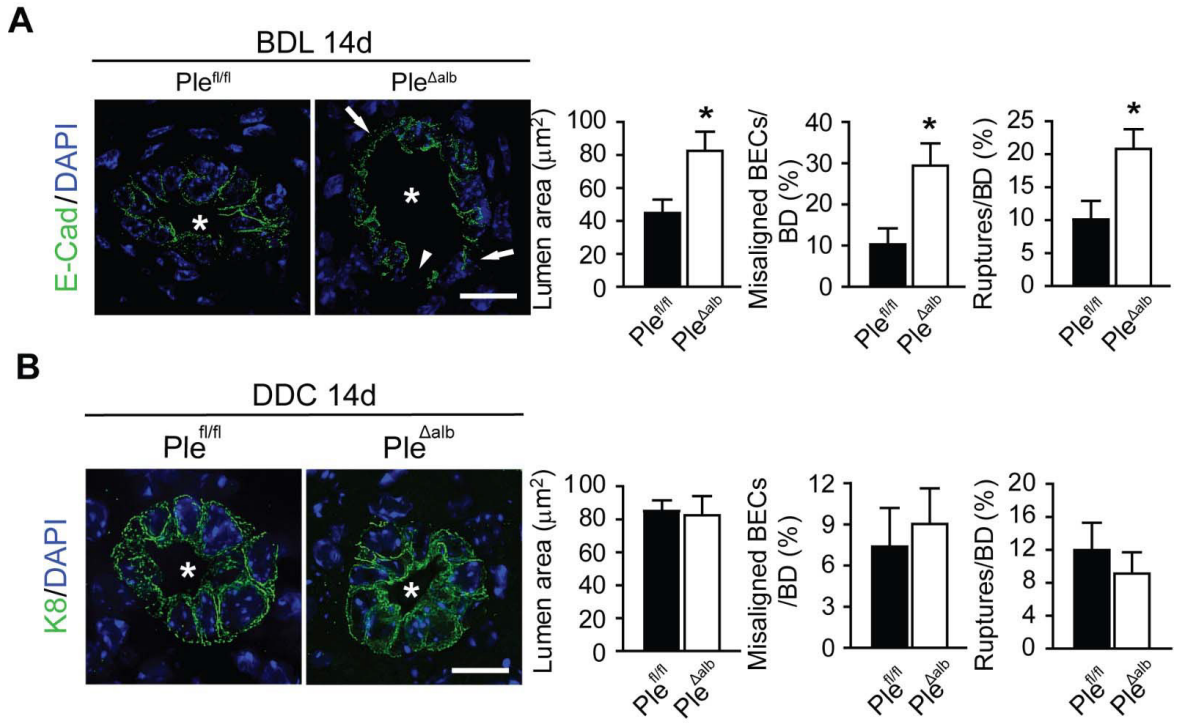

Figure 33. *Destabilisation of BEC cytoarchitecture results in cholestasis-induced biliary tree malformation.* **(A)** High-resolution microscopy images of bile duct (BD) from *Ple$^{fl/fl}$* and *Ple$^{\Delta alb}$* mice 14 days (14d) post-BDL. BDs immunolabeled for E-cadherin (E-Cad, green). Nuclei stained with DAPI (blue). The arrows indicates BEC with misaligned nucleus, the arrowhead points to BD rupture, and the asterisks mark biliary lumen. Scale bar, 10 µm.The bar graphs show statistical evaluation of morphometric analysis of BD. The cross-sectional luminal area, the number of misaligned cells (cells losing their polarized shape with the nuclear long axis perpendicular to the ductal wall) and the number of ruptures. (N = 2 animals per group, >10 BDs). **(B)** High-resolution microscopy images of BDs from *Ple$^{fl/fl}$* and *Ple$^{\Delta alb}$* mice fed with DDC for 14 days. BDs immunolabeled for K8 (green). Nuclei stained with DAPI (blue). The asteriks mark biliary lumen. Scale bar, 10 µm. The bar graphs show statistical evaluation of morphometric analysis of BD. The cross-sectional luminal area, the number of misaligned cells (cells losing their polarized shape with the nuclear long axis perpendicular to the ductal wall) and the number of ruptures. (N = 3 animals per group, >10 BDs). *$p < 0.05$ calculated using Student's *t*-test. Data are presented as mean + SEM.

In contrast to obstructive models of cholestasis, the CA-feedingt model represents metabolic cholestasis, primarily affecting bile acid transport and composition rather than mechanical obstruction. Hence, while BDL and DDC lead to mechanical stress and bile duct rupture, CA-induced cholestasis does not cause the same degree of ductal malformation.

Since junctional complexes are crucial to maintaining BECs cohesion, we compared the morphology of tight junctions, adherens junctions, and desmosomes in unchallenged *Ple$^{\Delta alb}$* and *Ple$^{fl/fl}$* mice using transmission electron microscopy (TEM). Quantitative analysis revealed a significant reduction in tight junction length in *Ple$^{\Delta alb}$* livers, while no differences were noted

in the morphology of adherens junctions and desmosomes (Figure 34A). Immonoblot analysis of desmosomal protein expression revealed comparable levels of desmoplakin between untreated *Ple*$^{\Delta alb}$ and *Ple*$^{fl/fl}$ liver lysates. However, *Ple*$^{\Delta alb}$ lysates showed a 50% increase in E-cadherin levels (Figure 33B), despite no obvious changes in morphology of adherens junctions were observed (Figure 34A). To understand whether plectin deficiency affects junctional protein expression under cholestatic stress, we evaluated the levels of these proteins in livers of BDL- and CA-challenged *Ple*$^{\Delta alb}$ and *Ple*$^{fl/fl}$ mice.

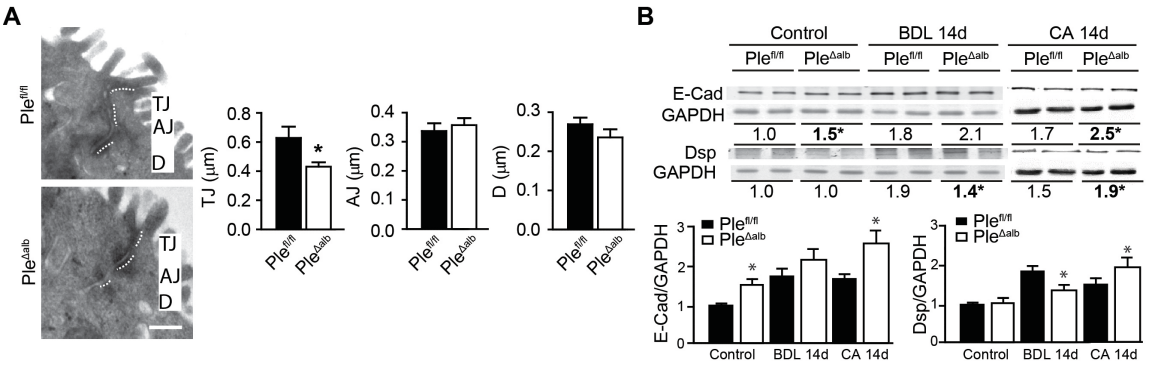

Figure 34. *Plectin depletion disrupts cytoarchitecture and alters expression levels of cell-cell junction components.* **(A)** Representative TEM micrographs of bile duct junctional complexes from untreated *Ple*$^{fl/fl}$ and *Ple*$^{\Delta alb}$ mice. Drawn bars (white) indicate tight junctions (TJs), adherens junctions (AJs), and desmosomes (Ds). Scale bar, 1.5 µm. Bar graphs show a statistical evaluation of junctional complex length measurement. (N = 2 animals per group, 2 - 3 bile ducts). **(B)** Immunoblots of liver lysates prepared from control, 14 days (14d) post-BDL or mice fed with CA diet for 14 days using antibodies to E-Cadherin (E-Cad) and desmoplakin (Dsp). GAPDH, as loading control. The numbers below lines and the bar graphs show relative band intensities normalized to average sham *Ple*$^{fl/fl}$ values. (N = 3 - 4 animals per group). *$p < 0.05$ calculated using Student's *t*-test. Data are presented as mean + SEM.

Both treatments caused a general dysregulation of junctional proteins. In particular, *Ple*$^{\Delta alb}$ mice showed significant increase in E-cadherin and desmoglein expression in response to CA treatment compared to controls (Figure 34B). In contrast, BDL resulted in a less pronounced upregulation of desmoplakin in *Ple*$^{\Delta alb}$ mice compared to *Ple*$^{fl/fl}$ mice (Figure 34B). These findings suggest that plectin deficiency affects composition of cell-cell contacts, rendering the ducts more susceptible to rupture and dilation under obstructive cholestatic stress.

4.2.5 Plectin is required in cholestasis-induced adaptive remodeling of interlobular bile ducts

To gain deeper insights into the mechanisms underlying ductular adaptation, we employed 3D confocal imaging and surface reconstructions, with automated image quantification of 80-µm-thick liver sections immunolabelled for K19 (Vartak et al. 2016). This

approach enabled precise visualization of bile duct morphology, revealing clearly discernible differences between $Ple^{\Delta alb}$ and $Ple^{fl/fl}$ mice under both normal and cholestatic conditions.

Dilation of the bile ducts represents an adaptive response to increased intraluminal pressure as the biliary tree attempts to accommodate increased bile secretion. In $Ple^{\Delta alb}$ mice, a higher prevalence of dilated bile ducts was observed under basal conditions (Figure 35), which supports our 2D histological findings (Figure 20). This dilation was significantly exacerbated following BDL-induced injury, in $Ple^{\Delta alb}$ mice showing more pronounced ductal enlargement compared to $Ple^{fl/fl}$. In contrast, DDC feeding led to only mild ductular dilation, with no significant differences observed between the $Ple^{fl/fl}$ and $Ple^{fl/fl}$ genotypes (Figure 35). Interestingly, CA-treated mice did exhibit almost no differences in bile duct diameter compared to untreated animals, suggesting that CA-induced cholestasis affects the biliary tree through mechanisms unrelated to pressure-induced ductal enlargement. However, plectin deficient bile ducts were significantly enlarged. Notably, differences between genotypes in ductular dilation were apparent in both the BDL and CA models, while no significant changes were observed in the DDC model.

Quantitative analysis revealed a significant increase in ductular surface area per field in BDL- and DDC-treated livers compared to untreated controls in $Ple^{fl/fl}$ (Figure 35), indicating a volumetric expansion as an adaptive response of the biliary tree. Interestingly, analysis of $Ple^{\Delta alb}$ mice revealed a remarkably different phenotype. Even under physiological conditions, ductular surface area was already elevated, and BDL further aggravated this dilation. In contrast, DDC treatment had minimal effect on the ductular area in $Ple^{\Delta alb}$ mice, with values similar to untreated controls. Also, the CA model did not induce significant changes in ductular surface area in either genotype compared to untreated livers, supporting the notion that CA-induced cholestasis is not associated with mechanical stress.

The most prominent morphological adaptation observed in $Ple^{\Delta alb}$ mice is the significant increase in ductal corrugation (Figure 35). Defined by the degree of surface elevation along the ductular length, corrugation was more pronounced in $Ple^{\Delta alb}$ mice under all cholestatic conditions, including BDL, DDC, and CA treatments, as well as in untreated controls. While DDC did not result in statistically significant differences, a clear trend toward increased corrugation was still present. This enhanced corrugation presumably represents a compensatory mechanism, increasing the total luminal surface area available for secretion of bile, thereby mitigating the adverse effects of cholestatic injury induced by BDL, DDC, and

CA treatments (Figure 35). The increase in ductal corrugation enhances absorptive capacity within the bile ducts, helping to reduce the risk of rupture or obstruction. Strikingly, in mechanically unstable plectin-deficient BECs, this adaptive response becomes exaggerated, reflecting increased susceptibility to cholestatic stress. CA-fed $Ple^{\Delta alb}$ mice exhibited the most pronounced alterations in ductal morphology, indicating severe changes in bile duct architecture in response to CA-induced cholestasis. These results suggest that $Ple^{\Delta alb}$ mice are more vulnerable to BDL- and CA-induced injury, leads to extensive remodeling of the biliary tree in an effort to optimize the intraluminal surface area and accommodate enhanced bile flow through structural adaptation.

In contrast, DDC exposure resulted in less prominent ductal adaptation of $Ple^{\Delta alb}$ mice. This highlights the model-specific nature of bile duct remodeling, where the obstructive cholestasis seen in BDL and DDC models induces greater mechanical and structural changes compared to the CA model, reflecting thus different pathogenic mechanisms.

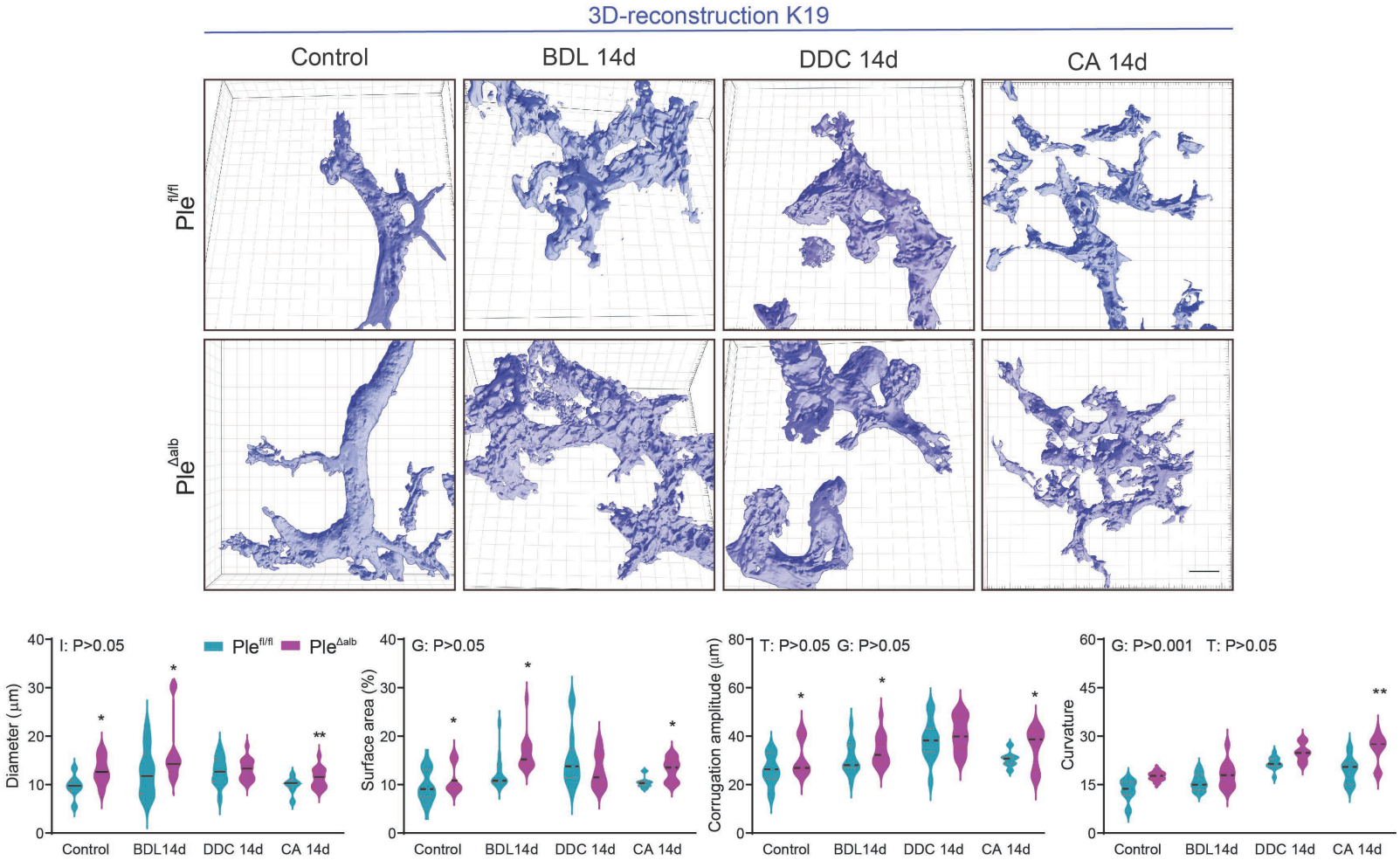

Figure 35. *Plectin facilates cholestasis-induced adaptive remodeling of interlobular bile dutcs.* The 3D reconstruction of bile ducts reveals fundamental changes in the biliary tree network remodeling upon challange in three cholestatic mouse models (BDL, DDC, and CA model for 14 days (14d)). Representative bile ducts isolated from 3D surface reconstructions of the biliary surface of K19-imminolabeleded of 80-µm-thick liver sections from untreated and challenged $Ple^{fl/fl}$ and $Ple^{\Delta alb}$ mice. Scale bar, 30 µm. The violin graphs show quantification spatial geometry of bile duct, diameter, percentage of $K19^{+}$ surface area, corrugation amplitude (average elevation of surface from normal vector magnitudes), and curvature. Median is indicated by line, dashed line 25 - 75th percentiles. (N = 3 animals per group, 10 bile ducts). *p*-value calculated using two-way ANOVA, indicating genetic (G) effect, effect of treatment (T) and their interaction (I) with post-*t*est (Bonferroni *$p < 0.05$).

4.2.6 Plectin facilitates an adaptive cellular response to cholestatic stress in hepatic canaliculi

Recent findings have highlighted plectin's pivotal role in mediating the cellular response to mechanical stress in epithelial cells (Prechova et al. 2022; Krausova et al. 2021). Consistent with these observations, we have shown that the cholestatic environment induced an elevation of plectin expression at the apical membrane of the bile canaliculi (Figure 36). This increase was particularly evident in 3D collagen sandwich cultures of primary mouse hepatocytes upon treatment with deoxycholic acid (DCA) for 16 hours (control, DMSO; Figure 36). These findings indicate that plectin may serve as a protective structural component during cholestatic stress by reinforcing the bile canalicular structures.

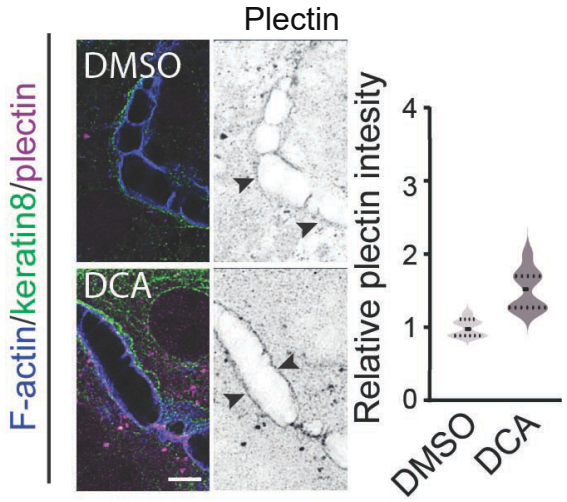

Figure 36. *Plectin intensity levels are elevated along bile canaliculi during cholestasis.* Representative confocal overlay images of primary mouse hepatocytes treated with 200 µM deoxycholic acid (DCA) for 16 hours and untreated control (DMSO) labeled for F-actin (blue), K8 (green), and plectin (magenta). Left images represents plectin-immolabeled bile canaliculi. The violin graph shows plectin fluorescence intensity levels on bile canalicular apical domain (visualised by F-actin) (N = 1 biological replicate).

To further explore the role of plectin in maintaining bile canalicular integrity, we examined bile canalicular width as an adaptive readout in response to BDL over three time points (1 , 5, and 14 days) post-BDL, investigating thus the transition from acute to chronic cholestatic injury.

Quantitative analysis of bile canaliculi along the CV to PV axis revealed a significant increase in bile canalicular width across all three liver zones: peri-central, mid-lobular, and peri-portalin $Ple^{\Delta alb}$ mice compared to controls at all time points post-BDL (Figure 37). This expansion in canalicular width is an initial compensatory mechanism to accommodate the increased bile pressure resulting from cholestasis. The bile canaliculi dilate to optimize bile flow and to cope with cholestataic stress; interestingly canalicular dilation was more pronounced in $Ple^{\Delta alb}$ compare to $Ple^{fl/fl}$ mice, indicating a reduced ability to cope with bile pressure in the absence of plectin.

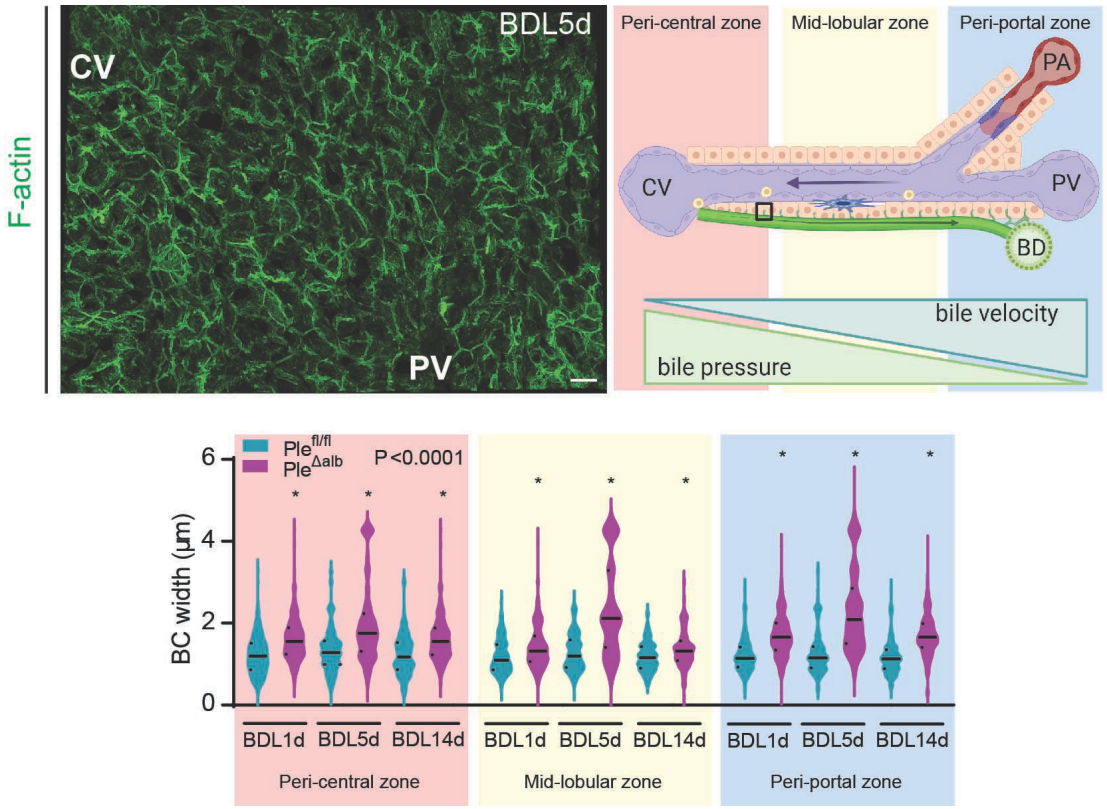

Figure 37. The role of *plectin in maintaining bile canalicular integrity across liver zones.* Representative image (left) of liver tissue from mouse 5 days (5d) post- BDL labeled for F-actin (green). Central vein (CV) and portal vein (PV) are indicated. Scale bar, 30 µm. Scheme of liver zonation (right). The blood flows from PV to CV which results in gradients formed along the sinusoid. The gradients of bile pressure and bile velocity are indicated. The violin graphs demonstrate the relationship between canalicular width and its spatial-temporal dependence. The median is indicated by line, 25 - 75th percentiles are indicated by dashed line. Individual liver zones are marked on the graph in accordance with the specified scheme (peri-central, pink; mid-lobular, yellow; and peri-portal, blue). N = 3 animals per group; *p*-value calculated using two-way ANOVA, with post-test (Bonferroni *$p < 0.05$).

To assess the vulnerability of the bile canalicular network in plectin-deficient mice, we utilized BDL over three time points (1, 5, and 14 days) post-BDL, representing the transition from acute to chronic cholestatic injury.

The widening of bile represents initial step in adaptation to bile duct obstruction. Plectin-deficiency leads to failure of this adaptation resulting in pathological consequences seen as canalicular blebbing and ruptures. Blebbing corresponds areas where the plasma membrane detaches from the underlying actin cytoskeleton due to excessive bile pressure, resulting in balloon-like protrusions (Figure 38, pink arrowheads). We observed a significant increase in bile canalicular blebbing in *Ple*$^{\Delta alb}$ mice compared to *Ple*$^{fl/fl}$ controls at all time points analyzed (Figure 38). This phenomenon underscores the mechanical fragility of the canalicular walls in *Ple*$^{\Delta alb}$ mice.

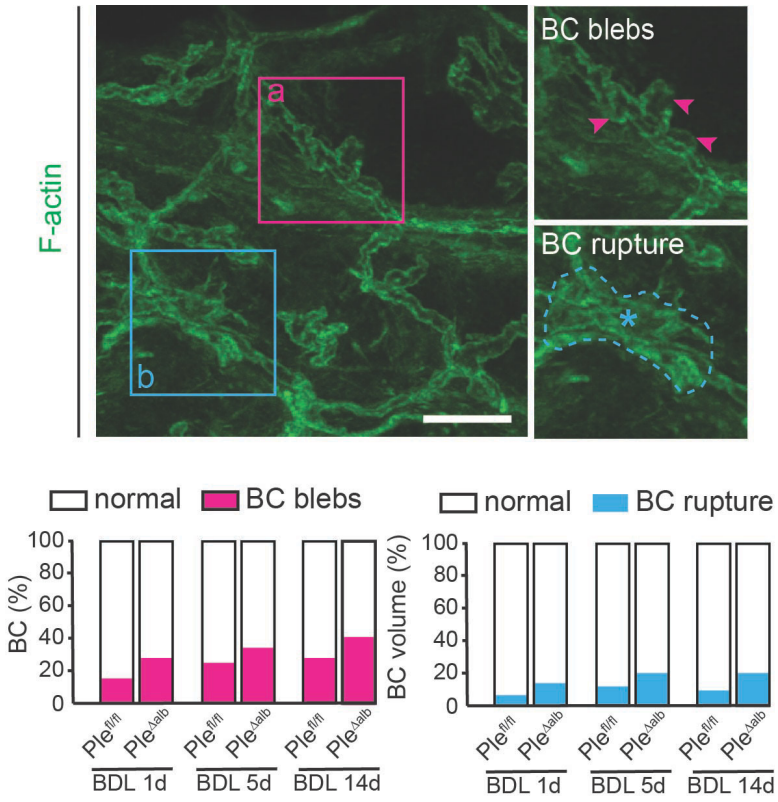

Figure 38. *Bile canalicular blebbing and ruptures as indicators of cholestatic stress in Ple*$^{fl/fl}$ *and Ple*$^{\Delta alb}$ *mice.* Representative high-resolution image of liver tissue of mouse 1 day (1d) post-BDL labeled for F-actin (green) to depict two features of bile canaliculi (BC) as result of cholestatic stress, BC blebs (a) pink square and 2x magnified image (individual blebs are marked by pink arrowheads) and BC rupture (b) blue square and 2x magnified image (rupture is marked by blue dashed-line, BC rupture lumen is indicated by asterix). Scale bar, 10 µm. The part-to-whole charts show the percentage of BC having blebs and percentage BC volume representing ruptured lumen over time of exposure of cholestatic insult (1d, 5d, and 14d). (N = 3 animals per group).

In addition to blebbing, bile canalicular ruptures were more frequently observed in $Ple^{\Delta alb}$ mice. These ruptures, distinguishible as the breakdown of the canalicular wall, were seen at all BDL time points. In addition, the extent of ruptures was significantly larger compared to $Ple^{fl/fl}$ (Figure 38, blue dashed lines and asterisks). The ruptures result in bile leakage into the surrounding parenchyma, where bile exacerebrates liver damage and inflammation.

For a better understanding of the spatial-temporal dynamics of the adaptive response to cholestatic stress, we utilized 3D confocal imaging, and surface reconstructions, with automated image quantification of 80-µm-thick liver sections. This approach involved immunostaining for the apical membrane marker DPP4 to visualize and analyze the structural changes of bile canaliculi. These analyses allowed us to visualize and quantify the complex architectural changes occurring in bile canaliculi under cholestatic conditions, both in $Ple^{fl/fl}$ and $Ple^{\Delta alb}$ mice in periportal zone. The 3D reconstructions revealed substantial morphological alterations in the bile canalicular network under cholestatic conditions, with obvious differences between $Ple^{fl/fl}$ and $Ple^{\Delta alb}$ mice (Figure 39). When unchallenged, $Ple^{\Delta alb}$ mice showed abberant canalicular network, with increased canalicular volume, diameter, angular variation, canalicular length, and higher curvature compared to untreated $Ple^{fl/fl}$ mice.

In $Ple^{fl/fl}$ mice, all three cholestatic models induced significant changes in bile canalicular morphology, including increases in volume, diameter, length, corrugation amplitude, tortuosity, and angular variation. Interestingly, BDL treatment led to a decrease in angular variation in $Ple^{fl/fl}$ mice, while other parameters associated with canalicular network complexity were consistently elevated. This mirrors the alterations observed in the bile ducts, demonstrating a coordinated morphological response to cholestatic stress.

In contrast to $Ple^{fl/fl}$ mice, $Ple^{\Delta alb}$ mice parameters such as bile canalicular volume, diameter and length were elevated compared to untreated $Ple^{\Delta alb}$ livers, reflecting an adaptive expansion of the canalicular network. Strikingly, crutial morphological adaptations, including angular variation and corrugation amplitude, were notably diminished in $Ple^{\Delta alb}$ mice, emphasizing reduced capacity to respond to cholestasis. Interestingly, canalicular tortuosity remained elevated, indicating that compensatory mechanisms remained preserved upon plectin inactivation. A particularly intriguing finding was the increase in eccentricity of the bile canalicular network under cholestatic conditions in $Ple^{\Delta alb}$ mice, a change that has not been observed in $Ple^{fl/fl}$ mice. This suggests that plectin deficiency alters the structural adaptation of

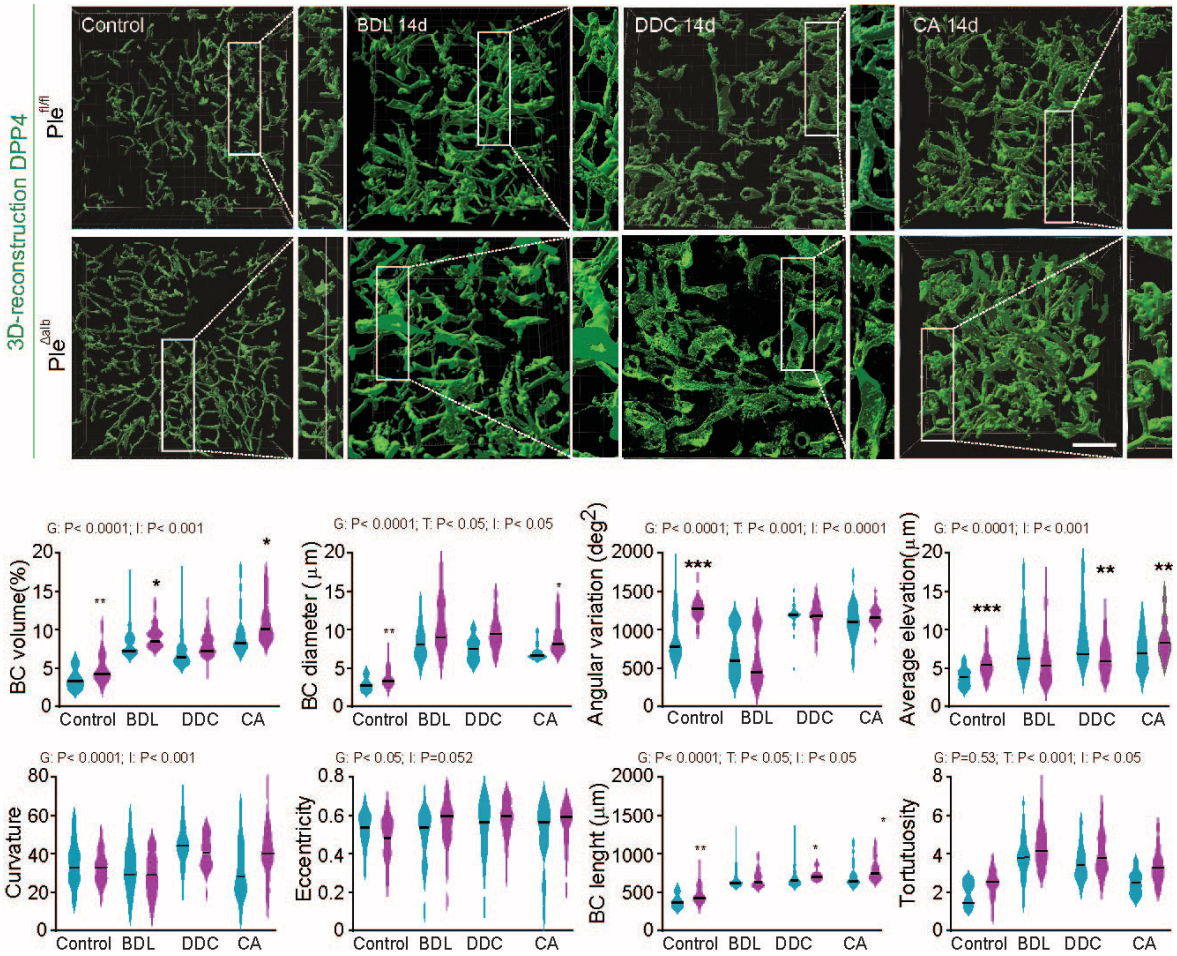

Figure 39. *Aberrant organization of the plectin-deficient parenchymal cytoskeleton is associated with pronounced remodeling of the canalicular network in cholestasis*. Representative 3D surface reconstructions of the bile canalicular surface from DPP4-immonolabeled 80-µm-thick liver sections from *Ple$^{fl/fl}$* and *Ple$^{\Delta alb}$* mice untreated and challenged in three cholestatic mouse ((BDL, DDC, and CA model for 14 days (14d)). Scale bar, 30 µm. The violin graphs show results of spatial geometry analysis of canalicular network, percentage of DPP4^{+}volume, quantification of bile canalicular (BC) diameter; angular variation and angular elevation as parameters of corrugation (average variation and elevation of surface from normal vector magnitudes); curvature; eccentricity; BC length and tortuosity. The median is indicated by line, 25 - 75th percentiles are indicated by dashed line. (N = 3 animals per genotype, 10 periportal fields). *p*-value calculated using two-way ANOVA, indicating genetic effect (G), effect of treatment (T), and their interaction (I), with post-test (Bonferroni *$p < 0.05$; **$p < 0.01$; ***$p < 0.001$).

liver to cholestatic injury, specifically affecting the spatial organization and flexibility of the canalicular network. In contrast, eccentricity remained unchanged in $Ple^{fl/fl}$ mice across all treatments, further highlighting the distinct morphological responses between the two genotypes.

Increased bile pressure due to cholestasis induces the formation of load-bearing structures known as apical bulkheads, which are visualized as F-actin-positive membrane protrusions spanning the lumen of bile canaliculi. To investigate whether elevated intraluminal pressure impacts apical bulkhead formation in a plectin-deficient liver, we employed the BDL model, analyzing liver tissue at 1, 5, and 14 days post-surgery. High-resolution imaging revealed a significant reduction in the number of apical bulkheads in $Ple^{\Delta alb}$ mice compared to $Ple^{fl/fl}$ controls, evident at all time points post-BDL. This reduction was consistent across all zones (peri-central, mid-lobular, and peri-portal) (Figure 40). The decreased presence of apical bulkheads in $Ple^{\Delta alb}$ mice was associated with dilated bile canaliculi and propably contributes to recuced mechanical resilience of bile canaliculi upon cholestatic stress.

In addition to structural changes in the bile canaliculi, $Ple^{\Delta alb}$ mice displayed increased sensitivity to bile acids, as evidenced by higher levels of necrosis (Figure 25 and 29). Under cholestatic conditions, particularly with CA feeding and BDL-induced cholestasis, $Ple^{\Delta alb}$ mice exhibited a greater degree of hepatocellular necrosis than their $Ple^{fl/fl}$ littermates, indicating that plectin deficiency exacerbates cell death in response to bile acid stress. This finding further underscores the protective role of plectin in liver homeostasis under conditions of bile acid accumulation. Morphometric analysis revealed that $Ple^{\Delta alb}$ hepatocytes were more susceptible to bile acid-induced necrosis and bile canalicular dilation (Figure 41A). These observations

suggest that the absence of plectin compromises the resilience of hepatocytes, fostering increased susceptibility to bile acid-induced toxicity.

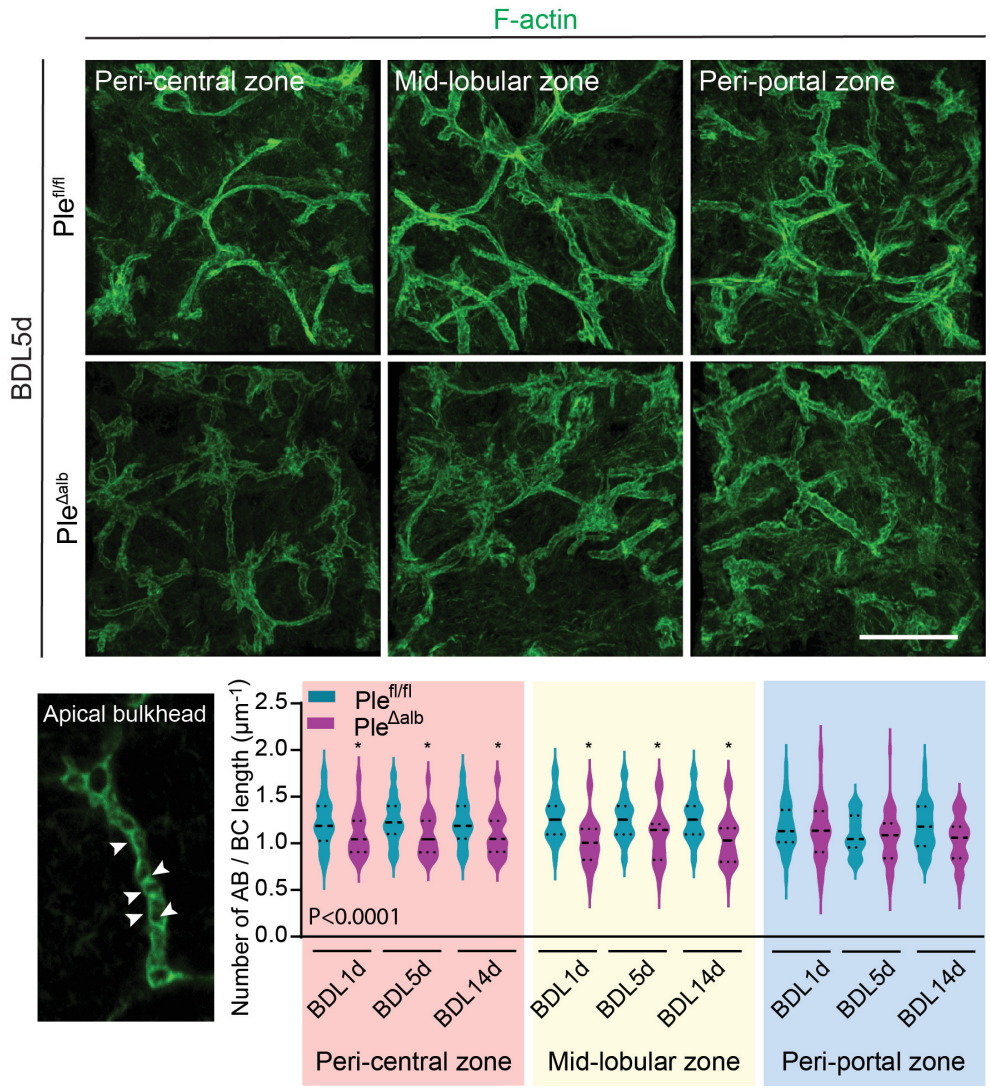

Figure 40. *Plectin plays a role in capacity of hepatocytes to withstand elevated pressure under cholestasis.* **(A)** Representative high-resolution images of liver tissue from *Ple$^{fl/fl}$* and *Ple$^{\Delta alb}$* mice 5 days (5d) post-BDL labelled for F-actin (green). Scale bar, 10 µm. High-resolution image of individual bile canalicullus with indicated apical bulkheads (AB, white arrowheads). The violin graphs show number of apical bulkheads per bile canaliculus 1d, 5d, and 14d post-BDL in different liver zones. The median is indicated by black line, 25 - 75th percentiles are indicated by dashed line. Individual liver zones are marked (peri-central, pink; mid-lobular, yellow; peri-portal, blue). (N = 3 animals per group), *p*-value calculated using two-way ANOVA, with post-test (Bonferroni *$p < 0.05$).

To directly test the effect of increased intraluminal pressure on the bile canaliculi, we used 3D collagen sandwich culture of primary *Ple*$^{fl/fl}$ and *Ple*$^{\Delta alb}$ hepatocytes and treated them with DCA. Morphometric analysis revealed significantly larger bile canaliculi in *Ple*$^{\Delta alb}$

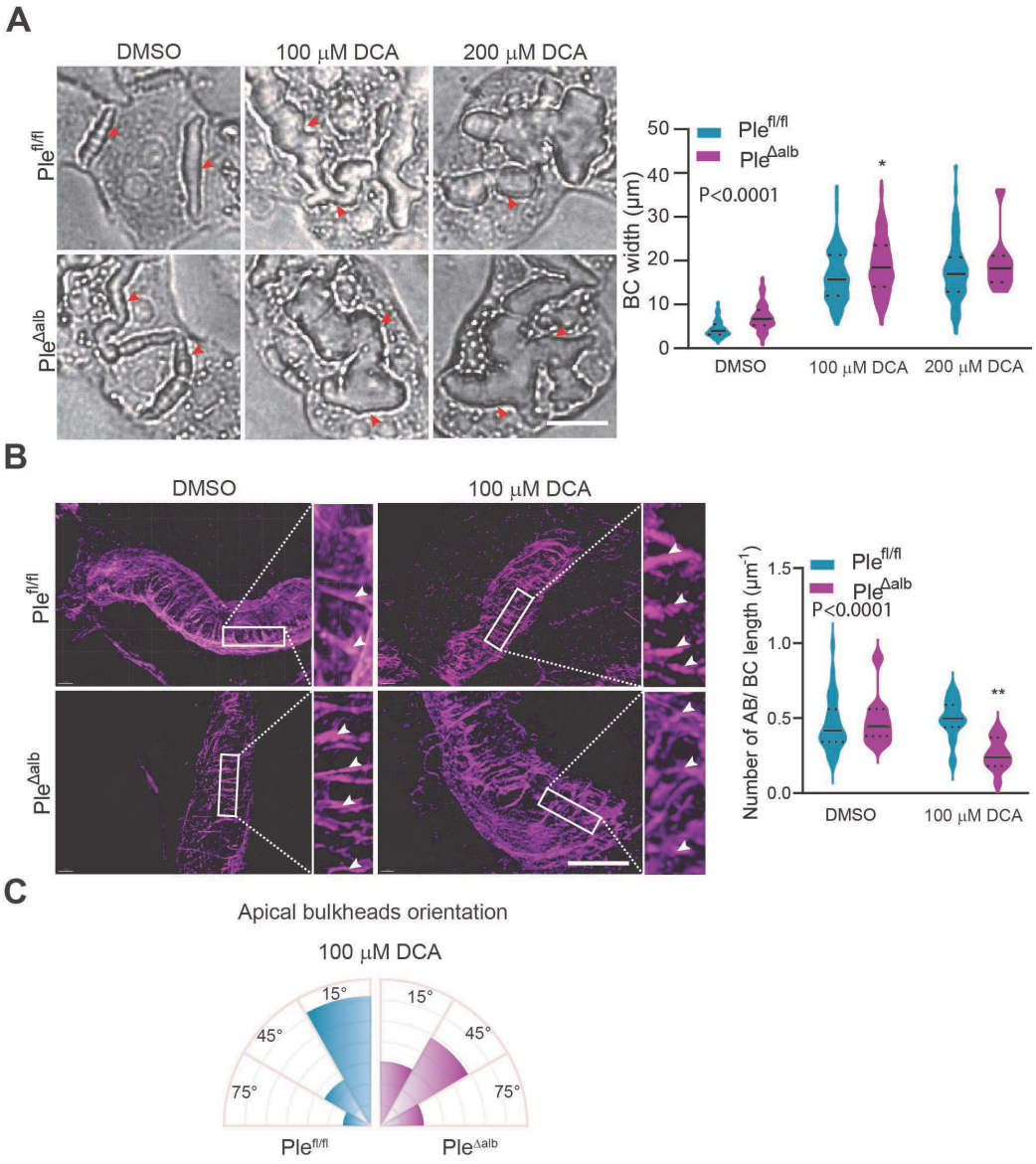

Figure 41. *Plectin fosters mechanical resilence of hepatocytes upon cholestatic stress.* **(A)** Different responses of the bile canaliculi towards increased pressure. Representative images of 3D collagen culure of primary hepatocytes isolated from *Ple*$^{fl/fl}$ and *Ple*$^{\Delta alb}$ mice either untreated (DMSO) or treated with 100 µM and 200 µM DCA for 16 hours. Red arrowhead indicate apical bulkheads (AB). Scale bar, 10 µm. The violin graph shows the width of bile canaliculi (BC). The median is indicated by line. 25 - 75th percentiles are indicated by dashed line. (N = 2 biological replicates). **(B)** Representative high-resolutin images of 3D collagen culure of primary hepatocytes treated with DMSO (control) or 100 µM DCA for 16 hours labeled for F-actin (magenta). Boxed areas 10x magnified images of bile camaliculi. Arrowheads indicate apical bulkheads. The violin graph show the number of apical bulkheads per length of bile camaliculus. The median is indicated by line, 25 - 75th percentiles are indicated by dashed line. **(C)** Rose diagram shows the orientation of apical bulkheads towards bile canaliculus in DCA-treated cells. Apical bulkheads perpendicular to bile canalicular axis has angle 0°. Data are shown as percentage, individual line within the diagram represents 14 %. (N = 2 biological replicates). *p*-value calculated using two-way ANOVA, with post-test (Bonferroni **p* < 0.05; ***p* < 0.01).

compared to *Ple*$^{fl/fl}$ hepatocytes (Figure 41A). Interestingly, primary hepatocytes isolated from *Ple*$^{\Delta alb}$ mice were more sensitive to DCA treatment, as we observed more dead cells at higher concentrations of DCA, though the used DCA concentration was within the range of total bile acids accumulating in the serum of mice after BDL. The number of apical bulkheads per bile canaliculus was significantly reduced in *Ple*$^{\Delta alb}$ hepatocytes, indicating that plectin deficiency compromises bile canalicular integrity (Figure 41B). Additionally, morphological analysis of apical bulkheads revealed altered orientation in *Ple*$^{\Delta alb}$ hepatocytes, as visualized in the rose diagram (Figure 41C). In *Ple*$^{fl/fl}$ hepatocytes, apical bulkheads were predominantly aligned perpendicular to the bile canaliculus axis, with most falling within a narrow range of 0°-30°. In contrast, *Ple*$^{\Delta alb}$ hepatocytes exhibited a more disorganized and variable orientation, with a significant proportion of apical bulkheads positioned within a broader angle range of 30°- 60°. This misalignment further underscores the critical role of plectin in maintaining the proper organization of apical bulkheads, which are essential for preserving bile canalicular structure and resilience under cholestatic stress.

4.2.7 Plectin stabilizes keratin filaments under stress and affects the p38 MAP kinase signaling pathway in liver epithelial cells

Previous studies have established a connection between resilience to cholestatic injury and the stability of the keratin filament network. Given the alterations in keratin filaments organization observed in *Ple*$^{\Delta alb}$ livers, we investigated keratin filament reorganization in response to stress conditions in liver epithelial cells. Immunofluorescence microscopy for K8 on liver sections 5 and 14 days post-BDL confirmed an increase in the density of the keratin filament network, as previously reported. Additionally, single hepatocytes with K8-positive ($K8^+$) aggregates were found to be 1.5-times more prevalent in *Ple*$^{\Delta alb}$ livers compared to *Ple*$^{fl/fl}$ livers (Figure 42A).

To validate the role of plectin in stress-induced keratin filament reorganization *in vitro*, we induce hyperphosphorylation primary hepatocytes seeded on collagen-coated coverslips using the phosphatase inhibitor okadaic acid (OA). Untreated *Ple*$^{\Delta alb}$ hepatocytes displayed a less organized and bundled keratin filament network compared to *Ple*$^{fl/fl}$ hepatocytes. This was reminiscent to immoflurescence images of liver parenchyme (Figure 16). After OA treatment, keratin filaments in *Ple*$^{\Delta alb}$ cells exhibited an increased propensity to collapse when compared

to *Ple*$^{fl/fl}$ hepatocytes. The filaments not only formed thicker, disorganized bundles in the cytoplasm but also showed extensive areas of collapse into aggregates (Figure 42B).

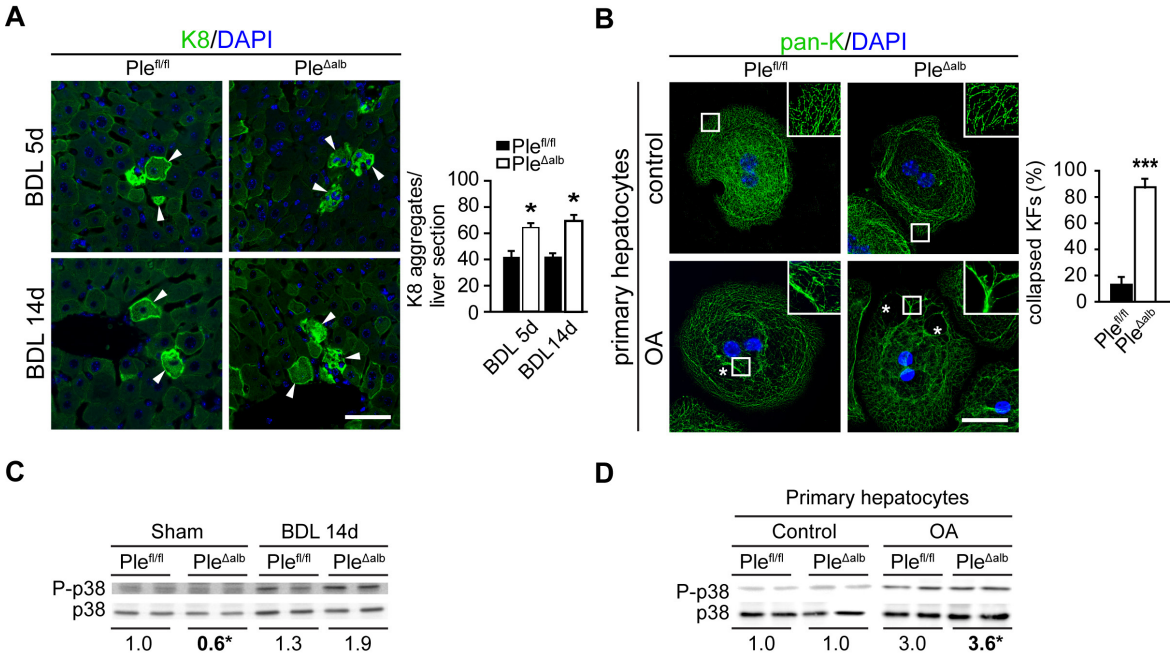

Figure 42. *Plectin deficiency leads to increased keratin filaments collapse and aberrant stress signaling in liver epithelial cells*. **(A)** Representative images of liver tissue from *Ple*$^{fl/fl}$ and *Ple*$^{\Delta alb}$ mice 5 and 14 days (5d and 14d) post-BDL immunolabelled for K8 (green). Nuclei were stained with DAPI (blue). The arrowheads indicate K8 aggregates. Scale bar, 25 µm. The bar graph shows the number of hepatocytes with K8 aggregates per liver section. (N = 3 animals per group). **(B)** Representative images of primary hepatocytes isolated from *Ple*$^{fl/fl}$ and *Ple*$^{\Delta alb}$ mice cultivated on collagen-coated coverslips untreated (control), or incubated with 30 nM okadaic acid (OA) for 1 hour and immunolabelled for pan-keratin (pan-K, green). Nuclei were stained with DAPI (blue). The asterisks, areas devoid of keratin staining. Scale bar, 10 µm. Boxed images show 3x magnified images. The bar graphs show the percentage of cells with collapsed keratin filaments. (N = 3 biological replicates). Data are presented as mean + SEM. **(C-D)** Immunoblots of lysates prepared from mouse livers isolated from *Ple*$^{fl/fl}$ and *Ple*$^{\Delta alb}$ mice sham operated mice and from mice 14 days post-BDL (C), or untreated and OA-treated primary hepatocytes cultivated on collagen coated dish (D) shown in A and B using anti-p38, and anti-phospho-p38 (P-p38) antibodies. The numbers below lines indicate relative band intensities normalized to average control values. (N = 3 - 4 animals per group). *$p < 0.05$, ***$p < 0.001$ calculated using Student's *t*-test.

The increased stress-induced activation of p38 kinase correlated with the increased fragility of the keratin filament networks in plectin-deficient liver epithelial cells, underscoring the critical role of plectin in maintaining keratin filament stability under stress conditions. Keratin filament reorganization is mediated by the MAP kinase p38 (Menon et al. 2010), a stress-response kinase that has been implicated in the pathogenesis of cholestatic liver disease. Previous studies have suggested that plectin plays a regulatory role in modulating the p38 signaling pathway, particularly under conditions of cellular stress (Osmanagic-Myers et al. 2006). To determine whether changes in the appearance of keratin filaments following BDL-

or OA-treatment were associated with p38 activation, we utilized anti-phospho-p38 antibodies to evaluate phosphorylation levels, a hallmark of p38 activation.

Our analysis revealed significantly lower baseline p38 activity in liver lysates from sham-operated $Ple^{\Delta alb}$ mice compared to $Ple^{fl/fl}$ controls, indicating that plectin-deficient livers exhibit reduced p38 signaling under normal conditions. Interestingly, this downregulation was not observed *in vitro*, as basal phosphorylation levels of p38 kinase were similar between plectin-deficient hepatocytes and those isolated from $Ple^{fl/fl}$ mice. This suggests that the regulatory effects of plectin on p38 activation may be more pronounced in the liver's *in vivo* environment, where mechanical stress and bile flow exert additional pressures that are not fully replicated *in vitro*.

Futhermore, upon exposure to cholestatic stress induced by BDL-challenge, p38 activation was significantly higher in $Ple^{\Delta alb}$ livers compared to their wild-type littermates, despite the lower levels in the sham condition (Figure 42C). This hyperactivation of p38 post-BDL suggests that in the absence of plectin, the liver's ability to modulate stress response pathways is significantly impaired, leading to an enhanced activation of p38 as a compensatory mechanism.

Similarly, when hepatocytes were treated with OA, we observed elevated p38 phosphorylation in plectin-deficient cells relative to those from $Ple^{fl/fl}$ mice (Figure 42D). The increased activation of p38 in response to stress correlated with the increased fragility of the keratin filament networks in $Ple^{\Delta alb}$ liver epithelial cells, further supporting the notion that plectin is critical for maintaining keratin filament stability under stress conditions. Without plectin, hepatocytes are unable to poperly regulate the p38-mediated stress response, which contributes to the disruption of the cytoskeletal network.

Taken together, these findings indicate that plectin plays a dual role in both directly stabilizing keratin filaments and modulating stress-response signaling pathways such as p38. The elevated stress-induced activation of p38 in plectin-deficient livers suggests that the loss of plectin renders hepatocytes more sensitive to mechanical and cholestatic stresses, resulting in an overactivation of p38. This, in turn, exacerbates keratin filament disorganization, further compromising the structural integrity of the liver and increasing susceptibility to cholestatic injury.

5 Discussion

In this thesis, I demonstrate that cytoskeletal crosslinker protein plectin is essential for stabilizing the cytoskeleton of hepatocytes and BECs by interlinking keratin filaments, proposed as the guardians of the liver (Omary, Ku, and Toivola 2002), with other cytoskeletal components and anchoring them to cell adhesions, thereby preserving cellular architecture. In the absence of plectin, the liver's ability to adapt to cholestatic stress is significantly compromised, resulting in epithelilal instability and increased mechanical vulnerability of the bile ducts and bile canaliculi. Loss of plectin weakens the liver's resilience to cholestatic insults, ultimately leading to destabilization of the biliary tree and increased susceptibility to injury.

In heathy liver $Ple^{fl/fl}$, hepatocellular keratin filaments are distributed as a cytoplasmic intermediate filament network and as a filamentous layer beneath the apical membrane (Omary, Ku, and Toivola 2002; Tsukada, Ackerley, and Phillips 1995). Hepatocytic keratins K8 and K18 fail to maintain their characteristic membrane-associated distribution, in the absence of plectin, and instead form disorganized cytoplasmic bundles, indicating disrupted filament organization. Krausova et al. (2021) and Prechova et al. (2022) have described similar phenotypes, demonstrating that plectin ablation results in circumferential keratin rim loss and keratin intermediate filament bundling *in vivo* in intestinal epithelial cells of *PLEKO* ($Ple^{\Delta IEC}$) mice and *in vitro* in MDCK (Krausova et al. 2021; Prechova et al. 2022). In BECs, partially due to the high density of the keratin filament network, plectin deficiency has shown less dramatic effect on keratin filament bundling. The apicobasal redistribution of the keratin network, indicating partial loss of apico-basal polarity, was observed in this type of epithelial cells.

In addition to abberant organization of keratin filament, plectin ablation also led to dysregulation of cell-cell adhesion in the BECs, as observed by TEM. Plectin-deficient BECs exhibited significantly shorter tight junctions, while adherens junctions and desmosomes showed similar trends. These findings are consistent with those of Prechova et al. (2022), who reported irregular and significantly widened desmosomes in epithelial sheets following both genetic and pharmacological disruption of plectin function (Prechova et al. 2022).

Although $Ple^{\Delta alb}$ mice exhibited partial loss of polarity and aberrant celluar adhesion in biliary epithelium, no histopathological or serological abnormalities were observed, and bile secretion and composition remained comparable to $Ple^{fl/fl}$ mice. Consistent with findings from

K8/K18KO (Fickert et al., 2009) and *K19KO* (Chen et al., 2015) mice, these results suggest that, under normal physiological conditions, both liver parenchymal cells and BECs in $Ple^{\Delta alb}$ mice remain functionally intact. Similarly, keratin mutations often manifest as mild phenotypes, where structural integrity is preserved in the absence of external stressors, but defects become apparent under conditions of mechanical or cholestatic stress (Ku et al., 2007; Toivola et al., 2010).

Our morphological analysis based on SEM and 3D-reconstruction of bile canaliculi revealed a more branched, distorted, wider, and more meandering plectin-deficient bile canaliculi compared to those in $Ple^{fl/fl}$ livers. In the context of bile canalicular dysmorphology, alterations in the keratin expression or organization of keratin filaments may weaken the cellular skeleton, making bile canaliculi more susceptible to bile flow-induced mechanical stress and deformation. Given the paucity of reported observations in knockout mice deficient for individual keratins, it seems implausible that the canalicular abnormalities observed in $Ple^{\Delta alb}$ livers and in 3D cultures of primary hepatocytes lacking plectin can be attributed solely to disruptions in the keratin filament network (Fickert et al. 2009; Chen et al. 2015).

Recently, Matsubara et al. (2020) demonstrated that plectin forms a scaffold that facilitates the activation of Src and Pyk2, two kinases involved in microtubule organization (Matsubara et al. 2020). By stabilizing microtubules, plectin ensures fidelity of intracellular trafficking, even under conditions of mechanical stress, which is particularly important during bile flow. This is crucial for maintainanace of the polarized architecture of both hepatocytes and BECs. The proper localization of apical transporters, such as ABCB11 (BSEP) and MRP2 at the canalicular membrane, and SLC10A1 at the apical membrane in BECs, relies on functional microtubule dynamics to ensure efficient trafficking and membrane targeting (Li, Sun, and van 2021; Theard et al. 2007; Wakabayashi, Lippincott-Schwartz, and Arias 2004; Marinelli, Tietz, and Larusso 2005). When microtubule function is compromised, trafficking is hampered, leading to mislocalization of key transporters and impaired bile secretion. This disruption not only affects cellular function but also alters bile canaliculi morphology, resulting in structural distortions and increased susceptibility to mechanical stress. Thus, the interplay between plectin, microtubules, and intermediate filaments underscores the importance of cytoskeletal organization in maintaining hepatocyte polarity and bile secretion. These findings, build on previous studies (Krausova et al. 2021; Prechova et al. 2022) that emphasize the structural role of plectin in epithelial cell integrity, are offering new insights into how plectin deficiency

exacerbates cholestatic liver injury by destabilizing the cytoskeletal network and altering bile canalicular morphology.

Li et al. (2016) demonstrated that mechanical intercellular tension plays a crucial role in guiding the elongation of bile canaliculi and accounts for the variability in luminal morphologies (Li et al. 2016). Notably, tension transducers and sensors such as α-catenin (Herr et al. 2014), β-catenin (Yeh et al. 2010), and piezo-1 (Gupta et al. 2020) have been independently shown to influence bile canalicular formation *in vivo*. These mechanosensitive proteins help convert mechanical signals into cellular responses, driving the morphogenesis and stabilization of the bile canaliculi.

Prior studies have shown that plectin-controlled cytoarchitecture is essential for generating effective actomyosin-driven cytoskeletal tension (Gregor, Osmanagic-Myers, Burgstaller, Wolfram, Fischer, Walko, Resch, Jorgl, et al. 2014; Osmanagic-Myers et al. 2015; Prechova et al. 2022). Cytoskeletal tension is necessary for maintaining the structural integrity of hepatocytes, supporting thus the organization of the bile canalicular network. By coordinating the actomyosin system, and other cytoskeletal components, plectin ensures that mechanical forces are properly distributed troughout the cell, enabling canalicular elongation and maintaining bile flow. The aberrant bile canalicular formation observed in $Ple^{\Delta alb}$ mice likely reflects altered mechanical properties and tensional homeostasis of plectin-deficient hepatocytes, resulting from cytoskeletal reconfiguration and a reduction in cellular mechanical stability.

We also found that plectin deficiency leads to the destabilization and collapse of bile ducts even under physiological conditions. Consistent with the widely accepted view that plectin provides mechanical stability to tissues such as skin, muscle and intestines (reviewed in Wiche, 2022), the observed bile duct dysmorphology is likely a result of cholestatic stress acting on the structurally compromised, plectin-deficient BECs. Interestingly, the dysmorphology of the plectin-deficient biliary tree is paralleled by a mild ductular reaction. While this could be attributed to local bile stasis in the irregularly shaped canaliculi or ductules, we did not observe significant upregulation of ALP or bilirubin levels, which are typically indicative of cholestatic conditions, in $Ple^{\Delta alb}$ mice under basal conditions. However, we detected a slight increase in bile flow, which progressively elevated with age. This trend, along with mildly elevated bile flow and serum biomarkers, suggests the presence of a pre-cholestatic state that could become more pronounced under stress or over time. These findings indicate

that while *Ple*$^{\Delta alb}$ mice may initially compensate for plectin deficiency, the liver's capacity to cope with cholestatic stress may diminish with aging, increasing susceptibility to bile duct dysfunction and liver injury.

Experimental models of cholestasis caused aggravated liver injury in *Ple*$^{\Delta alb}$ mice. We used two types of experimental models of cholestasis (i) obstructive (BDL- and DDC-induced cholestasis) and (ii) non-obstructive CA-induced cholestasis model. After BDL, the mechanically unstable, plectin-deficient bile ducts exhibited significant dilation in response to increased bile pressure. This ultimately led to more frequent bile duct ruptures and a higher incidence of bile infarcts, resulting in to more severe liver injury, as reflected by elevated levels of liver injury biomarkers.

In contrast to BDL, damage extent of hepatocytes in the DDC model was higher in *Ple*$^{fl/fl}$ than *Ple*$^{\Delta alb}$ mice whereas had almost no effect on ductular ruptures. This likely reflects the fact that DDC affects primarily small ducts (Fickert et al. 2007) which are less prone to hepatobiliary injury (Glaser et al. 2009). Additionaly, diminished injury in *Ple*$^{\Delta alb}$ liver is consistent with the observation that DDC induced plectin upregulation in *Ple*$^{fl/fl}$ mice to a much lesser extent than BDL. This likely suggests that plectin is not essential for the reorganization of biliary keratin cytoarchitecture (Szabo et al. 2015) under DDC-induced cholestasis. However, slower recovery from DDC-induced liver injury indicates that plectin is required foe effective reparation of periportal damage associated with DDC exposure.

Importantly, in non-obstructive CA-induced cholestasis, abberant hepatic cytoarchitecture in *Ple*$^{\Delta alb}$ mice not only leads to biliary epithelial vulnerability, but also impairs the hepatocellular ability to cope with bile acid burden. This results in increased levels of liver injury biomarkers and increased biliary necrosis in the liver parenchyma, further accompanied by increased ductular reaction and hepatocyte proliferation. Although untreated *Ple*$^{\Delta alb}$ mice show comparable bile composition and secretion as *Ple*$^{fl/fl}$ mice, after feeding with a CA-supplemented diet, *Ple*$^{\Delta alb}$ mice have an abnormal capacity to upregulate expression of bile transporters facilitating thus increased bile secretion. Taken together, our data suggests that *Ple*$^{\Delta alb}$ mice have altered adaptive capacity to overcome bile acid overload.

There are three case reports of PFIC patients suggesting that plectin mutations cause mislocalization of key transporters such as BSEP and MRP2, contributing thus to ductal proliferation, causing cholestasis, and eventually leading to liver failure (Thébaut et al., 2024; Wu et al., 2019; Kor-anantakul et al., 2024). Thébaut et al. (2024) reported that plectin

mutations impaired BSEP targeting and canalicular bile secretion, contributing to the failure of bile acid therapy and progressive cholestasis (Thebaut et al. 2024). Similarly, Wu et al. (2019) described siblings with compound heterozygous *PLEC* mutations who exhibited severe cholestasis and liver fibrosis due to impaired BSEP and MRP2 localization, highlighting the role of plectin in bile canalicular structure and function (Wu et al. 2019). These findings are further supported by Kor-Anantakul et al. (2024), who identified novel *PLEC* variants associated with infantile cholestasis, demonstrating that plectin dysfunction leads to bile duct proliferation and impaired transporter localization, ultimately resulting in liver injury (Kor-Anantakul et al. 2024).

The adaptive tissue response to cholestatic stress is a finely tuned mechanism optimized to enlarge the interface between the ductal lumen and the apical membrane of BECs. BECs express a variety of bile salt transporters, ion channels and aquaporins that play a critical role in modulating bile composition. Vartak et al. (Vartak et al. 2016) describes the spatio-temporal adaptation of intrahepatic bile ducts during the progression of cholestasis from the acute to the chronic phase. BDL-induced cholestasis causes adaptive remodeling aimed at optimizing the intraluminal surface area through corrugation for bile salt reabsorption.

Although both obstructive and non-obstructive cholestatic mouse models resulted in aggravated liver injury in $Ple^{\Delta alb}$ mice, the severity of the injury is surprisingly mild when we consider the reduced mechanical stability of bile ducts lacking plectin. This suppring phenotype may be ascribed to a ductular reaction that ensues in consequence of plectin inactivation under basal conditions. The $Ple^{\Delta alb}$ biliary tree exhibits a pre-adaptive response characterized by an increased intraluminal surface area due to corrugation and an increased number of ductules. This structural remodeling could contribute to an early compensatory mechanism that partially mitigates the effects of cholestatic injury by enhancing drainage capacity of the biliary tree (Vartak et al. 2016). Although these changes help alleviate bile accumulation under basal conditions, they suggest a pre-cholestatic state, where the liver is under constant stress, fostering increased vulnerability to progress into overt cholestasis under stress (such as bile flow obstruction).

We observed a significant increase of progenitor cells in $Ple^{\Delta alb}$ livers in all cholestatic models. Interestingly, this was not accompanied by a corresponding increase in the expected number of $K19^{+}$ cells. This finding reflects a lack of progenitor cell differentiation in these models. Similary, *K19KO* mice challenged by DDC-supplemented diet exhibit a reduced

ductular reaction and impaired progenitor cell proliferation, further emphasizing the critical role of K19 in promoting progenitor cell-mediated liver regeneration during injury (Chen et al. 2015). The increased ductular reaction may be linked to the mechanosensitive signaling such as Hippo pathway (Russell and Camargo 2022). For instance, nuclear localization of transcription factor YAP (Meyer et al., 2020) is during liver regeration driven by elevated actomyosin contractility. Increased contractility not only enhances YAP's nuclear translocation but also promotes the activation of YAP-dependent transcriptional programs that regulate progenitor cell proliferation and differentiation, suggesting a direct mechanotransduction pathway involved in the response to liver injury. A previous study of Prechova et al. (2022) demonstrated increased actomyosin contractility in plectin-deficient MDCK cells (Prechova et al. 2022), suggesting that activation of the mechanosensitive Hippo pathway may partly drive the increased progenitor cell numbers observed in cholestatic $Ple^{\Delta alb}$ livers (Kim et al. 2023; Meyer et al. 2020).

The upregulation of plectin expression in cholestasis models, along with the increased liver damage observed in $Ple^{\Delta alb}$ liver, suggests that plectin plays a crucial hepatoprotective role. Furthermore, bile canaliculi from BDL mice showed more severe canaliculi malformations such as apical membrane blebs, bile canalicular ruptures, and increased bile canalicular width in $Ple^{\Delta alb}$ livers. In the periportal zone, aberrant organization of the parenchymal cytoskeleton in $Ple^{\Delta alb}$ livers is associated with increased remodeling of the bile canalicular network in all cholestatic models (with a surprisingly mild phenotype in BDL model). This suggests different topography of canalicular injury since Meyer et al in 2017 have confirmed that bile pressure is highest in the bile canaliculi near the pericentral zone, and progressively decreases as the bile canalicular network reaches the periportal zone (Meyer et al. 2017). The actomyosin cortex, which supports canalicular domains, responses to bile pressure variations by contractions, particularly under cholestatic conditions when intraluminal pressure rises. Increase in bile pressure, driven by osmotic gradients, can lead to canalicular dysmorphologies, such as dilation, ruptures, and blebs if the luminal pressure surpasses the cortex's strength (Gupta et al. 2017). Indeed, we observed reduced stability of bile canaliculus demonstrated by an increased prevalence of canalicular dysmorphologies. The decreased number and distortion of apical bulkheads, previously described as load-bearing structures (Bebelman et al. 2023; Belicova et al. 2021) in $Ple^{\Delta alb}$ liver further contributes to reduced mechanical destabilitation of bile canalicular network.

The upregulation of stress-responsive proteins, such as keratins (K8/K18, K19) and plakins (epiplakin, periplakin), has been observed during cholestasis, emphasizing their role in reinforcing the mechanical stability of liver cells (Fickert et al. 2002; Chen et al. 2015; Szabo et al. 2015; Jang et al. 2019). In addition to these cytoskeletal components, liver epithelial cells also upregulate the expression of adhesion molecules, such as those forming tight and adherens junctions (E-cadherin), which are critical for maintaining tissue cohesion under stress (Ito et al. 2013; Maly and Landmann 2008). This complex adaptive response provides the liver epithelium with resilience against the increased mechanical pressure associated with cholestasis.

In $Ple^{\Delta alb}$ mice, we observed that plectin deficiency perturbs keratin filament organization in both hepatocytes and BECs, leading to distorted tight junctions and increased expression of the adherens junction protein E-cadherin. Interestingly, there was no upregulation of desmoplakin, a known binding partner of plectin that anchors keratin filaments to desmosomes. While these changes did not compromise the overall biliary barrier, they strongly suggest that plectin plays a critical role in maintaining biliary epithelial stability and facilitating the adaptive reorganization of the cytoskeleton and cell-cell cohesion under stress.

The p38 MAP kinase is a well-established mediator of the cellular stress response in hepatocytes, particularly during cholestasis, where increased bile toxicity and pressure can severely impact cell function. Previous studies have demonstrated that the collapse of keratin filaments can activate p38, initiating a feedback loop that compromises cellular integrity and exacerbates stress conditions. Once activated, p38 phosphorylates keratin proteins, notably K8 and K18, leading to their reorganization and destabilization (Osmanagic-Myers et al. 2006). This process has been linked to reduced cytoskeletal stability, rendering hepatocytes more vulnerable to continued stress and shifting the balance toward necrosis, ultimately worsening liver injury (Meyer et al., 2020).

Our findings support this model, showing that plectin-deficient hepatocytes exhibit enhanced p38 activity in response to stress, which leads to hyperphosphorylation of keratin filaments and further destabilization of the cytoskeleton. Similar to prior observations in keratinocytes (Osmanagic-Myers et al. 2006), this destabilization likely contributes to structural alterations, impaired cell integrity, and enhanced susceptibility to liver injury.

In addition to its role in cytoskeletal regulation, plectin also interacts with key metabolic regulators, such as AMPK, which stabilizes tight junctions and preserves cell polarity under

stress (Porat-Shliom et al. 2016; Gregor, Zeold, et al. 2006). It has been shown that LKB1, a major kinase for AMPK activation, plays a crucial role in microtubule-dependent trafficking of ABCB11 to the canalicular membrane (Homolya et al. 2014). The dysregulation of these signaling pathways in plectin-deficient models may represent alternative “non-mechanical” mechanisms underlay plectin-dependent effects of stress on liver function.

Plectin’s regulation of cellular integrity and polarity and its interplay with signaling pathways, represents a pivotal factor in the establishment of the biliary barrier. Further studies are needed to elucidate synergistic effect of various mechanisms and their roles in the development and progression of human liver diseases.

6 Conclusion

In this thesis, I have explored the critical role of plectin, a versatile cytolinker protein, in maintaining the structural integrity and cytoarchitecture of liver epithelial cells, particularly in the context of cholestasis. My findings demonstrate that plectin is indispensable for the organization of keratin filaments in both hepatocytes and BECs, playing a vital role in safeguarding the liver's structural integrity under both basal conditions and during cholestatic stress.

The characterization of liver-specific plectin knockout ($Ple^{\Delta alb}$) mice provided valuable insights into the function of plectin in the liver. Under basal conditions, the absence of plectin led to significant alterations in the organization of keratin filaments, with hepatocytic keratins K8 and K18 losing their typical peri-membranous distribution and forming disorganized bundles throughout the cytoplasm. In BECs, plectin deficiency resulted in a less pronounced but still significant disruption of keratin filaments, with an apicobasal redistribution observed. These changes in cytoarchitecture were accompanied by dysregulation of cell-cell adhesions, particularly in the biliary epithelium, where shorter tight junctions and elevated levels of E-cadherin were observed in $Ple^{\Delta alb}$ bile ducts. Despite these structural abnormalities, $Ple^{\Delta alb}$ mice exhibited no significant histopathological or serological defects under physiological conditions, suggesting that the liver's basal function remains intact in the absence of plectin.

However, when challenged in three cholestatic liver injury models: BDL, DDC feeding, and CA feeding, $Ple^{\Delta alb}$ mice showed increased susceptibility to liver injury. The mechanically unstable plectin-deficient bile ducts were more prone to dilation, rupture, and bile infarcts under increased bile pressure, leading to more severe liver damage. Interestingly, while plectin deficiency exacerbated biliary damage, it also resulted in a surprisingly mild parenchymal injury in the DDC model, suggesting a differential impact on liver tissue based on the nature of the cholestatic insult. Furthermore, $Ple^{\Delta alb}$ mice exhibited a pre-adaptive remodeling of the biliary tree, characterized by increased ductular reaction and an expansion of $A6^{+}$ progenitor cells, particularly under cholestatic stress thus contributing to preadaptation to ongoing cholestatic challenge.

Our findings also highlighted the critical role of plectin in the adaptive response of liver epithelial cells to mechanical stress. Plectin-deficient mice exhibited increased apical membrane blebs, bile canaliculi ruptures, and altered bile canalicular morphology, underscoring the importance of plectin in maintaining the integrity of the bile canalicular

network under cholestatic conditions. Observed dysmorphologies, including the disruption of apical bulkheads, load-bearing structures essential for stabilizing bile canaliculi, further emphasize the role of plectin in preserving liver architecture especially under pathologic conditions.

Moreover, the dysregulation of keratin filaments in plectin-deficient liver epithelial cells was linked to altered p38 MAP kinase signaling, a key pathway implicated in the stress response. The elevated p38 activity in $Ple^{\Delta alb}$ mice under stress conditions suggests a feedback loop between plectin-organized keratin filaments and p38 activation, contributing to the increased fragility of the keratin network and the liver's vulnerability to cholestatic injury.

In conclusion, this thesis underscores the hepatoprotective role of plectin in maintaining the structural integrity and mechanical stability of liver epithelial cells, particularly in the context of cholestatic stress. The findings presented herein provide a deeper understanding of the molecular mechanisms underlying liver cytoarchitecture and highlight the importance of plectin in preserving liver function and facilitating adaptive responses to cholestasis. Further research is needed to elucidate the precise signaling pathways and interactions involved in plectin's role in liver biology and its potential implications for the development and progression of human liver diseases.

7 References

Ackerl, R., G. Walko, P. Fuchs, I. Fischer, M. Schmuth, and G. Wiche. 2007. 'Conditional targeting of plectin in prenatal and adult mouse stratified epithelia causes keratinocyte fragility and lesional epidermal barrier defects', *J Cell Sci*, 120: 2435-43.

Akhtar, N., and C. H. Streuli. 2013. 'An integrin-ILK-microtubule network orients cell polarity and lumen formation in glandular epithelium', *Nat Cell Biol*, 15: 17-27.

Alpini, G., S. Roberts, S. M. Kuntz, Y. Ueno, S. Gubba, P. V. Podila, G. LeSage, and N. F. LaRusso. 1996. 'Morphological, molecular, and functional heterogeneity of cholangiocytes from normal rat liver', *Gastroenterology*, 110: 1636-43.

Alvaro, D., M. G. Mancino, S. Glaser, E. Gaudio, M. Marzioni, H. Francis, and G. Alpini. 2007. 'Proliferating cholangiocytes: a neuroendocrine compartment in the diseased liver', *Gastroenterology*, 132: 415-31.

Antoniou, A., P. Raynaud, S. Cordi, Y. Zong, F. Tronche, B. Z. Stanger, P. Jacquemin, C. E. Pierreux, F. Clotman, and F. P. Lemaigre. 2009. 'Intrahepatic bile ducts develop according to a new mode of tubulogenesis regulated by the transcription factor SOX9', *Gastroenterology*, 136: 2325-33.

Arteel, G. E., J. A. Raleigh, B. U. Bradford, and R. G. Thurman. 1996. 'Acute alcohol produces hypoxia directly in rat liver tissue in vivo: role of Kupffer cells', *Am J Physiol*, 271: G494-500.

Bataller, R., and D. A. Brenner. 2005. 'Liver fibrosis', *J Clin Invest*, 115: 209-18.

Baum, B., and M. Georgiou. 2011. 'Dynamics of adherens junctions in epithelial establishment, maintenance, and remodeling', *J Cell Biol*, 192: 907-17.

Bebelman, M. P., M. J. Bovyn, C. M. Mayer, J. Delpierre, R. Naumann, N. P. Martins, A. Honigmann, Y. Kalaidzidis, P. A. Haas, and M. Zerial. 2023. 'Hepatocyte apical bulkheads provide a mechanical means to oppose bile pressure', *J Cell Biol*, 222.

Belicova, L., U. Repnik, J. Delpierre, E. Gralinska, S. Seifert, J. I. Valenzuela, H. A. Morales-Navarrete, C. Franke, H. Raagel, E. Shcherbinina, T. Prikazchikova, V. Koteliansky, M. Vingron, Y. L. Kalaidzidis, T. Zatsepin, and M. Zerial. 2021. 'Anisotropic expansion of hepatocyte lumina enforced by apical bulkheads', *J Cell Biol*, 220.

Blanco, P. G., M. M. Zaman, O. Junaidi, S. Sheth, R. K. Yantiss, I. A. Nasser, and S. D. Freedman. 2004. 'Induction of colitis in cftr-/- mice results in bile duct injury', *Am J Physiol Gastrointest Liver Physiol*, 287: G491-6.

Bloomer, J., C. Bruzzone, L. Zhu, Y. Scarlett, S. Magness, and D. Brenner. 1998. 'Molecular defects in ferrochelatase in patients with protoporphyria requiring liver transplantation', *J Clin Invest*, 102: 107-14.

Blouin, A., R. P. Bolender, and E. R. Weibel. 1977. 'Distribution of organelles and membranes between hepatocytes and nonhepatocytes in the rat liver parenchyma. A stereological study', *J Cell Biol*, 72: 441-55.

Boron, W.F., and E.L. Boulpaep. 2016. *Medical Physiology E-Book* (Elsevier Health Sciences).

Bouameur, Jamal Eddine, Bertrand Favre, and Luca Borradori. 2014. "Plakins, a versatile family of cytolinkers: Roles in skin integrity and in human diseases." In *Journal of Investigative Dermatology*, 885-94. Nature Publishing Group.

Boyer, J. L. 1983. 'Tight junctions in normal and cholestatic liver: does the paracellular pathway have functional significance?', *Hepatology*, 3: 614-7.

———. 2013. 'Bile formation and secretion', *Compr Physiol*, 3: 1035-78.

Boyer, J. L., and C. J. Soroka. 2021. 'Bile formation and secretion: An update', *J Hepatol*, 75: 190-201.

Boyer, T.D., M.P. Manns, A.J. Sanyal, and D. Zakim. 2012. *Zakim and Boyer's Hepatology: A Textbook of Liver Disease* (Saunders/Elsevier).

Bryant, D. M., A. Datta, A. E. Rodriguez-Fraticelli, J. Peranen, F. Martin-Belmonte, and K. E. Mostov. 2010. 'A molecular network for de novo generation of the apical surface and lumen', *Nat Cell Biol*, 12: 1035-45.

Bryant, D. M., and K. E. Mostov. 2008. 'From cells to organs: building polarized tissue', *Nat Rev Mol Cell Biol*, 9: 887-901.

Burgstaller, G., M. Gregor, L. Winter, and G. Wiche. 2010. 'Keeping the vimentin network under control: cell-matrix adhesion-associated plectin 1f affects cell shape and polarity of fibroblasts', *Mol Biol Cell*, 21: 3362-75.

Cai, S. Y., and J. L. Boyer. 2021. 'The role of bile acids in cholestatic liver injury', *Ann Transl Med*, 9: 737.

Cai, S. Y., X. Ouyang, Y. Chen, C. J. Soroka, J. Wang, A. Mennone, Y. Wang, W. Z. Mehal, D. Jain, and J. L. Boyer. 2017. 'Bile acids initiate cholestatic liver injury by triggering a hepatocyte-specific inflammatory response', *JCI Insight*, 2: e90780.

Campanale, J. P., T. Y. Sun, and D. J. Montell. 2017. 'Development and dynamics of cell polarity at a glance', *J Cell Sci*, 130: 1201-07.

Castañón, Maria J., Gernot Walko, Lilli Winter, and Gerhard Wiche. 2013. "Plectin-intermediate filament partnership in skin, skeletal muscle, and peripheral nerve." In *Histochemistry and Cell Biology*, 33-53. Histochem Cell Biol.

Cozmescu, C. A., and P. Gissen. 2021. 'Rab35 controls formation of luminal projections required for bile canalicular morphogenesis', *J Cell Biol*, 220.

Cunningham, R. P., and N. Porat-Shliom. 2021. 'Liver Zonation - Revisiting Old Questions With New Technologies', *Front Physiol*, 12: 732929.

Dasgupta, S., K. Gupta, Y. Zhang, V. Viasnoff, and J. Prost. 2018. 'Physics of lumen growth', *Proc Natl Acad Sci U S A*, 115: E4751-E57.

Datta, A., D. M. Bryant, and K. E. Mostov. 2011. 'Molecular regulation of lumen morphogenesis', *Curr Biol*, 21: R126-36.

De Groot, H., A. Littauer, D. Hugo-Wissemann, P. Wissemann, and T. Noll. 1988. 'Lipid peroxidation and cell viability in isolated hepatocytes in a redesigned oxystat system: evaluation of the hypothesis that lipid peroxidation, preferentially induced at low oxygen partial pressures, is decisive for CCl4 liver cell injury', *Arch Biochem Biophys*, 264: 591-9.

Deharde, D., C. Schneider, T. Hiller, N. Fischer, V. Kegel, M. Lubberstedt, N. Freyer, J. G. Hengstler, T. B. Andersson, D. Seehofer, J. Pratschke, K. Zeilinger, and G. Damm. 2016. 'Bile canaliculi formation and biliary transport in 3D sandwich-cultured hepatocytes in dependence of the extracellular matrix composition', *Arch Toxicol*, 90: 2497-511.

Durie, P. R., G. Kent, M. J. Phillips, and C. A. Ackerley. 2004. 'Characteristic multiorgan pathology of cystic fibrosis in a long-living cystic fibrosis transmembrane regulator knockout murine model', *Am J Pathol*, 164: 1481-93.

European Association for the Study of the Liver. Electronic address, easloffice easloffice eu, and Liver European Association for the Study of the. 2022. 'EASL Clinical Practice Guidelines on sclerosing cholangitis', *J Hepatol*, 77: 761-806.

Feracci, H., T. P. Connolly, R. N. Margolis, and A. L. Hubbard. 1987. 'The establishment of hepatocyte cell surface polarity during fetal liver development', *Dev Biol*, 123: 73-84.

Fickert, P. 2014. 'Time to say goodbye to the drug or the model? - why do drugs fail to live up to their promise in bile duct ligated mice?', *J Hepatol*, 60: 12-5.

Fickert, P., A. Fuchsbichler, H. U. Marschall, M. Wagner, G. Zollner, R. Krause, K. Zatloukal, H. Jaeschke, H. Denk, and M. Trauner. 2006. 'Lithocholic acid feeding induces segmental bile duct obstruction and destructive cholangitis in mice', *Am J Pathol*, 168: 410-22.

Fickert, P., A. Fuchsbichler, M. Wagner, D. Silbert, K. Zatloukal, H. Denk, and M. Trauner. 2009. 'The role of the hepatocyte cytokeratin network in bile formation and resistance to bile acid challenge and cholestasis in mice', *Hepatology*, 50: 893-9.

Fickert, P., M. J. Pollheimer, U. Beuers, C. Lackner, G. Hirschfield, C. Housset, V. Keitel, C. Schramm, H. U. Marschall, T. H. Karlsen, E. Melum, A. Kaser, B. Eksteen, M. Strazzabosco, M. Manns, M. Trauner, and P. S. C. Study Group International. 2014. 'Characterization of animal models for primary sclerosing cholangitis (PSC)', *J Hepatol*, 60: 1290-303.

Fickert, P., U. Stoger, A. Fuchsbichler, T. Moustafa, H. U. Marschall, A. H. Weiglein, O. Tsybrovskyy, H. Jaeschke, K. Zatloukal, H. Denk, and M. Trauner. 2007. 'A new xenobiotic-induced mouse model of sclerosing cholangitis and biliary fibrosis', *Am J Pathol*, 171: 525-36.

Fickert, P., M. Wagner, H. U. Marschall, A. Fuchsbichler, G. Zollner, O. Tsybrovskyy, K. Zatloukal, J. Liu, M. P. Waalkes, C. Cover, H. Denk, A. F. Hofmann, H. Jaeschke, and M. Trauner. 2006. '24-norUrsodeoxycholic acid is superior to ursodeoxycholic acid in the treatment of sclerosing cholangitis in Mdr2 (Abcb4) knockout mice', *Gastroenterology*, 130: 465-81.

Fickert, P., G. Zollner, A. Fuchsbichler, C. Stumptner, A. H. Weiglein, F. Lammert, H. U. Marschall, O. Tsybrovskyy, K. Zatloukal, H. Denk, and M. Trauner. 2002. 'Ursodeoxycholic acid aggravates bile infarcts in bile duct-ligated and Mdr2 knockout mice via disruption of cholangioles', *Gastroenterology*, 123: 1238-51.

Flores-Benitez, D., and E. Knust. 2015. 'Crumbs is an essential regulator of cytoskeletal dynamics and cell-cell adhesion during dorsal closure in Drosophila', *Elife*, 4.

Franz, A., and V. Riechmann. 2010. 'Stepwise polarisation of the Drosophila follicular epithelium', *Dev Biol*, 338: 136-47.

Fu, D., Y. Wakabayashi, Y. Ido, J. Lippincott-Schwartz, and I. M. Arias. 2010. 'Regulation of bile canalicular network formation and maintenance by AMP-activated protein kinase and LKB1', *J Cell Sci*, 123: 3294-302.

Fuchs, P., M. Zorer, G. A. Rezniczek, D. Spazierer, S. Oehler, M. J. Castanon, R. Hauptmann, and G. Wiche. 1999. 'Unusual 5' transcript complexity of plectin isoforms: novel tissue-specific exons modulate actin binding activity', *Hum Mol Genet*, 8: 2461-72.

Garrido, M., C. Escobar, C. Zamora, C. Rejas, J. Varas, M. Parraga, S. San Martin, and S. Montedonico. 2017. 'Bile duct ligature in young rats: A revisited animal model for biliary atresia', *Eur J Histochem*, 61: 2803.

Gayathri, A. K., and G. Padmanaban. 1974. 'Biochemical effects of 3,5-diethoxycarbonyl-1,4-dihydrocollidine in mouse liver', *Biochem Pharmacol*, 23: 2713-25.

Gebhardt, R. 1992. 'Metabolic zonation of the liver: regulation and implications for liver function', *Pharmacol Ther*, 53: 275-354.

Gebhardt, R., and M. Matz-Soja. 2014. 'Liver zonation: Novel aspects of its regulation and its impact on homeostasis', *World J Gastroenterol*, 20: 8491-504.

Geerts, A. M., E. Vanheule, M. Praet, H. Van Vlierberghe, M. De Vos, and I. Colle. 2008. 'Comparison of three research models of portal hypertension in mice: macroscopic, histological and portal pressure evaluation', *Int J Exp Pathol*, 89: 251-63.

Gijbels, E., A. Pieters, K. De Muynck, M. Vinken, and L. Devisscher. 2021. 'Rodent models of cholestatic liver disease: A practical guide for translational research', *Liver Int*, 41: 656-82.

Gissen, P., and I. M. Arias. 2015. 'Structural and functional hepatocyte polarity and liver disease', *J Hepatol*, 63: 1023-37.

Glaser, S. S., E. Gaudio, A. Rao, L. M. Pierce, P. Onori, A. Franchitto, H. L. Francis, D. E. Dostal, J. K. Venter, S. DeMorrow, R. Mancinelli, G. Carpino, D. Alvaro, S. E. Kopriva, J. M. Savage, and G. D. Alpini. 2009. 'Morphological and functional heterogeneity of the mouse intrahepatic biliary epithelium', *Lab Invest*, 89: 456-69.

Gooijert, K. E., R. Havinga, H. Wolters, R. Wang, V. Ling, S. Tazuma, and H. J. Verkade. 2015. 'The mechanism of increased biliary lipid secretion in mice with genetic inactivation of bile salt export pump', *Am J Physiol Gastrointest Liver Physiol*, 308: G450-7.

Gregor, M., S. Osmanagic-Myers, G. Burgstaller, M. Wolfram, I. Fischer, G. Walko, G. P. Resch, A. Jorgl, H. Herrmann, and G. Wiche. 2014. 'Mechanosensing through focal adhesion-anchored intermediate filaments', *FASEB J*, 28: 715-29.

Gregor, M., S. Osmanagic-Myers, G. Burgstaller, M. Wolfram, I. Fischer, G. Walko, G. P. Resch, A. Jörgl, H. Herrmann, and G. Wiche. 2014. 'Mechanosensing through focal adhesion-anchored intermediate filaments', *FASEB J*, 28: 715-29.

Gregor, M., A. Zeold, S. Oehler, K. A. Marobela, P. Fuchs, G. Weigel, D. G. Hardie, and G. Wiche. 2006. 'Plectin scaffolds recruit energy-controlling AMP-activated protein kinase (AMPK) in differentiated myofibres', *J Cell Sci*, 119: 1864-75.

Gregor, Martin, Aniko Zeöld, Susanne Oehler, Kerstin Andrä Marobela, Peter Fuchs, Günter Weigel, D. Graham Hardie, and Gerhard Wiche. 2006. 'Plectin scaffolds recruit energy-controlling AMP-activated protein kinase (AMPK) in differentiated myofibres', *Journal of Cell Science*, 119: 1864-75.

Gribben, C., V. Galanakis, A. Calderwood, E. C. Williams, R. Chazarra-Gil, M. Larraz, C. Frau, T. Puengel, A. Guillot, F. J. Rouhani, K. Mahbubani, E. Godfrey, S. E. Davies, E. Athanasiadis, K. Saeb-Parsy, F. Tacke, M. Allison, I. Mohorianu, and L. Vallier. 2024. 'Acquisition of epithelial plasticity in human chronic liver disease', *Nature*, 630: 166-73.

Gupta, K. 2023. 'A modular analysis of bile canalicular function and its implications for cholestasis', *Am J Physiol Gastrointest Liver Physiol*, 325: G14-G22.

Gupta, K., Q. Li, J. J. Fan, E. L. S. Fong, Z. Song, S. Mo, H. Tang, I. C. Ng, C. W. Ng, P. Pawijit, S. Zhuo, C. Y. Dong, B. C. Low, A. Wee, Y. Y. Dan, P. Kanchanawong, P. So, V. Viasnoff, and H. Yu. 2017. 'Actomyosin contractility drives bile regurgitation as an early response during obstructive cholestasis', *J Hepatol*, 66: 1231-40.

Gupta, K., I. C. Ng, G. M. Balachander, B. P. Nguyen, L. Tucker-Kellogg, B. C. Low, and H. Yu. 2020. 'Bile canaliculi contract autonomously by releasing calcium into hepatocytes via mechanosensitive calcium channel', *Biomaterials*, 259: 120283.

Hadj-Rabia, S., L. Baala, P. Vabres, D. Hamel-Teillac, E. Jacquemin, M. Fabre, S. Lyonnet, Y. De Prost, A. Munnich, M. Hadchouel, and A. Smahi. 2004. 'Claudin-1 gene mutations in neonatal sclerosing cholangitis associated with ichthyosis: a tight junction disease', *Gastroenterology*, 127: 1386-90.

Han, X., C. Lin, H. Liu, S. Li, B. Hu, and L. Zhang. 2024. 'Allocholic acid protects against alpha-naphthylisothiocyanate-induced cholestasis in mice by ameliorating disordered bile acid homeostasis', *J Appl Toxicol*, 44: 582-94.

Hawley, S. A., M. Davison, A. Woods, S. P. Davies, R. K. Beri, D. Carling, and D. G. Hardie. 1996. 'Characterization of the AMP-activated protein kinase kinase from rat liver and identification of threonine 172 as the major site at which it phosphorylates AMP-activated protein kinase', *J Biol Chem*, 271: 27879-87.

Heinrich, S., P. Georgiev, A. Weber, A. Vergopoulos, R. Graf, and P. A. Clavien. 2011. 'Partial bile duct ligation in mice: a novel model of acute cholestasis', *Surgery*, 149: 445-51.

Herr, K. J., Y. H. Tsang, J. W. Ong, Q. Li, L. L. Yap, W. Yu, H. Yin, R. L. Bogorad, J. E. Dahlman, Y. G. Chan, B. H. Bay, R. Singaraja, D. G. Anderson, V. Koteliansky, V. Viasnoff, and J. P. Thiery. 2014. 'Loss of alpha-catenin elicits a cholestatic response and impairs liver regeneration', *Sci Rep*, 4: 6835.

Homolya, L., D. Fu, P. Sengupta, M. Jarnik, J. P. Gillet, L. Vitale-Cross, J. S. Gutkind, J. Lippincott-Schwartz, and I. M. Arias. 2014. 'LKB1/AMPK and PKA control ABCB11 trafficking and polarization in hepatocytes', *PLoS One*, 9: e91921.

Hutchins, G. F., and J. L. Gollan. 2004. 'Recent developments in the pathophysiology of cholestasis', *Clin Liver Dis*, 8: 1-26, v.

Chen, Y., N. Guldiken, M. Spurny, H. H. Mohammed, J. Haybaeck, M. J. Pollheimer, P. Fickert, N. Gassler, M. K. Jeon, C. Trautwein, and P. Strnad. 2015. 'Loss of keratin 19 favours the development of cholestatic liver disease through decreased ductular reaction', *J Pathol*, 237: 343-54.

Ikenaga, N., S. B. Liu, D. Y. Sverdlov, S. Yoshida, I. Nasser, Q. Ke, P. M. Kang, and Y. Popov. 2015. 'A new Mdr2(-/-) mouse model of sclerosing cholangitis with rapid fibrosis progression, early-onset portal hypertension, and liver cancer', *Am J Pathol*, 185: 325-34.

Israel, Y., and H. Orrego. 1984. 'Hypermetabolic state and hypoxic liver damage', *Recent Dev Alcohol*, 2: 119-33.

Ito, S., J. Satoh, T. Matsubara, Y. M. Shah, S. H. Ahn, C. R. Anderson, W. Shan, J. M. Peters, and F. J. Gonzalez. 2013. 'Cholestasis induces reversible accumulation of periplakin in mouse liver', *BMC Gastroenterol*, 13: 116.

Jacob, J. T., P. A. Coulombe, R. Kwan, and M. B. Omary. 2018. 'Types I and II Keratin Intermediate Filaments', *Cold Spring Harb Perspect Biol*, 10.

Jang, K. H., H. N. Yoon, J. Lee, H. Yi, S. Y. Park, S. Y. Lee, Y. Lim, H. J. Lee, J. W. Cho, Y. K. Paik, W. S. Hancock, and N. O. Ku. 2019. 'Liver disease-associated keratin 8 and 18 mutations modulate keratin acetylation and methylation', *FASEB J*, 33: 9030-43.

Jungermann, K. 1986. 'Dynamics of zonal hepatocyte heterogeneity. Perinatal development and adaptive alterations during regeneration after partial hepatectomy, starvation and diabetes', *Acta Histochem Suppl*, 32: 89-98.

Jungermann, K., and T. Kietzmann. 1996. 'Zonation of parenchymal and nonparenchymal metabolism in liver', *Annu Rev Nutr*, 16: 179-203.

Jungst, C., T. Berg, J. Cheng, R. M. Green, J. Jia, A. L. Mason, and F. Lammert. 2013. 'Intrahepatic cholestasis in common chronic liver diseases', *Eur J Clin Invest*, 43: 1069-83.

Just, P. A., A. Poncy, S. Charawi, R. Dahmani, M. Traore, T. Dumontet, V. Drouet, F. Dumont, H. Gilgenkrantz, S. Colnot, B. Terris, C. Coulouarn, F. Lemaigre, and C. Perret. 2015. 'LKB1 and Notch Pathways Interact and Control Biliary Morphogenesis', *PLoS One*, 10: e0145400.

Kah, Delf, Alexander Winterl, Magdalena Přechová, Ulrike Schöler, Werner Schneider, Oliver Friedrich, Martin Gregor, and Ben Fabry. 2021. 'A low-cost uniaxial cell stretcher for six parallel wells', *HardwareX*, 9: e00162.

Ketema, Mirjam, Maaike Kreft, Pablo Secades, Hans Janssen, and Arnoud Sonnenberg. 2013. 'Nesprin-3 connects plectin and vimentin to the nuclear envelope of Sertoli cells but is not required for Sertoli cell function in spermatogenesis', *Molecular Biology of the Cell*, 24: 2454-66.

Kietzmann, T., E. Y. Dimova, D. Flugel, and J. G. Scharf. 2006. 'Oxygen: modulator of physiological and pathophysiological processes in the liver', *Z Gastroenterol*, 44: 67-76.

Kikuchi, S., M. Hata, K. Fukumoto, Y. Yamane, T. Matsui, A. Tamura, S. Yonemura, H. Yamagishi, D. Keppler, S. Tsukita, and S. Tsukita. 2002. 'Radixin deficiency causes conjugated hyperbilirubinemia with loss of Mrp2 from bile canalicular membranes', *Nat Genet*, 31: 320-5.

Kim, E., B. D. Riehl, T. Bouzid, R. Yang, B. Duan, H. J. Donahue, and J. Y. Lim. 2023. 'YAP mechanotransduction under cyclic mechanical stretch loading for mesenchymal stem cell osteogenesis is regulated by ROCK', *Front Bioeng Biotechnol*, 11: 1306002.

Kipp, H., and I. M. Arias. 2000. 'Newly synthesized canalicular ABC transporters are directly targeted from the Golgi to the hepatocyte apical domain in rat liver', *J Biol Chem*, 275: 15917-25.

Kojima, T., M. Murata, M. Go, D. C. Spray, and N. Sawada. 2007. 'Connexins induce and maintain tight junctions in epithelial cells', *J Membr Biol*, 217: 13-9.

Kojima, T., N. Sawada, H. Chiba, Y. Kokai, M. Yamamoto, M. Urban, G. H. Lee, E. L. Hertzberg, Y. Mochizuki, and D. C. Spray. 1999. 'Induction of tight junctions in human connexin 32 (hCx32)-transfected mouse hepatocytes: connexin 32 interacts with occludin', *Biochem Biophys Res Commun*, 266: 222-9.

Kong, J., B. B. Liu, S. D. Wu, Y. Wang, Q. Q. Jiang, and E. L. Guo. 2014. 'Enhancement of interaction of BSEP and HAX-1 on the canalicular membrane of hepatocytes in a mouse model of cholesterol cholelithiasis', *Int J Clin Exp Pathol*, 7: 1644-50.

Kor-Anantakul, P., H. L. Chen, Y. H. Chen, C. Ittiwut, R. Ittiwut, N. Chaijitraruch, K. Suphapeetiporn, and V. Chongsrisawat. 2024. 'Novel PLEC variants associated with infantile cholestasis', *Clin Genet*.

Kostan, Julius, Martin Gregor, Gernot Walko, and Gerhard Wiche. 2009. 'Plectin isoform-dependent regulation of keratin-integrin α6β4 anchorage via Ca2+/calmodulin', *Journal of Biological Chemistry*, 284: 18525-36.

Krausova, A., P. Buresova, L. Sarnova, G. Oyman-Eyrilmez, J. Skarda, P. Wohl, L. Bajer, E. Sticova, L. Bartonova, J. Pacha, G. Koubkova, J. Prochazka, M. Sporrer, C. Durrbeck, Z. Stehlikova, M. Vit, N. Ziolkowska, R. Sedlacek, D. Jirak, M. Kverka, G. Wiche, B. Fabry, V. Korinek, and M. Gregor. 2021. 'Plectin ensures intestinal epithelial integrity and protects colon against colitis', *Mucosal Immunol*, 14: 691-702.

Krizhanovsky, V., M. Yon, R. A. Dickins, S. Hearn, J. Simon, C. Miething, H. Yee, L. Zender, and S. W. Lowe. 2008. 'Senescence of activated stellate cells limits liver fibrosis', *Cell*, 134: 657-67.

Ku, N. O., P. Strnad, H. Bantel, and M. B. Omary. 2016. 'Keratins: Biomarkers and modulators of apoptotic and necrotic cell death in the liver', *Hepatology*, 64: 966-76.

Ku, N. O., D. M. Toivola, P. Strnad, and M. B. Omary. 2010. 'Cytoskeletal keratin glycosylation protects epithelial tissue from injury', *Nat Cell Biol*, 12: 876-85.

Leung, Conrad L., Kathleen J. Green, and Ronald K. H. Liem. 2002. "Plakins: A family of versatile cytolinker proteins." In *Trends in Cell Biology*, 37-45. Elsevier.

Lewis, J. H., and H. J. Zimmerman. 1999. 'Drug- and chemical-induced cholestasis', *Clin Liver Dis*, 3: 433-64, vii.

Li, M., W. Wang, C. J. Soroka, A. Mennone, K. Harry, E. J. Weinman, and J. L. Boyer. 2010. 'NHERF-1 binds to Mrp2 and regulates hepatic Mrp2 expression and function', *J Biol Chem*, 285: 19299-307.

Li, M., J. Zhang, Z. Li, Z. Xu, S. Qian, L. J. Tay, Z. Zhang, F. Yang, and Y. Huang. 2024. 'The role and mechanism of SUMO modification in liver disease', *Biomed Pharmacother*, 177: 116898.

Li, Q., Y. Sun, and IJzendoorn S. C. D. van. 2021. 'A Link between Intrahepatic Cholestasis and Genetic Variations in Intracellular Trafficking Regulators', *Biology (Basel)*, 10.

Li, Q., Y. Zhang, P. Pluchon, J. Robens, K. Herr, M. Mercade, J. P. Thiery, H. Yu, and V. Viasnoff. 2016. 'Extracellular matrix scaffolding guides lumen elongation by inducing anisotropic intercellular mechanical tension', *Nat Cell Biol*, 18: 311-8.

Libbrecht, L., L. Meerman, F. Kuipers, T. Roskams, V. Desmet, and P. Jansen. 2003. 'Liver pathology and hepatocarcinogenesis in a long-term mouse model of erythropoietic protoporphyria', *J Pathol*, 199: 191-200.

Lleo, A., L. Maroni, S. Glaser, G. Alpini, and M. Marzioni. 2014. 'Role of cholangiocytes in primary biliary cirrhosis', *Semin Liver Dis*, 34: 273-84.

Ludwig, J. 1987. 'New concepts in biliary cirrhosis', *Semin Liver Dis*, 7: 293-301.

Majumdar, D., J. P. Tiernan, A. J. Lobo, C. A. Evans, and B. M. Corfe. 2012. 'Keratins in colorectal epithelial function and disease', *Int J Exp Pathol*, 93: 305-18.

Malinen, M. M., H. Palokangas, M. Yliperttula, and A. Urtti. 2012. 'Peptide nanofiber hydrogel induces formation of bile canaliculi structures in three-dimensional hepatic cell culture', *Tissue Eng Part A*, 18: 2418-25.

Maly, I. P., and L. Landmann. 2008. 'Bile duct ligation in the rat causes upregulation of ZO-2 and decreased colocalization of claudins with ZO-1 and occludin', *Histochem Cell Biol*, 129: 289-99.

Marinelli, R. A., P. S. Tietz, and N. F. Larusso. 2005. 'Regulated vesicle trafficking of membrane transporters in hepatic epithelia', *J Hepatol*, 42: 592-603.

Mariotti, V., M. Strazzabosco, L. Fabris, and D. F. Calvisi. 2018. 'Animal models of biliary injury and altered bile acid metabolism', *Biochim Biophys Acta Mol Basis Dis*, 1864: 1254-61.

Martin, C. R., M. M. Zaman, G. A. Ketwaroo, A. Q. Bhutta, E. Coronel, Y. Popov, D. Schuppan, and S. D. Freedman. 2012. 'CFTR dysfunction predisposes to fibrotic liver disease in a murine model', *Am J Physiol Gastrointest Liver Physiol*, 303: G474-81.

Matsubara, T., T. Yaginuma, W. N. Addison, Y. Fujita, K. Watanabe, I. Yoshioka, H. Hikiji, K. Maki, R. Baron, and S. Kokabu. 2020. 'Plectin stabilizes microtubules during osteoclastic bone resorption by acting as a scaffold for Src and Pyk2', *Bone*, 132: 115209.

Mauad, T. H., C. M. van Nieuwkerk, K. P. Dingemans, J. J. Smit, A. H. Schinkel, R. G. Notenboom, M. A. van den Bergh Weerman, R. P. Verkruisen, A. K. Groen, R. P. Oude Elferink, and et al. 1994.

'Mice with homozygous disruption of the mdr2 P-glycoprotein gene. A novel animal model for studies of nonsuppurative inflammatory cholangitis and hepatocarcinogenesis', *Am J Pathol*, 145: 1237-45.

Mayer, C., S. Nehring, M. Kucken, U. Repnik, S. Seifert, A. Sljukic, J. Delpierre, H. Morales-Navarrete, S. Hinz, M. Brosch, B. Chung, T. Karlsen, M. Huch, Y. Kalaidzidis, L. Brusch, J. Hampe, C. Schafmayer, and M. Zerial. 2023. 'Apical bulkheads accumulate as adaptive response to impaired bile flow in liver disease', *EMBO Rep*, 24: e57181.

Meerman, L., N. R. Koopen, V. Bloks, H. Van Goor, R. Havinga, B. G. Wolthers, W. Kramer, S. Stengelin, M. Muller, F. Kuipers, and P. L. Jansen. 1999. 'Biliary fibrosis associated with altered bile composition in a mouse model of erythropoietic protoporphyria', *Gastroenterology*, 117: 696-705.

Menon, M. B., J. Schwermann, A. K. Singh, M. Franz-Wachtel, O. Pabst, U. Seidler, M. B. Omary, A. Kotlyarov, and M. Gaestel. 2010. 'p38 MAP kinase and MAPKAP kinases MK2/3 cooperatively phosphorylate epithelial keratins', *J Biol Chem*, 285: 33242-51.

Meyer, K., H. Morales-Navarrete, S. Seifert, M. Wilsch-Braeuninger, U. Dahmen, E. M. Tanaka, L. Brusch, Y. Kalaidzidis, and M. Zerial. 2020. 'Bile canaliculi remodeling activates YAP via the actin cytoskeleton during liver regeneration', *Mol Syst Biol*, 16: e8985.

Meyer, K., O. Ostrenko, G. Bourantas, H. Morales-Navarrete, N. Porat-Shliom, F. Segovia-Miranda, H. Nonaka, A. Ghaemi, J. M. Verbavatz, L. Brusch, I. Sbalzarini, Y. Kalaidzidis, R. Weigert, and M. Zerial. 2017. 'A Predictive 3D Multi-Scale Model of Biliary Fluid Dynamics in the Liver Lobule', *Cell Syst*, 4: 277-90 e9.

Michalopoulos, G. K. 2007. 'Liver regeneration', *J Cell Physiol*, 213: 286-300.

Michalopoulos, G. K., and M. C. DeFrances. 1997. 'Liver regeneration', *Science*, 276: 60-6.

Miyoshi, H., C. Rust, P. J. Roberts, L. J. Burgart, and G. J. Gores. 1999. 'Hepatocyte apoptosis after bile duct ligation in the mouse involves Fas', *Gastroenterology*, 117: 669-77.

Moch, M., R. Windoffer, N. Schwarz, R. Pohl, A. Omenzetter, U. Schnakenberg, F. Herb, K. Chaisaowong, D. Merhof, L. Ramms, G. Fabris, B. Hoffmann, R. Merkel, and R. E. Leube. 2016. 'Effects of Plectin Depletion on Keratin Network Dynamics and Organization', *PLoS One*, 11: e0149106.

Moch, Marcin, and Rudolf E. Leube. 2021. 'Hemidesmosome-related keratin filament bundling and nucleation', *International Journal of Molecular Sciences*, 22: 1-24.

Morell, C. M., L. Fabris, and M. Strazzabosco. 2013. 'Vascular biology of the biliary epithelium', *J Gastroenterol Hepatol*, 28 Suppl 1: 26-32.

Mostov, K. E. 2003. 'Epithelial polarity and morphogenesis', *Methods*, 30: 189-90.

Musch, A. 2014. 'The unique polarity phenotype of hepatocytes', *Exp Cell Res*, 328: 276-83.

Nance, J., and J. A. Zallen. 2011. 'Elaborating polarity: PAR proteins and the cytoskeleton', *Development*, 138: 799-809.

Navis, A., and C. M. Nelson. 2016. 'Pulling together: Tissue-generated forces that drive lumen morphogenesis', *Semin Cell Dev Biol*, 55: 139-47.

Omary, M. B., N. O. Ku, P. Strnad, and S. Hanada. 2009. 'Toward unraveling the complexity of simple epithelial keratins in human disease', *J Clin Invest*, 119: 1794-805.

Omary, M. B., N. O. Ku, and D. M. Toivola. 2002. 'Keratins: guardians of the liver', *Hepatology*, 35: 251-7.

Osmanagic-Myers, S., T. Dechat, and R. Foisner. 2015. 'Lamins at the crossroads of mechanosignaling', *Genes Dev*, 29: 225-37.

Osmanagic-Myers, S., M. Gregor, G. Walko, G. Burgstaller, S. Reipert, and G. Wiche. 2006. 'Plectin-controlled keratin cytoarchitecture affects MAP kinases involved in cellular stress response and migration', *J Cell Biol*, 174: 557-68.

Osmanagic-Myers, S., S. Rus, M. Wolfram, D. Brunner, W. H. Goldmann, N. Bonakdar, I. Fischer, S. Reipert, A. Zuzuarregui, G. Walko, and G. Wiche. 2015. 'Plectin reinforces vascular integrity by mediating crosstalk between the vimentin and the actin networks', *J Cell Sci*, 128: 4138-50.

Pall, H., M. M. Zaman, C. Andersson, and S. D. Freedman. 2006. 'Decreased peroxisome proliferator activated receptor alpha is associated with bile duct injury in cystic fibrosis transmembrane conductance regulator-/- mice', *J Pediatr Gastroenterol Nutr*, 42: 275-81.

Pfendner, E., F. Rouan, and Jouni Uitto. 2005. "Progress in epidermolysis bullosa: The phenotypic spectrum of plectin mutations." In *Experimental Dermatology*, 241-49. Exp Dermatol.

Pollheimer, M. J., and P. Fickert. 2015. 'Animal models in primary biliary cirrhosis and primary sclerosing cholangitis', *Clin Rev Allergy Immunol*, 48: 207-17.

Pollheimer, M. J., M. Trauner, and P. Fickert. 2011. 'Will we ever model PSC? - "it's hard to be a PSC model!"', *Clin Res Hepatol Gastroenterol*, 35: 792-804.

Porat-Shliom, N., A. J. Tietgens, C. M. Van Itallie, L. Vitale-Cross, M. Jarnik, O. J. Harding, J. M. Anderson, J. S. Gutkind, R. Weigert, and I. M. Arias. 2016. 'Liver kinase B1 regulates hepatocellular tight junction distribution and function in vivo', *Hepatology*, 64: 1317-29.

Prechova, M., Z. Adamova, A. L. Schweizer, M. Maninova, A. Bauer, D. Kah, S. M. Meier-Menches, G. Wiche, B. Fabry, and M. Gregor. 2022. 'Plectin-mediated cytoskeletal crosstalk controls cell tension and cohesion in epithelial sheets', *J Cell Biol*, 221.

Quick, Q. A. 2018. 'Microtubule-Actin Crosslinking Factor 1 and Plakins as Therapeutic Drug Targets', *Int J Mol Sci*, 19.

Quinlan, R. A., N. Schwarz, R. Windoffer, C. Richardson, T. Hawkins, J. A. Broussard, K. J. Green, and R. E. Leube. 2017. 'A rim-and-spoke hypothesis to explain the biomechanical roles for cytoplasmic intermediate filament networks', *J Cell Sci*, 130: 3437-45.

Rabino, A., S. Awadia, N. Ali, A. Edson, and R. Garcia-Mata. 2024. 'The Scribble/SGEF/Dlg1 complex regulates the stability of apical junctions in epithelial cells', *bioRxiv*.

Raven, A., W. Y. Lu, T. Y. Man, S. Ferreira-Gonzalez, E. O'Duibhir, B. J. Dwyer, J. P. Thomson, R. R. Meehan, R. Bogorad, V. Koteliansky, Y. Kotelevtsev, C. Ffrench-Constant, L. Boulter, and S. J. Forbes. 2017. 'Cholangiocytes act as facultative liver stem cells during impaired hepatocyte regeneration', *Nature*, 547: 350-54.

Rezniczek, Günther A., Christina Abrahamsberg, Peter Fuchs, Daniel Spazierer, and Gerhard Wiche. 2003. 'Plectin 5'-transcript diversity: Short alternative sequences determine stability of gene products, initiation of translation and subcellular localization of isoforms', *Human Molecular Genetics*, 12: 3181-94.

Rogel, M. R., A. Jaitovich, and K. M. Ridge. 2010. 'The role of the ubiquitin proteasome pathway in keratin intermediate filament protein degradation', *Proc Am Thorac Soc*, 7: 71-6.

Roma, M. G., F. A. Crocenzi, and A. D. Mottino. 2008. 'Dynamic localization of hepatocellular transporters in health and disease', *World J Gastroenterol*, 14: 6786-801.

Russell, J. O., and F. D. Camargo. 2022. 'Hippo signalling in the liver: role in development, regeneration and disease', *Nat Rev Gastroenterol Hepatol*, 19: 297-312.

Sambrotta, M., S. Strautnieks, E. Papouli, P. Rushton, B. E. Clark, D. A. Parry, C. V. Logan, L. J. Newbury, B. M. Kamath, S. Ling, T. Grammatikopoulos, B. E. Wagner, J. C. Magee, R. J. Sokol, G. Mieli-Vergani, Genomics University of Washington Center for Mendelian, J. D. Smith, C. A. Johnson, P. McClean, M. A. Simpson, A. S. Knisely, L. N. Bull, and R. J. Thompson. 2014. 'Mutations in TJP2 cause progressive cholestatic liver disease', *Nat Genet*, 46: 326-8.

Sato, K., M. Marzioni, F. Meng, H. Francis, S. Glaser, and G. Alpini. 2019. 'Ductular Reaction in Liver Diseases: Pathological Mechanisms and Translational Significances', *Hepatology*, 69: 420-30.

Scheuerle, A. E., M. Ni, A. A. Ahmad, C. F. Timmons, D. Rakheja, E. E. Gordon, and M. Boothe. 2023. 'Biallelic variants in NUDCD2 associated with a multiple malformation syndrome with cholestasis and renal failure', *Am J Med Genet A*, 191: 2324-28.

Schliess, F., S. Hoehme, S. G. Henkel, A. Ghallab, D. Driesch, J. Bottger, R. Guthke, M. Pfaff, J. G. Hengstler, R. Gebhardt, D. Haussinger, D. Drasdo, and S. Zellmer. 2014. 'Integrated metabolic spatial-temporal model for the prediction of ammonia detoxification during liver damage and regeneration', *Hepatology*, 60: 2040-51.

Scholich, A., S. Syga, H. Morales-Navarrete, F. Segovia-Miranda, H. Nonaka, K. Meyer, W. de Back, L. Brusch, Y. Kalaidzidis, M. Zerial, F. Julicher, and B. M. Friedrich. 2020. 'Quantification of nematic cell polarity in three-dimensional tissues', *PLoS Comput Biol*, 16: e1008412.

Slim, C. L., IJzendoorn S. C. van, F. Lazaro-Dieguez, and A. Musch. 2014. 'The special case of hepatocytes: unique tissue architecture calls for a distinct mode of cell division', *Bioarchitecture*, 4: 47-52.

Snider, N. T., S. V. Weerasinghe, J. A. Iniguez-Lluhi, H. Herrmann, and M. B. Omary. 2011. 'Keratin hypersumoylation alters filament dynamics and is a marker for human liver disease and keratin mutation', *J Biol Chem*, 286: 2273-84.

Starkel, P., and I. A. Leclercq. 2011. 'Animal models for the study of hepatic fibrosis', *Best Pract Res Clin Gastroenterol*, 25: 319-33.

Strazzabosco, Mario, and Luca Fabris. 2013. 'The balance between Notch/Wnt signaling regulates progenitor cells’ commitment during liver repair: Mystery solved?', *Journal of Hepatology*, 58: 181-83.

Strnad, P., S. Paschke, K. H. Jang, and N. O. Ku. 2012. 'Keratins: markers and modulators of liver disease', *Curr Opin Gastroenterol*, 28: 209-16.

Szabo, S., K. L. Wogenstein, and P. Fuchs. 2016. 'Functional and Genetic Analysis of Epiplakin in Epithelial Cells', *Methods Enzymol*, 569: 261-85.

Szabo, S., K. L. Wogenstein, C. H. Osterreicher, N. Guldiken, Y. Chen, C. Doler, G. Wiche, P. Boor, J. Haybaeck, P. Strnad, and P. Fuchs. 2015. 'Epiplakin attenuates experimental mouse liver injury by chaperoning keratin reorganization', *J Hepatol*, 62: 1357-66.

Tag, C. G., S. Sauer-Lehnen, S. Weiskirchen, E. Borkham-Kamphorst, R. H. Tolba, F. Tacke, and R. Weiskirchen. 2015. 'Bile duct ligation in mice: induction of inflammatory liver injury and fibrosis by obstructive cholestasis', *J Vis Exp*.

Tag, C. G., S. Weiskirchen, K. Hittatiya, F. Tacke, R. H. Tolba, and R. Weiskirchen. 2015. 'Induction of experimental obstructive cholestasis in mice', *Lab Anim*, 49: 70-80.

Tam, P. K. H., R. S. Yiu, U. Lendahl, and E. R. Andersson. 2018. 'Cholangiopathies - Towards a molecular understanding', *EBioMedicine*, 35: 381-93.

Tanimizu, N., A. Miyajima, and K. E. Mostov. 2007. 'Liver progenitor cells develop cholangiocyte-type epithelial polarity in three-dimensional culture', *Mol Biol Cell*, 18: 1472-9.

ter Beest, M. B., S. J. Chapin, D. Avrahami, and K. E. Mostov. 2005. 'The role of syntaxins in the specificity of vesicle targeting in polarized epithelial cells', *Mol Biol Cell*, 16: 5784-92.

Teutsch, H. F. 2005. 'The modular microarchitecture of human liver', *Hepatology*, 42: 317-25.

Theard, D., M. Steiner, D. Kalicharan, D. Hoekstra, and S. C. van Ijzendoorn. 2007. 'Cell polarity development and protein trafficking in hepatocytes lacking E-cadherin/beta-catenin-based adherens junctions', *Mol Biol Cell*, 18: 2313-21.

Thebaut, A., M. Aumar, A. Gardin, M. Almes, A. Davit-Spraul, and E. Jacquemin. 2024. 'Failure of cholic acid therapy in a child with a bile acid synthesis defect and harboring plectin mutations', *J Pediatr Gastroenterol Nutr*, 78: 1203-04.

Tocan, V., J. Hayase, S. Kamakura, A. Kohda, S. Ohga, M. Kohjima, and H. Sumimoto. 2021. 'Hepatocyte polarity establishment and apical lumen formation are organized by Par3, Cdc42, and aPKC in conjunction with Lgl', *J Biol Chem*, 297: 101354.

Toivola, D. M., P. Boor, C. Alam, and P. Strnad. 2015. 'Keratins in health and disease', *Curr Opin Cell Biol*, 32: 73-81.

Toivola, D. M., L. Polari, T. Schwerd, N. Schlegel, and P. Strnad. 2024. 'The keratin-desmosome scaffold of internal epithelia in health and disease - The plot is thickening', *Curr Opin Cell Biol*, 86: 102282.

Toivola, D. M., P. Strnad, A. Habtezion, and M. B. Omary. 2010. 'Intermediate filaments take the heat as stress proteins', *Trends Cell Biol*, 20: 79-91.

Torok, G., Z. Erdei, J. Lilienberg, A. Apati, and L. Homolya. 2020. 'The importance of transporters and cell polarization for the evaluation of human stem cell-derived hepatic cells', *PLoS One*, 15: e0227751.

Torre, C., C. Perret, and S. Colnot. 2010. 'Molecular determinants of liver zonation', *Prog Mol Biol Transl Sci*, 97: 127-50.

Trauner, M., P. Fickert, E. Halilbasic, and T. Moustafa. 2008. 'Lessons from the toxic bile concept for the pathogenesis and treatment of cholestatic liver diseases', *Wien Med Wochenschr*, 158: 542-8.

Treyer, A., and A. Musch. 2013. 'Hepatocyte polarity', *Compr Physiol*, 3: 243-87.

Tsukada, N., C. A. Ackerley, and M. J. Phillips. 1995. 'The structure and organization of the bile canalicular cytoskeleton with special reference to actin and actin-binding proteins', *Hepatology*, 21: 1106-13.

Vahidnezhad, H., L. Youssefian, N. Harvey, A. R. Tavasoli, A. H. Saeidian, S. Sotoudeh, A. Varghaei, H. Mahmoudi, P. Mansouri, N. Mozafari, O. Zargari, S. Zeinali, and J. Uitto. 2022. 'Mutation update: The spectra of PLEC sequence variants and related plectinopathies', *Hum Mutat*, 43: 1706-31.

Van Campenhout, S., H. Van Vlierberghe, and L. Devisscher. 2019. 'Common Bile Duct Ligation as Model for Secondary Biliary Cirrhosis', *Methods Mol Biol*, 1981: 237-47.

Vartak, N., A. Damle-Vartak, B. Richter, O. Dirsch, U. Dahmen, S. Hammad, and J. G. Hengstler. 2016. 'Cholestasis-induced adaptive remodeling of interlobular bile ducts', *Hepatology*, 63: 951-64.

Vilas-Boas, V., E. Gijbels, A. Cooreman, R. Van Campenhout, E. Gustafson, K. Leroy, and M. Vinken. 2019. 'Industrial, Biocide, and Cosmetic Chemical Inducers of Cholestasis', *Chem Res Toxicol*, 32: 1327-34.

Vinken, M., B. Landesmann, M. Goumenou, S. Vinken, I. Shah, H. Jaeschke, C. Willett, M. Whelan, and V. Rogiers. 2013. 'Development of an adverse outcome pathway from drug-mediated bile salt export pump inhibition to cholestatic liver injury', *Toxicol Sci*, 136: 97-106.

Wakabayashi, Y., P. Dutt, J. Lippincott-Schwartz, and I. M. Arias. 2005. 'Rab11a and myosin Vb are required for bile canalicular formation in WIF-B9 cells', *Proc Natl Acad Sci U S A*, 102: 15087-92.

Wakabayashi, Y., J. Lippincott-Schwartz, and I. M. Arias. 2004. 'Intracellular trafficking of bile salt export pump (ABCB11) in polarized hepatic cells: constitutive cycling between the canalicular membrane and rab11-positive endosomes', *Mol Biol Cell*, 15: 3485-96.

Walko, G., M. J. Castanon, and G. Wiche. 2015. 'Molecular architecture and function of the hemidesmosome', *Cell Tissue Res*, 360: 529-44.

Wang, L., and J. L. Boyer. 2004. 'The maintenance and generation of membrane polarity in hepatocytes', *Hepatology*, 39: 892-9.

Wang, L., F. Cao, L. L. Zhu, P. Liu, Y. R. Shang, W. H. Liu, X. Dong, H. D. Bao, P. Gong, and Z. Y. Wang. 2019. 'Andrographolide impairs alpha-naphthylisothiocyanate-induced cholestatic liver injury in vivo', *J Nat Med*, 73: 388-96.

Wang, R., P. Lam, L. Liu, D. Forrest, I. M. Yousef, D. Mignault, M. J. Phillips, and V. Ling. 2003. 'Severe cholestasis induced by cholic acid feeding in knockout mice of sister of P-glycoprotein', *Hepatology*, 38: 1489-99.

Wang, T., K. Yanger, B. Z. Stanger, D. Cassio, and E. Bi. 2014. 'Cytokinesis defines a spatial landmark for hepatocyte polarization and apical lumen formation', *J Cell Sci*, 127: 2483-92.

Wang, Y., Y. C. Toh, Q. Li, B. Nugraha, B. Zheng, T. B. Lu, Y. Gao, M. M. Ng, and H. Yu. 2013. 'Mechanical compaction directly modulates the dynamics of bile canaliculi formation', *Integr Biol (Camb)*, 5: 390-401.

Watanabe, S., M. Miyairi, C. Oshio, C. R. Smith, and M. J. Phillips. 1983. 'Phalloidin alters bile canalicular contractility in primary monolayer cultures of rat liver', *Gastroenterology*, 85: 245-53.

Wiche, G. 1998. 'Role of plectin in cytoskeleton organization and dynamics', *J Cell Sci*, 111 (Pt 17): 2477-86.

———. 2021. 'Plectin-Mediated Intermediate Filament Functions: Why Isoforms Matter', *Cells*, 10.

———. 2022. 'Plectin in Health and Disease', *Cells*, 11.

Winter, L., and G. Wiche. 2013. 'The many faces of plectin and plectinopathies: pathology and mechanisms', *Acta Neuropathol*, 125: 77-93.

Woods, A., A. J. Heslegrave, P. J. Muckett, A. P. Levene, M. Clements, M. Mobberley, T. A. Ryder, S. Abu-Hayyeh, C. Williamson, R. D. Goldin, A. Ashworth, D. J. Withers, and D. Carling. 2011. 'LKB1 is required for hepatic bile acid transport and canalicular membrane integrity in mice', *Biochem J*, 434: 49-60.

Wu, J., S. Fang, W. Li, Y. Li, Y. Li, T. Wang, L. Yang, S. Liu, Z. Wang, and Y. Ma. 2020. 'Metabolomics research on the hepatoprotective effect of cultured bear bile powder in alpha-naphthylisothiocyanate-induced cholestatic mice', *J Chromatogr B Analyt Technol Biomed Life Sci*, 1153: 122269.

Wu, S. H., J. S. Hsu, H. L. Chen, M. M. Chien, J. F. Wu, Y. H. Ni, B. Y. Liou, M. C. Ho, Y. M. Jeng, M. H. Chang, P. L. Chen, and H. L. Chen. 2019. 'Plectin Mutations in Progressive Familial Intrahepatic Cholestasis', *Hepatology*, 70: 2221-24.

Wu, W., K. Li, X. Ran, W. Wang, X. Xu, Y. Zhang, X. Wei, and T. Zhang. 2022. 'Combination of resveratrol and luteolin ameliorates alpha-naphthylisothiocyanate-induced cholestasis by regulating the bile acid homeostasis and suppressing oxidative stress', *Food Funct*, 13: 7098-111.

Yeh, T. H., L. Krauland, V. Singh, B. Zou, P. Devaraj, D. B. Stolz, J. Franks, S. P. Monga, E. Sasatomi, and J. Behari. 2010. 'Liver-specific beta-catenin knockout mice have bile canalicular abnormalities, bile secretory defect, and intrahepatic cholestasis', *Hepatology*, 52: 1410-9.

Yokoda, R. T., and E. A. Rodriguez. 2020. 'Review: Pathogenesis of cholestatic liver diseases', *World J Hepatol*, 12: 423-35.

Yokota, S., Y. Ono, T. Nakao, P. Zhang, G. K. Michalopoulos, and Z. Khan. 2018. 'Partial Bile Duct Ligation in the Mouse: A Controlled Model of Localized Obstructive Cholestasis', *J Vis Exp*.

Zatloukal, K., S. W. French, C. Stumptner, P. Strnad, M. Harada, D. M. Toivola, M. Cadrin, and M. B. Omary. 2007. 'From Mallory to Mallory-Denk bodies: what, how and why?', *Exp Cell Res*, 313: 2033-49.

Zatloukal, K., C. Stumptner, A. Fuchsbichler, P. Fickert, C. Lackner, M. Trauner, and H. Denk. 2004. 'The keratin cytoskeleton in liver diseases', *J Pathol*, 204: 367-76.

Zhang, Y., R. De Mets, C. Monzel, V. Acharya, P. Toh, J. F. L. Chin, N. Van Hul, I. C. Ng, H. Yu, S. S. Ng, S. Tamir Rashid, and V. Viasnoff. 2020. 'Biomimetic niches reveal the minimal cues to trigger apical lumen formation in single hepatocytes', *Nat Mater*, 19: 1026-35.

Zheng, Bin, and Lewis C. Cantley. 2007. 'Regulation of epithelial tight junction assembly and disassembly by AMP-activated protein kinase', *Proceedings of the National Academy of Sciences of the United States of America*, 104: 819-22.

Zhong, B., P. Strnad, C. Selmi, P. Invernizzi, G. Z. Tao, A. Caleffi, M. Chen, I. Bianchi, M. Podda, A. Pietrangelo, M. E. Gershwin, and M. B. Omary. 2009. 'Keratin variants are overrepresented in primary biliary cirrhosis and associate with disease severity', *Hepatology*, 50: 546-54.